Chemistry and Physics of Water Dissociation in Bipolar Membranes

by

Lihaokun Chen

A dissertation accepted and approved in partial fulfillment of the

requirements for the degree of

Doctor of Philosophy

in Chemistry

Dissertation Committee:

Carl K. Brozek, Chair

Shannon W. Boettcher, Advisor

Christopher H. Hendon, Core Member

Calin Plesa, Institutional Representative

University of Oregon

Fall 2023

DISSERTATION ABSTRACT

Lihaokun Chen

Doctor of Philosophy in Chemistry

Title: Chemistry and Physics of Water Dissociation in Bipolar Membranes

Water dissociation (WD, $H_2O \rightarrow H^+ + OH^-$) is the core process in bipolar membranes (BPMs) that limits energy efficiency. Both electric-field and catalytic effects have been invoked to describe WD, but the interplay of the two and the underlying design principles for WD catalysts remain unclear. Furthermore, how WD is driven by voltage and catalyzed is not understood. In Chapter II, by using precise layers of metal-oxide nanoparticles, membrane-electrolyzer platforms, materials characterization, and impedance analysis, we illustrate the role of electronic conductivity in modulating the performance of WD catalysts in the BPM junction through screening and focusing the interfacial electric field and thus electrochemical potential gradients. In contrast, the ionic conductivity of the same layer is not a significant factor in limiting performance. BPM water electrolyzers, optimized *via* these findings, use ~30-nm-diameter anatase TiO_2 as an earth-abundant WD catalyst, and generate O_2 and H_2 at 500 mA cm^{-2} with a record-low total cell voltage below 2 V. These advanced BPMs might accelerate deployment of new electrodialysis, carbon-capture, and carbon-utilization technology. In Chapter III, we report BPM electrolyzers with two reference electrodes to measure temperature-dependent WD current

and overpotential (η_{wd}) without soluble electrolyte. Using TiO_2-P25-nanoparticle catalyst and Arrhenius-type analysis, $E_{a,wd}$ was 25–30 kJ/mol, independent of η_{wd}, with a pre-exponential factor proportional to η_{wd} that decreases ~10-fold in D_2O. We propose a new WD mechanism where metal-oxide nanoparticles, polarized by the BPM-junction voltage, serve as proton *i*) acceptors (from water) on the negative-charged side of the particle to generate free OH^-, *ii*) donors on the positive-charged side to generate H_3O^+, and *iii*) surface conductors that connect spatially separate donor/acceptor sites. Increasing electric-field with η_{wd} orients water for proton-transfer, increasing the pre-exponential factor, but is insufficient to lower E_a.

This dissertation includes previously published and unpublished co-authored materials.

CURRICULUM VITAE

NAME OF AUTHOR: Lihaokun Chen

GRADUATE AND UNDERGRADUATE SCHOOLS ATTENDED:

University of Oregon, Eugene, Oregon, United States of America

Peking University, Beijing, People's Republic of China

DEGREES AWARDED:

Doctor of Philosophy, Chemistry, 2023, University of Oregon

Bachelor of Science, Environmental Science, 2019, Peking University

AREAS OF SPECIAL INTEREST:

Electrochemistry, Energy Science, Water Electrolysis

PROFESSIONAL EXPERIENCE:

Research Assistant, University of Oregon, 2019 – 2023

Teaching Assistant, University of Oregon, 2019 – 2023

PUBLICATIONS:

Chen, L.; Xu, Q.; Boettcher, S. W. Kinetics and mechanism of heterogeneous voltage-driven water-dissociation catalysis. *Joule* **2023**, *7* (8), 1867-1886.

Chen, L.; Xu, Q.; Oener, S. Z.; Fabrizio, K.; Boettcher, S. W. Design principles for water dissociation catalysts in high-performance bipolar membranes. *Nat. Commun.* **2022**, *13* (1), 3846.

Mitchell, J. B.; **Chen, L.**; Langworthy, K.; Fabrizio, K.; Boettcher, S. W. Catalytic proton–hydroxide recombination for forward-bias bipolar membranes. *ACS Energy Lett.* **2022**, *7* (11), 3967-3973.

Marin, D. H.; Perryman, J. T.; Hubert, M. A.; Lindquist, G. A.; **Chen, L.**; Aleman, A. M.; Kamat, G. A.; Niemann, V. A.; Stevens, M. B.; Regmi, Y. N.; et al. Hydrogen production with seawater-resilient bipolar membrane electrolyzers. *Joule* **2023**, *7* (4), 765-781.

Andreeva, A. B.; Le, K. N.; **Chen, L.**; Kellman, M. E.; Hendon, C. H.; Brozek, C. K. Soft Mode Metal-Linker Dynamics in Carboxylate MOFs Evidenced by Variable-Temperature Infrared Spectroscopy. *J. Am. Chem. Soc.* **2020**, *142* (45), 19291-19299.

Wang, L.; Zhou, H.; Li, N.; Zhang, Y.; **Chen, L.**; Ke, X.; Chen, Z.; Wang, Z.; Sui, M.; Chen, Y.; et al. Carrier transport composites with suppressed glass-transition for stable planar perovskite solar cells. *J. Mat. Chem. A* **2020**, *8* (28), 14106-14113.

ACKNOWLEDGMENTS

I would like to give my big thank you to my advisor Prof. Shannon W. Boettcher, for letting me join his group, teaching me electrochemistry ("celebration of knowledge") and all sorts of skills, including writing papers ("data + logic = good") and proposals, dealing with reviewers, using the drill press and vice grip to make something "in five minutes", so and so on. Among all of these, the most important and astonishing thing I learned is that he is very willing to help others, which impressed, inspired, and encouraged me a lot, so much so that he is life model for me in terms of this. The second most important thing is that he is an optimist, who tends to view things differently from me (a somewhat pessimistic person). His high energy generally cheers me up whenever I think about how his "high-volume love" spreads in the classroom, in the office, in the lab, and in the Zoom meeting. The third most important thing is that he usually responds to e-mails very quickly – a very good habit I learned!

I wish to express sincere appreciation to Prof. Mark C. Lonergan, for his rigorous and amusing way of teaching ("welcome to the world of electrochemistry" and "my favorite electrolyte"), his moral character, his understanding for students, and his sincere advice when I have big decisions to make. Special thanks are due to my committee members, including Shannon, Prof. Carl K. Brozek, Prof. Christopher H. Hendon, and Prof. Calin Plesa. Thank you all for the support over the years. In addition, I also would like to thank Prof. Paul A. Kempler, Prof. Gary S. Harlow, and Dr. Andreas R. Stonas, for their answers and suggestions to my various questions and problems.

To my mentors: Sebastian Z. Oener and Qiucheng Xu, who taught me how to make bipolar membranes and assemble electrolyzers. To my labmates: Changsuk Yun, Hakan Görçay, Meikun Shen, James B. Mitchell, Sayantan Sasmal, Jiawei Huang, Anthony C. Ekennia, Prasad V. Sarma, Kasinath Ojha, Xudong Hu, Anastasiia Konovalova, Shujin Hou, Jessica L. Fehrs, Lu Liu, Yingqing Ou, Raina A. Krivina, Tawney A. Knecht, Grace A. Lindquist, Yang Zhao, Tingting Zhai, Yi-Lin Kao, Liam P. Twight, Aaron J. Kaufman, Minkyoung Kwak, Olivia P. Traenkle, Kira A. Thurman, Nick D'Antona, Nicole A. Saguì, Manasa Rajeev, Raj Shekhar, Dwaipayan Roychowdhury, and orthers, for all kinds of help and support, and the good discussions and time we had. To my mentees: Dylan H. Bauer, Liza Briody-Pavlik, and Brian G. Diamond, for giving me the chance to build up my ability to teach and lead a project.

Special thanks to my mentors and coworkers in other labs: Alison S. Chang, Anastasia B. Andreeva, Kevin Fabrizio, and to many people at the University of Oregon who helped me along the way: Kurt Langworthy, Casey Check, Casey Simons, Josh Razink, Valerie Brogden, Julie Chouinard; Julian McAdams, Geordi Allred, Jefferson Garman, John Boosinger; Natalie Dunn (and her dog), Christian Gervasi; Christi Mabinuori, Leah O'Brien, Janet Kneller, Laurie Schneider, and others. To my collaborators at other universities: Daniela H. Marin, Joseph T. Perryman, McKenzie A. Hubert, Adam C. Nielander, Boris V. Kramar, Michael W. Mara, Madison C. Schwinn, Harrison J. Cassady, Maria Rochow, William White, and others.

Finally, sincere gratefulness to my parents, other family members, and my friends (especially Ruijia Yang, Jianshu Wang, and Shengyu Zou) for their love and support over the years.

This work was supported by the U.S. Office of Naval Research, grant N00014-20-1-2517. The work used shared instrumentation in the Center for Advanced Materials Characterization in Oregon (CAMCOR) and the Phil and Penny Knight Campus for Accelerating Scientific Impact.

To my parents, and my middle school mathematics teacher – Mrs. Zirong Xia, who taught me logic, plane geometry, the axiomatic system, and proof, which is the starting point for my science journey.

献给我父母，以及我的初中数学老师——夏梓荣老师，她教给了我逻辑、平面几何、公理化体系和证明，这是我科学之旅的起点。

TABLE OF CONTENTS

LIST OF FIGURES

LIST OF TABLES

CHAPTER I

INTRODUCTION

Co-authored unpublished material with Shannon W. Boettcher.

Water dissociation (WD, $H_2O \rightleftharpoons H^+ + OH^-$) is important for *any* chemical reaction that uses water as a reactant. Understanding fundamental WD mechanisms in pure water, and the reverse $H^+ + OH^-$ recombination, has been a focus of experiment and theory for decades.[1-3] The related dissociative adsorption of water, $H_2O \rightleftharpoons H_{ad} + OH_{ad}$, occurs on surfaces and is important when water reacts in thermochemical processes, such as for water-gas-shift catalysis.[4] The interaction of water with surfaces has thus been of longstanding interest,[5] with broad importance to corrosion, passivation, and geological processes.[6] In biology, metalloenzymes activate water. Carbonic anhydrase, for example, binds water to Zn^{2+} and releases H^+ to generate nucleophilic OH^- that reacts with CO_2 to form HCO_3^-.[7] During the alkaline hydrogen-evolution reaction (HER, $2H_2O + 2e^- \rightarrow H_2 + 2OH^-$), important for low-cost alkaline water electrolysis,[8] the first step is WD coupled with the formation of a surface metal hydride ($H_2O + M^* + e^- \rightarrow M\text{–}H + OH^-$) and is thought to be rate limiting. Modification of metals with hydroxides, to catalyze WD, increase HER activity via a bifunctional mechanism,[9-10] though alternative explanations have been proposed.[11-13]

While researchers have studied WD rate and mechanism in pure water,[2-3, 14-15] the understanding of WD *catalysis* under electrochemical conditions is poor. A bipolar membrane

(BPM, Figure 1.1) electrolyzer offers a platform for fundamental science studies of WD (in addition to the many applications of high-performance BPMs). A BPM consists of an anion exchange layer (AEL) and a cation exchange layer (CEL), sometimes WD catalysts are added at the junction between AEL and CEL. In reverse bias, H_2O diffuses to the BPM junction, and *dissociates* into H^+ and OH^-. The voltage drives H^+ through the CEL towards the cathode where the HER occurs, and OH^- through AEL towards the anode where the oxygen evolution reaction (OER) occurs. As one example, reverse-bias BPMs enable new classes of water electrolyzers where OH^- is delivered to a basic anode that enables the use of fast earth-abundant non-precious metal catalysts, and H^+ to an acidic cathode where HER kinetics is faster than in base.

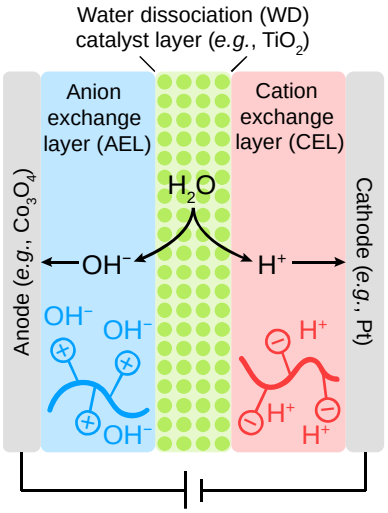

Figure 1.1 Schematic diagram of a bipolar membrane (BPM) electrolyzer

In reverse bias, H_2O dissociates into H^+ and OH^- at the BPM junction. H^+ transports to cathode to generate H_2, while OH^- transports to anode to generate oxygen.

Using the BPM electrolyzer platform, Oener et al. studied the *kinetics of WD* on the

metal-oxide nanoparticle catalysts surfaces and discovered that local pH is a critical, but previously unrecognized, parameter. They proposed a pH-dependent proton-transfer mechanism on metal-oxide nanoparticles to explain our data.[16] To study WD at a specific local-pH, they used a stable WD catalyst at one membrane surface while systematically varying the WD catalyst at the other membrane surface and discovered a correlation between WD overpotential η_{wd} and the metal oxide's point of zero charge (PZC, the pH at which the oxide surface is electrically neutral) estimated *via* zeta-potential measurements. With NiO on the basic AEL surface, the best WD catalysts on the acidic CEL surface have acidic PZCs near 1-2. With Sb:SnO_2 on the acidic CEM surface, the best WD catalysts on the basic AEL surface have basic PZCs > 12. Combining the best WD catalysts in the locally basic and acidic environments leads to η_{wd} of < 10 mV at 20 mA cm^{-2} – *at least 10 times lower than commercial BPMs*,[16-18] which is driving tremendous interest in using WD catalysis in BPMs for many applications, including to make acid and base for carbon capture from the air or ocean water,[19-21] and to prevent cross-over of unwanted species in CO_2 electrolyzers that yield useful products from waste or captured CO_2.[22] While this performance improvement is impressive, it remains unclear precisely how the WD reaction is catalyzed, what the active sites are, how to multiply them, and what the foundation design principles are that will enable water dissociation and related reaction catalysts to be systematically engineered.

Weak acid/base groups have been implicated in the WD mechanism on organic groups,[23-27] but the mechanism of *heterogeneous WD catalysts* is unclear even though they are critical for efficient BPM devices.[28-29] Other studies of inorganic compounds show poor performance and provide little fundamental insight.[30-33] The experimental work by Oener et al. provides strong

preliminary data and a platform on which the current joint experimental – theory-computational approach is based. The goal is to establish a new paradigm of understanding that bridges the molecular mechanisms and the solid-state materials physics of water's reactions on surfaces.

This dissertation aims to shed light on the design principles for WD catalysts, as well as kinetics and mechanisms. Chapter II studies WD catalysts of different properties in pure-water BPM electrolyzers, and discusses the loading dependence and the surprising effect of electronic conductivity. Chapter III further dives into the temperature dependence of WD in BPMs by integrating reference electrodes to isolate the WD overpotential. The unexpected kinetics parameters dependence on WD overpotential is discussed, and a possible molecular mechanism is proposed. Finally, Chapter IV gives a summary of this dissertation and points out challenges and opportunities for future research of WD in BPMs.

Chapters I and IV contain co-authored unpublished material with Shannon W. Boettcher. Chapter II is published as **Chen, L.**; Xu, Q.; Oener, S. Z.; Fabrizio, K.; Boettcher, S. W. Design principles for water dissociation catalysts in high-performance bipolar membranes. *Nat. Commun.* **2022**, *13* (1), 3846. Chapter III is published as **Chen, L.**; Xu, Q.; Boettcher, S. W. Kinetics and mechanism of heterogeneous voltage-driven water-dissociation catalysis. *Joule* **2023**, *7* (8), 1867-1886.

REFERENCES

1. Moqadam, M.; Lervik, A.; Riccardi, E.; Venkatraman, V.; Alsberg, B. K.; van Erp, T. S., Local initiation conditions for water autoionization. *Proc. Nat. Acad. Sci.* **2018,** *115* (20), E4569-E4576.

2. Eigen, M.; Maeyer, L. d., Untersuchungen über die kinetik der neutralisation. I. *Z. Elecktrochem.* **1955,** *59*, 986.

3. Ertl, G.; Gerischer, H., Ein vergleich der kinetik der neutralisationsreaktionen des leichten und schweren wassers. *Z. Elecktrochem.* **1962,** *66*, 560.

4. Ovesen, C. V.; Stoltze, P.; Nørskov, J. K.; Campbell, C. T., A kinetic model of the water gas shift reaction. *J. Catal.* **1992,** *134* (2), 445-468.

5. Sterrer, M.; Nilius, N.; Shaikhutdinov, S.; Heyde, M.; Schmidt, T.; Freund, H.-J., Interaction of water with oxide thin film model systems. *J. Mater. Res.* **2019,** *34* (3), 360-378.

6. Thiel, P. A.; Madey, T. E., The interaction of water with solid surfaces: fundamental aspects. *Surf. Sci. Rep.* **1987,** *7* (6-8), 211-385.

7. Bertini, I.; Luchinat, C., The reaction pathways of zinc enzymes and related biological catalysts. In *Bioinorganic Chemistry*, University Science Books: Mill Valley, CA, 1994; pp 37-106.

8. Xu, D.; Stevens, M. B.; Cosby, M. R.; Oener, S. Z.; Smith, A. M.; Enman, L. J.; Ayers, K. E.; Capuano, C. B.; Renner, J. N.; Danilovic, N.; Li, Y.; Wang, H.; Zhang, Q.; Boettcher, S. W., Earth-abundant oxygen electrocatalysts for alkaline anion-exchange-membrane water electrolysis: effects of catalyst conductivity and comparison with performance in three-electrode cells. *ACS Catalysis* **2019,** *9* (1), 7-15.

9. Danilovic, N.; Subbaraman, R.; Strmcnik, D.; Chang, K.-C.; Paulikas, A. P.; Stamenkovic, V. R.; Markovic, N. M., Enhancing the alkaline hydrogen evolution reaction activity through the bifunctionality of $Ni(OH)_2$/metal catalysts. *Angew. Chem. Int. Ed.* **2012,** *51* (50), 12495-12498.

10. Subbaraman, R.; Tripkovic, D.; Strmcnik, D.; Chang, K. C.; Uchimura, M.; Paulikas, A. P.; Stamenkovic, V.; Markovic, N. M., Enhancing hydrogen evolution activity in water splitting by tailoring Li^+-$Ni(OH)_2$-Pt interfaces. *Science* **2011,** *334* (6060), 1256-1260.

11. Chen, X.; McCrum, I. T.; Schwarz, K. A.; Janik, M. J.; Koper, M. T. M., Co-adsorption of cations as the cause of the apparent pH dependence of hydrogen adsorption on a stepped platinum single-crystal electrode. *Angew. Chem. Int. Ed.* **2017,** *56* (47), 15025-15029.

12. Ledezma-Yanez, I.; Wallace, W. D. Z.; Sebastián-Pascual, P.; Climent, V.; Feliu, J. M.; Koper, M. T. M., Interfacial water reorganization as a pH-dependent descriptor of the hydrogen evolution rate on platinum electrodes. *Nat. Energy.* **2017,** *2*, 17031.

13. Zheng, J.; Sheng, W.; Zhuang, Z.; Xu, B.; Yan, Y., Universal dependence of hydrogen oxidation and evolution reaction activity of platinum-group metals on pH and hydrogen binding energy. *Science Advances* **2016,** *2* (3), e1501602.

14. Geissler, P. L.; Dellago, C.; Chandler, D.; Hutter, J.; Parrinello, M., Autoionization in liquid water. *Science* **2001,** *291* (5511), 2121-2124.

15. Hassanali, A.; Prakash, M. K.; Eshet, H.; Parrinello, M., On the recombination of hydronium and hydroxide ions in water. *Proc. Nat. Acad. Sci.* **2011,** *108* (51), 20410-20415.

16. Oener, S. Z.; Foster, M. J.; Boettcher, S. W., Accelerating water dissociation in bipolar membranes and for electrocatalysis. *Science* **2020,** *369* (6507), 1099-1103.

17. Oener, S. Z.; Foster, M.; Boettcher, S. W. Bipolar Membranes. 2019, US Patent Application No. 62/984,652.

18. Shen, C. H.; Wycisk, R.; Pintauro, P. N., High performance electrospun bipolar membrane with a 3D junction. *Energy Environ. Sci.* **2017,** *10* (6), 1435-1442.

19. Heimdall Ocean Carbon Capture Company. *https://www.heimdalccu.com/* **2022**.

20. Captura – the future of carbon capture. *https://capturacorp.com/* **2022**.

21. CarbonCapture Inc. - Direct air capture. *https://www.carboncapture.com/* **2022**.

22. Xie, K.; Miao, R. K.; Ozden, A.; Liu, S.; Chen, Z.; Dinh, C.-T.; Huang, J. E.; Xu, Q.; Gabardo, C. M.; Lee, G.; Edwards, J. P.; O'Brien, C. P.; Boettcher, S. W.; Sinton, D.; Sargent, E. H., Bipolar membrane electrolyzers enable high single-pass CO_2 electroreduction to multicarbon products. *Nat. Commun.* **2022,** *13* (1), 3609.

23. Simons, R., Strong electric field effects on proton transfer between membrane-bound amines and water. *Nature* **1979,** *280* (5725), 824-826.

24. Simons, R.; Khanarian, G., Water dissociation in bipolar membranes: Experiments and theory. *J. Membrane Biol.* **1978,** *38* (1), 11-30.

25. Strathmann, H.; Rapp, H. J.; Bauer, B.; Bell, C. M., Theoretical and practical aspects of preparing bipolar membranes. *Desalination* **1993,** *90* (1-3), 303-323.

26. Yaroslavtsev, A. B.; Nikonenko, V. V.; Zabolotsky, V. I., Ion transfer in ion-exchange and membrane materials. *Russ. Chem. Rev.* **2003,** *72* (5), 393-421.

27. Zabolotskii, V. I.; Shel'deshov, N. V.; Gnusin, N. P., Dissociation of water molecules in systems with ion-exchange membranes. *Russ. Chem. Rev.* **1988,** *57* (8), 801-808.

28. Vermaas, D. A.; Sassenburg, M.; Smith, W. A., Photo-assisted water splitting with bipolar membrane induced pH gradients for practical solar fuel devices. *J. Mat. Chem. A* **2015,** *3* (38), 19556-19562.

29. Yan, Z.; Zhu, L.; Li, Y. C.; Wycisk, R. J.; Pintauro, P. N.; Hickner, M. A.; Mallouk, T. E., The balance of electric field and interfacial catalysis in promoting water dissociation in bipolar membranes. *Energy Environ. Sci.* **2018,** *11* (8), 2235-2245.

30. Balster, J.; Srinkantharajah, S.; Sumbharaju, R.; Pünt, I.; Lammertink, R. G. H.; Stamatialis, D. F.; Wessling, M., Tailoring the interface layer of the bipolar membrane. *J. Membr. Sci.* **2010,** *365* (1-2), 389-398.

31. Mel'nikov, S. S.; Shapovalova, O. V.; Shel'deshov, N. V.; Zabolotskii, V. I., Effect of d-metal hydroxides on water dissociation in bipolar membranes. *Pet. Chem.* **2011,** *51* (7), 577-584.

32. Rajesh, A. M.; Chakrabarty, T.; Prakash, S.; Shahi, V. K., Effects of metal alkoxides on electro-assisted water dissociation across bipolar membranes. *Electrochim. Acta* **2012,** *66*, 325-331.

33. Hanada, F.; Hiraya, K.; Ohmura, N.; Tanaka, S. Bipolar membrane and method for its production European Patent: EP0459820B1, 1991.

CHAPTER II

DESIGN PRINCIPLES FOR WATER DISSOCIATION CATALYSTS IN HIGH-PERFORMANCE BIPOLAR MEMBRANES

Published as **Chen, L.**; Xu, Q.; Oener, S. Z.; Fabrizio, K.; Boettcher, S. W. Design principles for water dissociation catalysts in high-performance bipolar membranes. *Nat. Commun.* **2022**, *13* (1), 3846. L.C., Q.X. and S.W.B. conceived the experiments and led the project. L.C. performed most experiments. Q.X. performed pilot experiments. S.Z.O trained Q.X. and L.C. on the fabrication of BPMs and provided insightful feedback on the analysis. K.F. performed the BET experiments. L.C. and S.W.B. wrote the manuscript with input from all authors.

INTRODUCTION

A bipolar membrane (BPM) consists of an anion-exchange layer (AEL) and a cation-exchange layer (CEL) sandwiched together[1-2]. The AEL contains fixed positively charged groups and mobile anions, while CEL contains fixed negatively charged groups and mobile cations (Figure 2.1a). BPMs were first conceived as an ionic counterpart to current-rectifying semiconductor *pn* junctions[3-5], and now are used in electrodialysis devices for desalination and acid/base production from brine[6], fuel cells[7], water and CO_2 electrolysis[8-9], flow batteries[10], and protonic diodes[11]. They provide distinct alkaline and acidic environments that are ideal for water oxidation and water reduction, respectively, offering new pathways for increasing electrolyzer performance while reducing or eliminating precious metals use[12]. In CO_2 electroreduction, BPMs

retard crossover of carbonate and product species, thus increasing Faradaic efficiency[13-16].

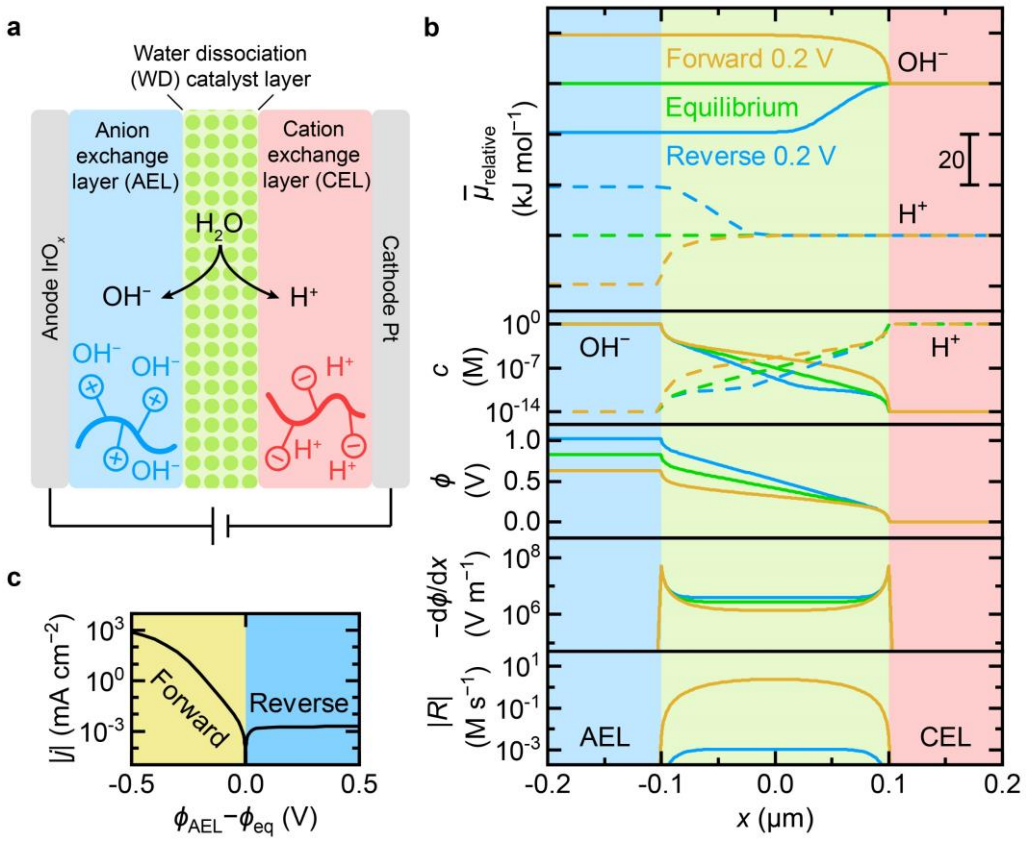

Figure 2.1 Properties of BPMs

a Schematic of a BPM electrolyzer. Pure water is fed through the anode and cathode gas-diffusion layers (GDLs) and diffuses into the AEL|CEL junction where water is dissociated with the aid of WD catalysts. **b** Steady-state numerical simulation results of a BPM at equilibrium (green), in forward bias 0.2 V (orange), and in reverse bias 0.2 V (blue). From top to bottom are the profiles of relative electrochemical potential $\bar{\mu}_{\mathrm{relative}}$, molar concentration c, electric potential ϕ, electric field $-\mathrm{d}\phi/\mathrm{d}x$, and magnitude of the net reaction rate $|R|$ (sum of dissociation and recombination). At equilibrium, the electrochemical potentials of each mobile species are the same across the whole BPM. **c** Simulated polarization curve of a BPM in forward bias and reverse bias. See Methods for more information.

Water dissociation (WD, $H_2O \rightarrow H^+ + OH^-$) in reverse bias, and H^+/OH^- recombination in forward bias, are key to BPM function. Despite recent advances[8, 17-22], the mechanism(s) of

WD in BPMs, and many of the factors critical to controlling the WD kinetics, remain unclear. Kunst and Lovreček appear to be the first to explain high rates of WD (relative to bulk water) *via* electric-field enhancement at the AEL|CEL interface *via* the second Wien effect[23], but conclude that the field strength is too small to explain the high observed currents[24]. Simons then proposed a proton-transfer WD-catalysis mechanism at tertiary amino groups on the AEL at the BPM junction[25-26]. Strathmann *et al.* argued that only with a relative permittivity of water <10 at the AEL|CEL interface can the enhanced WD rate be explained by the second Wien effect, and that the ideal pK_a for WD catalysis *via* proton transfer is ~7, assuming a single type of acid/base group in the AEL|CEL junction[27]. Abdu *et al.* controlled the BPM junction WD activity and ionic selectivity with layer-by-layer deposited polyelectrolytes[18]. Recently Yan *et al.* fabricated custom BPMs with different amounts of graphene oxide (GO) between the AEL and CEL as WD catalyst and proposed that the catalytic and electric-field-enhancement effects play counterbalanced roles in speeding WD[19]. The best performance they found was with the largest amount of GO in the range tested (4 layers, probably ~5 nm[28]). Oener *et al.* discovered a link between WD in electrocatalysis and BPMs and showed how the point of zero charge (PZC) of oxide nanoparticles correlates with the (seemingly pH-dependent) WD activity,[8] while also demonstrating dramatically improved BPM performance with metal-oxide nanoparticle bilayer films ~ 500 nm in thickness. However, the mechanistic details of WD remain unclear, particularly the exact role of the electric field in the junction for WD catalysts with varying electronic and dielectric properties as well as thicknesses (see Supplementary Discussion). This knowledge gap slows the design of higher-performance BPMs for key energy applications.

Here we uncover new BPM design principles derived from numerical simulations and measurements on well-defined custom BPM architectures with controlled WD catalyst loading, particle size, composition, and electrical properties. We find that for semiconducting nanoparticles such as TiO_2, there is a clear optimal range of loading/thickness, ~10-30 μg cm^{-2} (~200-600 nm in thickness), and particle size (20-30 nm), out of which the performance becomes substantially worse. For electronic conductors, including antimony-doped tin oxide (ATO), IrO_x, and Pt nanoparticles, the optimal loading is much higher (>100 μg cm^{-2}), and the optimal performance window is wider. Mobile electrons of the WD catalyst layer inside the (electrically disconnected) BPM junction appear to screen and focus the electric field to a narrow region at the AEL|WD-catalyst and WD-catalyst|CEL interface, speeding catalytic WD. Contrary to expectations, we find that TiO_2 with particle sizes < 20 nm decrease performance, despite providing a higher surface, which is also explained by electric-field effects. By collectively controlling these parameters, we demonstrate earth-abundant anatase TiO_2 WD catalyst layers that enable BPM pure-water electrolyzers that run at 500 mA cm^{-2} at record-low voltages below 2 V.

RESULTS AND DISCUSSION

Simulations to Inform Design Principles

We built a 1D numerical model with the minimum components to represent BPM features to illustrate design principles and help interpret experimental data. Taking H^+ and OH^- as the only mobile ions during pure-water operation (consistent with our experiments), we simulated profiles of relative electrochemical potential $\bar{\mu}_{\mathrm{relative}}$, molar concentration c, electric potential ϕ,

electric field $-\mathrm{d}\phi/\mathrm{d}x$, and net reaction rate R (Figure 2.1b). Changes in the AEL and CEL are small, so we focus on the junction region. The concentration of OH^- drops nearly exponentially from the AEL into the junction (notice the semi-log scale), and H^+ shows the same behavior at the CEL. This suggests that the ionic conductivity in the junction is small due to the low concentration of mobile H^+ and OH^- without added ionomers. Across the junction, ϕ drops nearly linearly with steeper slope (higher electric field) at the AEL|WD-catalyst and WD-catalyst|CEL interfaces due to screening.

The simulated polarization curve (Figure 2.1c) shows rectification of ionic current. In forward bias, H^+ and OH^- are driven into the junction by the gradients in electrochemical potential, leading to an increasing conductivity and their recombination to form water. In reverse bias, H^+ and OH^- are driven out of the junction, decreasing the concentration and thus ionic conductivity. The polarization curve approaches a limiting current density determined by, in this simulation, the product of the water dissociation rate constant k_f, the concentration of water in the junction, and the junction thickness. We note that ϕ drops almost entirely across the junction, since the ionic conductivity there is small compared with the AEL and CEL. Both the dissociation and recombination also occur almost exclusively in the junction region. We will return to this model in the context of the experimental data below.

WD Catalyst Layer Thickness/Loading Effects

Conventionally, BPMs are characterized in H-cells with soluble supporting electrolytes[1]. In such systems, the ionic current is due to transport of H^+ and OH^- from WD and of so-called "co-ions", *i.e.* electrolyte species like Na^+ or Cl^-. Differentiating between these two currents is

difficult, and often uncontrolled pH gradients form, complicating the analysis. We use electrolyzers in a membrane-electrode assembly (MEA) geometry fed by pure water and the current is thus carried exclusively by H^+ and OH^-. This MEA is under active compression so that no adhesives, interpenetrating 3D junctions, or other complicating interface structures are needed. This allows us to make fundamental discoveries as to the underlying physics and chemistry that govern the electrochemical response of BPMs and rationally design for higher performance. The total cell voltage reported includes the WD overpotential (η_{wd}), ohmic losses, and overpotentials due to charge-transfer (CT) reactions at the electrodes, *i.e.* the oxygen-evolution reaction (OER) and the hydrogen-evolution reaction (HER). To compare different WD catalysts, the electrodes, gas-diffusion layers (GDLs), HER catalyst (Pt), OER catalyst (IrO_x), assembly methods, temperature (55 ± 2 °C, maximum fluctuation), etc. are all kept identical (see Methods and Figure A.1 for detailed schematics).

We first studied TiO_2-P25 as a benchmark WD catalyst as it is commercially available at low cost, has good WD performance, and is chemically stable in both acid and base[8-9]. Increasing the spray-coated loading of TiO_2-P25 from 0 to ~18 μg cm^{-2} decreases the cell voltage, while higher loading increases the voltage (Figure 2.2a, Figure 2.2b, solid lines, and Figure A.2). The polarization curves are found to be nearly linear, consistent with catalyzed WD and a low driving force needed for WD. The reproducibility of the BPM electrolyzers is verified with ~18 μg cm^{-2} TiO_2-P25 samples at different testing dates with different batches of GDLs (Figure A.3). The cell voltage at 500 mA cm^{-2} is 2.05 ± 0.06 V (standard deviation across 7 samples).

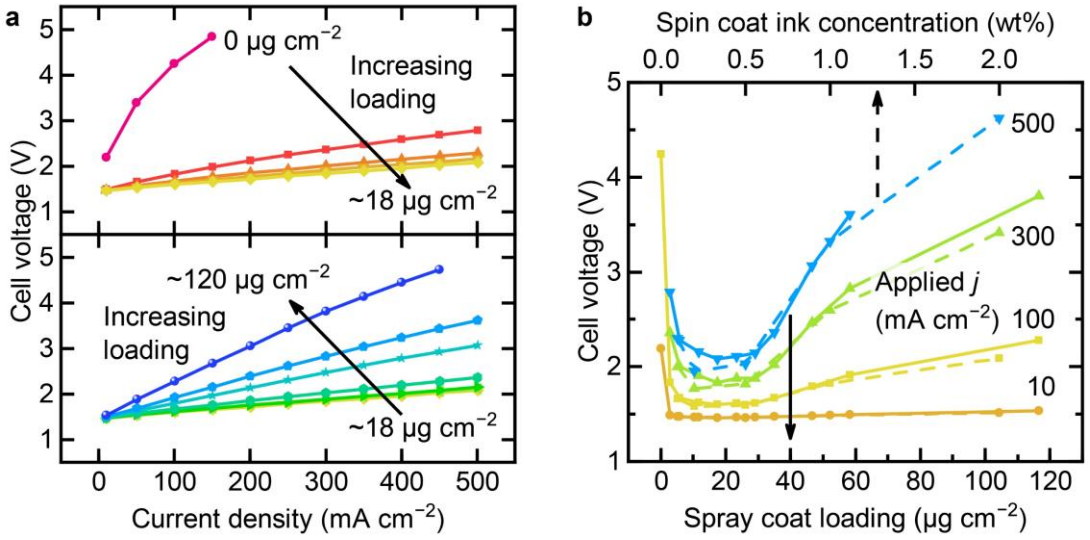

Figure 2.2 Performance of BPM electrolyzers with TiO_2-P25 as WD catalysts

a Polarization curves of BPM electrolyzers with different loadings of TiO_2-P25 WD catalyst deposited by spray coating. **b** Cell voltage of BPM electrolyzers as a function of spray-coating loading (solid lines) of TiO_2-P25 and spin-coating ink concentration (dashed lines) of TiO_2-P25 at different applied current densities. The 2.0 wt% sample is 1.0 wt% ink spun twice. The temperature is 55 ± 2 °C (maximum fluctuation).

The best-performing BPMs had incomplete coverage of spray-coated TiO_2-P25 (Figure 2.3), which led us to question whether this was important for function. We thus also spin-coated more-uniform TiO_2-P25 films and found a comparable loading dependence (Figure 2.2b, dash lines). The best performance was made from an ink with 0.2 wt% TiO_2, and resulted in the membrane uniformly covered with TiO_2-P25 at a thickness comparable to the spray-coated sample with ~18 μg cm^{-2} (Figure 2.3). With the 0.5 wt% ink, the performance is similar, and uncovered membrane regions are not evident. Uniform films are therefore capable, but not necessarily required, for high-performance WD in BPMs. The regions without WD catalyst coverage are likely inactive, as BPMs without WD catalysts require high voltages to pass current. Below we focus on data obtained from spray-coating (unless specified), as this method is

amenable to large-area processing and manufacturing.

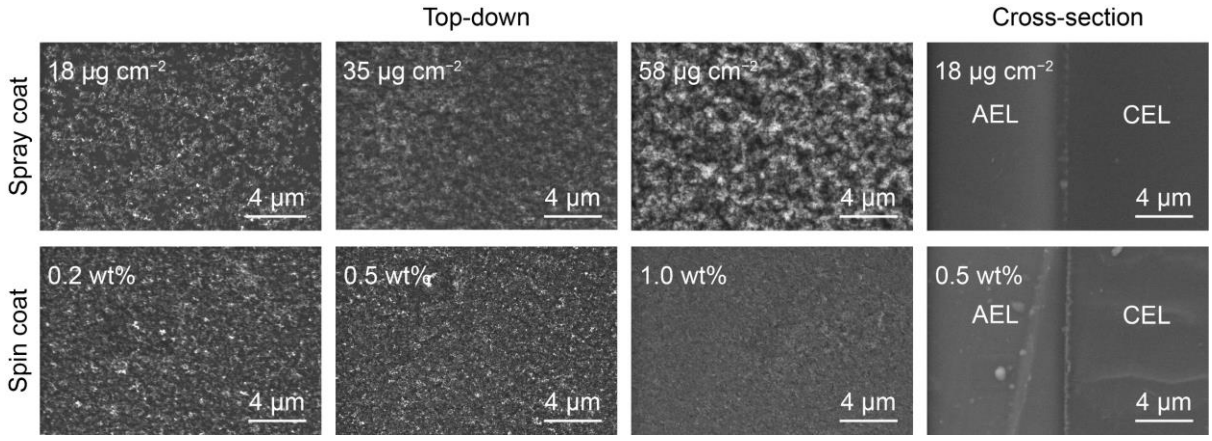

Figure 2.3 SEM images of TiO_2-P25 on the CEL and BPM cross-sections

For spray-coated samples, the approximate loadings are given while for spin-coated samples, the ink concentrations are given. The optimal spin-coated WD catalysts layers are smoother, with more-uniform coverage, but only marginally improved performance.

The U-shaped dependence of voltage on loading (Figure 2.2b) might be explained by the ionic resistance of the WD catalyst layer. The WD catalyst layer is composed of solid nanoparticles and liquid water. The ions must move in the liquid phase or by hopping across the particle surfaces. Nanoparticle surfaces are the putative active sites for WD, which generates ionic carriers, so increasing the loading would be expected to improve performance. However, as the thickness and packing density of the WD catalyst layer increase the transport lengths for OH^- and H^+ also increase leading to an expected increasing ohmic loss. The nanoparticles, however, also likely provide H^+ or OH^- from surface acid/base groups, therefore increasing the equilibrium ionic carrier concentration compared to pure water.

To assess this behavior, we modified our BPM simulation. We keep the ionization

constant of water K_w the same as in bulk water, but increase both WD rate constant k_f and H^+/OH^- recombination rate constant k_r (*i.e.* modelling a pure catalytic effect, with no change to the thermodynamics of the reaction). We simulate the total current density j at different voltages across the membrane as a function of distance between the AEL and CEL. The resulting current density as a function of junction thickness d (*i.e.* AEL-CEL distance) peaks, consistent with the experimental results (Figure 2.4a). With higher WD rate constants, the optimal thickness is smaller and the peak current is higher. Based on the model, better WD catalysts provide higher currents at lower loading where ohmic losses are minimized.

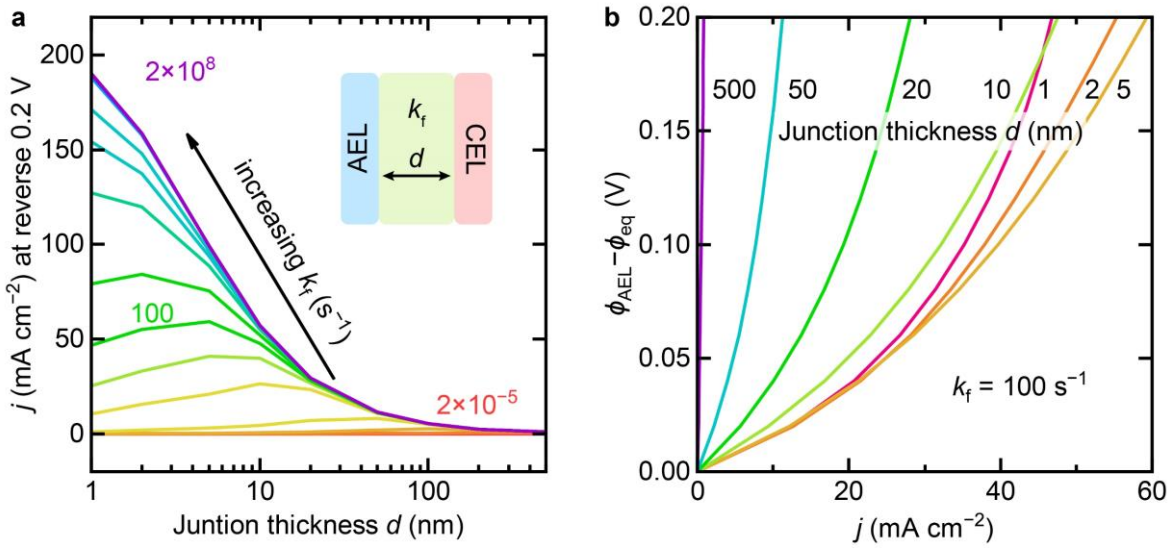

Figure 2.4 Steady-state numerical simulated results of BPMs with different junction thickness and WD rate constant

a Current density at reverse bias of 0.2 V as a function of junction thickness for different WD rate constants in the junction. **b** Polarization curves in reverse bias for different junction thickness with WD rate constant $k_f = 100$ s^{-1}. Similar results using the reported diffusion coefficients for H^+ an OH^- along with the fixed ion concentration in the membranes estimated based on the manufacturer specifications are in Figure A.4. See Methods for more information.

This model, however, has limitations. The simulated reverse bias polarization curves show that conductance (dj/dV) decreases with increased applied potential. Further, a limiting current density in reverse bias is evident when the junction thickness and WD rate constant are small (Figure 2.4b). The experimental results, however, show that the reverse-bias conductance increases with potential and approaches a constant (linear j-V response), and no limiting current density is apparent. This discrepancy suggests that the WD catalytic effect described by a constant, η_{wd}-independent rate constant is insufficient to explain the enhanced WD in BPMs. Further, the best WD catalyst thickness in our experiments is 200-600 nm, but with this thickness, the model cannot produce the high current densities observed in experiments, even with a large WD rate constant (see the curve of $k_f = 2\times10^8$ s^{-1} in Figure 2.4a, for comparison, in bulk water $k_f = 2\times10^{-5}$ s^{-1}). Previous simulation studies proposing WD driven by the second Wien effect used small junction thicknesses of usually < 10 nm, leading to large interfacial electric field, and assumed an electric-field-dependent WD rate constant to generate curves that roughly match experiment[29-31].

Impedance Analysis to Isolate WD Kinetics

To inform simulations and obtain quantitative information on the various CT, transport, and WD impedances of the BPM electrolyzer, we used electrochemical impedance spectroscopy (EIS).[7, 32] A typical Nyquist plot at 30 mA cm^{-2} with various TiO_2-P25 loadings shows two semicircles (Figure 2.5a). The lower frequency semicircle (right) is independent of the WD catalyst loading, while the one at higher frequency (left) is not. We keep the anode and cathode the same, so the CT impedances should be independent of WD catalyst loading. Thus, we

associate the high-frequency semicircle with WD in the BPM, and the low-frequency one with the electrode CT processes. Similar trends are observed at other current densities (Figure A.5). We construct an equivalent circuit (Figure 2.5a) composed of a series resistance (R_s) and two parallel *RC* circuits, to describe WD (R_{wd}) and CT (R_{ct}) accordingly, connected in series. We fit the impedance spectra using this equivalent circuit at 450 mA cm^{-2} (Figure 2.5b, and Figure A.6), and find that R_{wd} dominates the total resistance and is directly correlated with the cell voltage (Figure 2.2b). R_{ct} is essentially independent with the WD catalyst loading, as expected. R_s increases slightly with increasing loading (see below). Therefore, the linear increase of total voltage with current observed at higher currents in Figure 2.2a can be assigned largely to WD. However, from our equivalent-circuit model and impedance data, it is not clear whether the ionic resistance of the WD catalyst layer will be represented in R_s or R_{wd}.

The EIS data can also be used to estimate the WD overpotential η_{wd} and compare with reported values. To compare with an industry-standard Neosepta BPM (~1.2 V in H-cell at 100 mA cm^{-2} and 30 °C, $\eta_{wd} \approx 1.2\ \text{V} - 0.83\ \text{V} = 0.37\ \text{V}$)[33], we tested the BPM electrolyzer with optimal TiO_2-P25 loading (~18 μg cm^{-2}) at 30 °C (Figure A.7 and Supplementary Discussion). EIS analysis shows that R_{wd} decreases from ~0.96 Ω cm^2 to ~0.66 Ω cm^2 as current increases from 5 mA cm^{-2} to 500 mA cm^{-2} and we calculate $\eta_{wd} = \int_0^j R_{wd}(j)\mathrm{d}j$. At 100 mA cm^{-2}, η_{wd} is 0.09 V, four times lower than Neosepta. The performance of many other BPMs are compiled in literature[1, 8]. Most of the membrane voltages are well above 1 V at 100 mA cm^{-2} (η_{wd} > 0.2 V). Shen *et al.* used $Al(OH)_3$ in an electrospun 3D BPM junction and found η_{wd} ~0.2 V (estimated from the onset of the polarization curve) at 100 mA cm^{-2} at 25 °C [34]. Chen *et al.* reported an *iR*

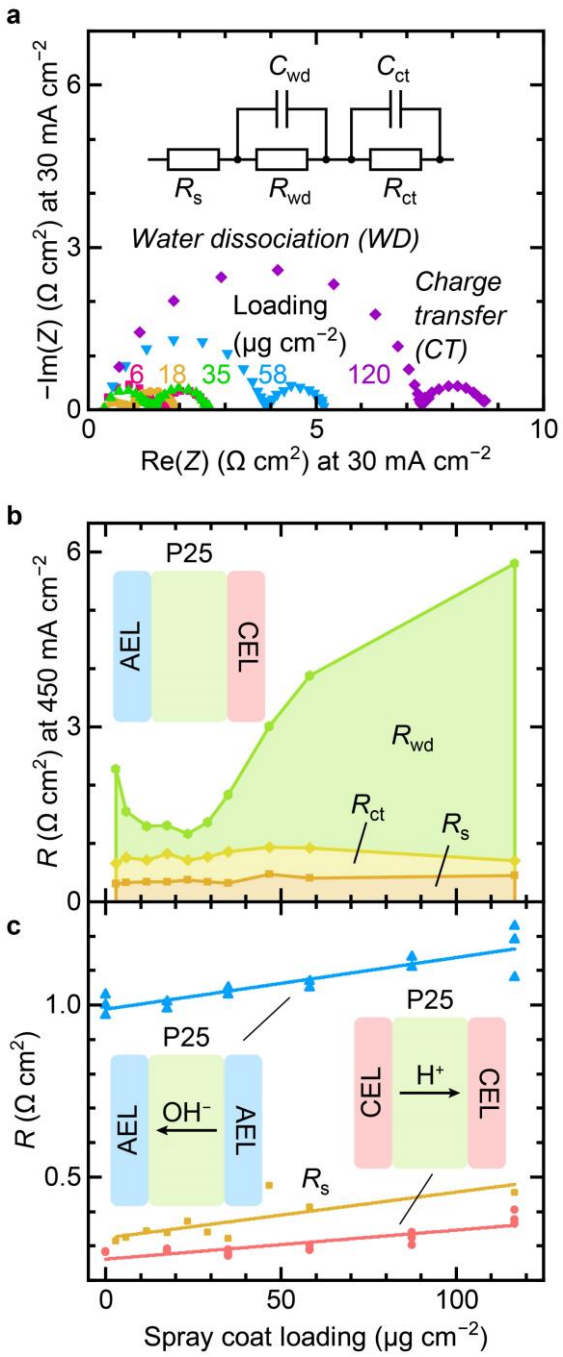

Figure 2.5 Impedance analysis of BPM electrolyzers

a Nyquist plots of BPM electrolyzers at 30 mA cm^{-2} with different loadings of TiO_2-P25 deposited by spray coating WD catalysts. The high frequency semicircle is assigned to WD, while the low frequency one to CT. The inset shows the equivalent circuit used to fit the EIS data. **b** Extracted resistance values at 450 mA cm^{-2} as a function of TiO_2-P25 loading. **c** Comparison of series resistance R_s (orange) extracted from BPM electrolyzer EIS data at 450 mA cm^{-2} with the resistance of PEM (red) and AEM (blue) electrolyzers at 300-500 mA cm^{-2} as a function of TiO_2-P25 loading.

free voltage of 1.5 V at 500 mA cm^{-2} at ~25 °C using graphene oxide WD catalyst[21], which is η_{wd} ~0.7 V compared to η_{wd} ~0.38 V under the similar conditions for our systems. By increasing temperature, as in Figure 2.2, here η_{wd} is substantially reduced to, e.g., only 0.24 V at 500 mA cm^{-2} and 55 °C. The systems we studied are nominally 2D BPMs and we focused specifically on the WD catalytic processes. The developments we report are orthogonal to the progress made in, for example, electrospinning of 3D-junction BPMs. We expect that if controlled WD catalyst layers like reported here can be integrated into 3D electrospun BPMs, further performance enhancements will be possible.

Ion Transport in the WD Catalyst Layer

To measure the ionic conductivity in the WD catalyst layer, we built proton-exchange-membrane (PEM) and anion-exchange-membrane (AEM) electrolyzers where the TiO_2-P25 layers were sandwiched between either two identical CELs or AELs (Figure 2.5c, and Figure A.8). We measured electrolyzer polarization curves and fit the region from 300 to 500 mA cm^{-2} to a line to obtain the differential resistance. At these high currents, the differential resistance is dominated by ionic transport (both HER and OER rates increase exponentially with overpotential). Because only H^+ transports through the TiO_2-P25 layer in PEM electrolyzers and only OH^- through TiO_2-P25 in AEM electrolyzers, we are able to measure the ionic conductivity of H^+ and OH^- in the TiO_2-P25 layer separately. As the TiO_2-P25 WD catalyst loading increased from 0 to ~120 μg cm^{-2} (a ~2.4-μm-thick film) the resistance of PEM electrolyzers increases by only ~0.10 Ω cm^2, while for AEM electrolyzers only ~0.17 Ω cm^2. Based on this data, we estimate the ionic conductivity of the TiO_2-P25 layer to be ~2.4 mS cm^{-1} for H^+ and ~1.4 mS

cm^{-1} for OH^- at 55 °C. Assuming equivalent conductivities of H^+ and OH^- in the water/TiO_2-P25 WD-catalyst layer as in pure water, and neglecting temperature and concentration effects, these results give an average concentration of H^+ and OH^- in the TiO_2-P25 layer of ~7 mmol L^{-1}. In comparison, the conductivities of Nafion 212 and PAP-TP-85 at 60 °C are both over >50 mS cm^{-1} [35-36]. From the impedance analysis, we find that the change of R_{wd} is ~5 Ω cm^2 from ~18 to ~120 μg cm^{-2} (~360 nm to ~2.4 μm) but the change in the ionic resistance of the TiO_2-P25 layer is only ~0.10 or ~0.17 Ω cm^2. This demonstrates that a simple increase in ionic resistance due to the WD catalyst layer thickness cannot explain the decrease in BPM performance for WD catalyst loadings above the optimum. Interestingly, we also find that the increase in differential resistance in the reference AEM and CEM electrolyzers is comparable to the increase of R_s (~0.15 Ω cm^2) measured by impedance in BPM electrolyzers as the WD catalyst loading is increased (Figure 2.5c). This result indicates that the ionic resistance of the WD catalyst layer is represented as a component of R_s in the equivalent circuit and not R_{wd}. This impedance data thus shows that it is possible to confidently separate the ionic transport, charge transfer, and WD resistances *via* EIS analysis, which is of significant value in optimizing systems.

WD Catalyst Surface Area

Previously, Oener *et al.* studied the WD activity of various metal-oxide nanoparticles with similar diameters[8]. An obvious hypothesis is that smaller nanoparticles of the same metal oxide will have better WD performance because of higher specific surface area (SSA, see Methods and Table A.1 and Table A.2). We studied the loading dependence with nominally 5, 15, 30, and 100 nm anatase and 30 nm rutile particles (Figure 2.6a, and Figure A.2). The 5, 15, and

30 nm anatase shows the U-shaped voltage response with loading, indicative of an optimal loading between 10 and 30 μg cm^{-2}. The performance of 100-nm anatase and 30-nm rutile TiO_2, however, continues to improve with loading to much higher values. If we compare the performance of each WD catalyst at its optimal loading, the 30 nm anatase and TiO_2-P25 (around ~20-30 nm, ~80% anatase) are substantially better than the 5-nm anatase even though the 5-nm particles have an SSA seven times that the 30-nm ones (Table A.2). This surprising result contradicts typical behavior of heterogeneous catalysts where higher SSA yields higher activity.

Field Effects on Water Dissociation

These unexpected results led us to consider in more detail the second Wien effect (see Supplementary Discussion). According to Onsager's theory, the WD rate increases nearly exponentially with the electric field. If the electric field is "concentrated" in some regions of the BPM junction, the overall WD rate might be higher than if the field is averaged across the whole junction. In fact, Chen *et al.* suggested that WD might be enhanced by using electronically conducting materials (see Supplementary Discussion)[20]. We further studied the loading dependence of electronically insulating materials like SiO_2, as well as conductive materials such as antimony-doped tin oxide (ATO), IrO_x, and Pt (Figure 2.6a and Figure A.9). SiO_2 is the worst WD catalyst. ATO, IrO_x, and Pt all show good performance, but with much higher mass loading than anatase TiO_2. We measure the apparent electronic conductivities of these nanoparticles (using a simple two-probe setup, see Methods) and correlated those with their performance in BPM electrolyzers (Figure A.10). Better performance is generally observed for nanoparticles with higher electronic conductivity (although electronic conductivity is clearly not the only

important parameter, *e.g.* the acid-base properties of the surface are also critical to the catalytic effect[8], as is the loading, etc.).

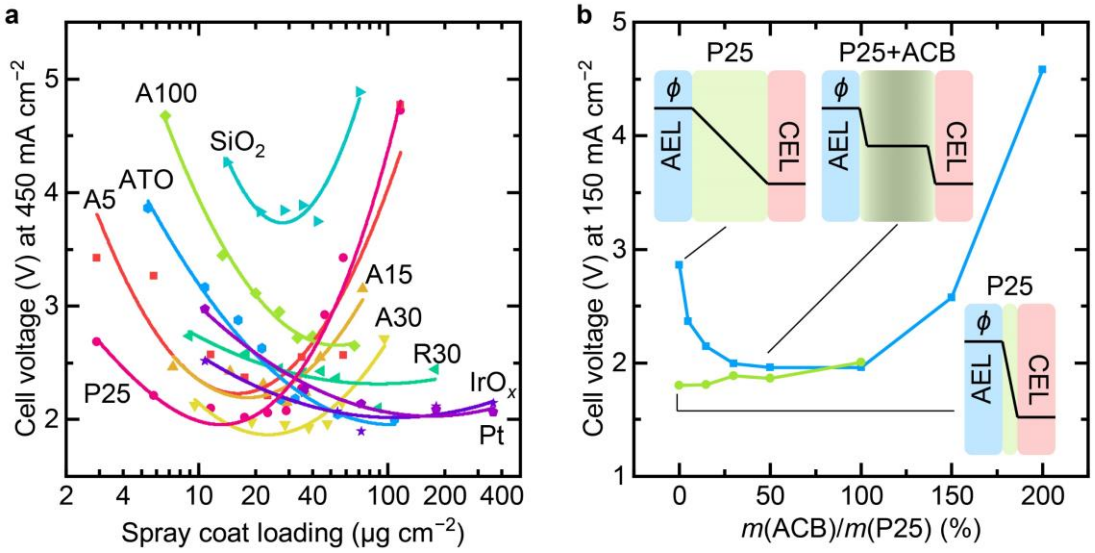

Figure 2.6 Performance of BPM electrolyzers with various WD catalysts

a Cell voltage of BPM electrolyzers as a function of spray-coated loading of various WD catalysts at 450 mA cm^{-2}. Lines are added to serve as a guide for the eye. For various TiO_2, A = anatase and R = rutile. The number denotes the size of the nanoparticles (nm) provided by the manufacture. ATO = Sb:SnO_2. **b** Cell voltage of BPM electrolyzers as a function of the mass ratio of acetylene carbon black (ACB) and TiO_2-P25 at 150 mA cm^{-2}. The blue line is for a thick layer of ~120 μg cm^{-2} (~2.4 μm) TiO_2-P25, and the green line is for a thin layer of TiO_2-P25 at optimal loading ~18 μg cm^{-2} (~360 nm). Only one of each type of device was fabricated for the data in this figure to illustrate trends, except for P25 TiO_2. The error was estimated to be less than 5% (one standard deviation) based on seven devices fabricated with the best loading of TiO_2-P25 catalysts (Figure A.3). Insets are schematic proposed electric-potential profiles across the BPM junction.

Based on this data, we hypothesized that adding electronically conductive carbon to the TiO_2-P25 would improve performance in situations where that WD catalyst layer was too thick – and thus the electric field is too small with the electrochemical potential drop smeared out across the junction – by concentrating the electrochemical potential drops and electric field to the

interfacial regions. We added different amounts of acetylene carbon black (ACB) nanoparticles, an electronic conductor, to BPMs with the most TiO_2-P25 (~120 μg cm^{-2}, ~2.4 μm thick) and measured BPM electrolyzer performance (Figure 2.6b, blue curve, and Figure A.11). The WD performance is substantially improved after adding ACB at a mass ratio near 1:1. We also tested ACB and TiO_2-P25 mixtures at the previously determined optimal loading (~18 μg cm^{-2} and ~360 nm). For these thinner WD catalyst films, no performance improvement was observed (Figure 2.6b, green curve, and Figure A.11). ACB alone was a poor WD catalyst (Figure A.12). These experimental results are consistent with the mobile electrons in the conductive WD catalyst polarizing the WD catalyst layer in response to the net electric potential drop across the junction, with a positive electronic charge on the junction side facing the CEM and negative electronic charge on the AEM side. As a result, the electric potential drop is focused into a narrow region at the AEL|WD-catalyst and WD-catalyst|CEL interfaces. Based on Onsager's theory, the resulting increased field would increase the rate of WD almost exponentially in that region. The excess WD catalyst in the middle of the WD catalyst film then simply adds a series resistance (shown to be small by the ionic conductivity experiments above). For optimally thin WD catalyst, however, the electric field is apparently already sufficiently strong that the addition of ACB reduces performance (*e.g.* by reducing density of WD active sites).

Stability

We tested the stability of the BPM electrolyzer with the best loading (~18 μg cm^{-2}) of TiO_2-P25 at 500 mA cm^{-2} for 36 h at 55 °C (Figure A.13). The voltage was found to increase at ~15 mV h^{-1} for the first 18 h and at ~6 mV h^{-1} after that, comparable to what we observed in

AEM electrolyzers[37]. This data suggests a similar degradation mechanism, i.e. ionomer degradation at the alkaline anode evolving O_2. In the Nyquist plots collected at 30 mA cm^{-2} every 6 h, the initial two semicircles evolved into three semicircles. Equivalent circuit fits show that R_s is constant and R_{wd} slightly increased (~1.7 mΩ cm^2 h^{-1}) over 36 h, indicating good stability of the water-dissociating BPM junction. In contrast, the total charge-transfer resistance R_{ct1} + R_{ct2} increased from ~1.1 Ω cm^2 to ~3.3 Ω cm^2, consistent with the expected anode degradation.

SUMMARY AND OUTLOOK

We elucidated the key roles of electronic and ionic conductivity of the WD catalyst within the BPM junction enabling record BPM-electrolyzer performance with pure-water feed. For semiconducting WD catalysts such as TiO_2, there is an optimal range of loading/thickness, 10-30 μg cm^{-2} (200-600 nm in thickness), while for electronic conductors, the optimal is higher and the range larger. Reference measurements in proton-exchange-membrane and anion-exchange-membrane electrolyzers show that, surprisingly, the ionic resistance of the WD catalyst layer is relatively unimportant, even for TiO_2 films ~2 μm in thickness. Combining conductive carbon nanoparticles with thick TiO_2 WD catalyst layers dramatically improves performance compared to either component in isolation, apparently by focusing the junction electric field. Impedance analysis enables clear separation of ionic transport, anode/cathode, and WD resistances and supports these conclusions. These data show that WD catalysts operate *via* mechanisms that are more complex in high-electric-field BPM junctions compared to conventional heterogeneous chemical catalysts. Not only do "intrinsic activities" matter – probably governed by acid/base and surface-chemical properties – but properties like the dielectric constant and electrical

conductivity of the WD catalyst play a key role in affecting interfacial junction physics and WD rate.

Additional work is needed to fully understand the WD mechanism in BPMs. Particularly useful would be experiments to map the concentration profiles of H^+ and OH^- and the electric field within the BPM junction and correlate this to WD rates. Measuring such profiles for WD catalysts of different compositions and layering schemes would be useful to understand the molecular details of the catalysis process, including the specific chemical sites where WD occurs. Studying the reverse reaction, H^+ and OH^- recombination, and whether that process can also be catalyzed following the same mechanistic principles as WD would also be of fundamental interest and important for new BPM applications. Such advances are important for the design of optimized WD catalysts and BPMs based on the electronic, ionic, surface-chemical, transport, and other materials properties. Finally, the high current density and low resistance of the BPM electrolyzers reported here using only earth-abundant WD catalysts are impressive in their own right. This will be likely to benefit the applications highlighted in the introduction, among others. Further improvements are likely by combining optimized catalytic layers with 3D interpenetrating BPM junctions developed by others[34].

METHODS

Cell fabrication and measurements

The gas diffusion layers (GDLs) are fabricated by spray coating. The anode ink is prepared in a 20 mL scintillation vial with 0.1 g IrO_x (Pajarito Powder) or Core/Shell Ir/IrO_x (Fuel Cell Store), 0.5 g H_2O, 1.7 g isopropyl alcohol (IPA), 0.1 g PiperION-A5 Ionomer Suspension

(TP-85, 5% w/w, Versogen). The ink is sonicated until the nanoparticles are well dispersed. The substrate for the anode GDL is stainless steel 25AL3 (Bekaert Bekipor®). The substrate is cut into a square of 5 cm × 5 cm and taped on a hot plate of 90 °C. Two vials of the ink are spray coated on the substrate. The loading of the catalyst is ~2 mg cm^{-2}. Then PiperION-A5 Ionomer Suspension is sprayed on top of the catalysts layer until the mass of the ionomer reaches 10 % ~ 20 % the catalyst mass. Finally, the GDL is cut into squares of 1.0 cm × 1.0 cm for later use. For PEM electrolyzers, platinized Ti-fibre felt (Fuel Cell Store) is used as substrate instead of stainless steel to prevent corrosion under acidic and anodic conditions.

The cathode ink is prepared in a 20 mL scintillation vial with 0.1 g Pt black (high surface area, Fuel Cell Store), 1.5 g H_2O, 1.7 g IPA, 0.1 g D520 Nafion™ Dispersion (alcohol-based 1000 EW at 5 wt%, Fuel Cell Store). The ink is sonicated until the nanoparticles are well dispersed. The substrate for the GDL is Toray Carbon Paper 090 (value pack, wet proofed, Fuel Cell Store). The substrate is cut into a square of 5 cm × 5 cm and taped on a hot plate of 90 °C. Two vials of the ink are spray coated on the substrate. The loading of the catalyst is ~2 mg cm^{-2}. Then D520 Nafion™ dispersion is sprayed on top of the catalyst layer until the mass of the ionomer reaches 10 ~ 20 % the catalyst mass. The GDL is the cut into squares of 1.0 cm × 1.0 cm for later use.

PiperION-A40-HCO3 (TP-85, 40 μm, Versogen) is used as the anion exchange layer (AEL). The membranes are pre-treated according to the manufacturer instructions. The AEL is soaked in 0.5 M KOH for > 1 h, stored in fresh 0.5 M KOH, and rinsed in ultra-pure H_2O before use. Nafion™ 212 (Fuel Cell Store) is used as the cation exchange layer (CEL). According to the

manufacturer, the membrane comes in a pre-protonated state and does not need additional pre-treatment. Thus, the CELs are soaked and stored in H_2O. Both membranes are cut into squares 1.5 cm × 1.5 cm before use.

The measured and manufacturer-provided properties of all the WD catalyst nanoparticles studied are listed in Table A.1 and Table A.2. These nanoparticles were spray coated from an ink onto the CEL. A mother ink of 2 wt% is prepared in H_2O and sonicated until the nanoparticles are well dispersed. The ink for spray coating is made by diluting this mother ink. Different masses of the mother ink are transferred to a 20 mL scintillation vial. H_2O is added until the total mass reaches 0.5 g, and then 1.7 g IPA is added. For high loading of IrO_x and Pt, the amount of H_2O and IPA is increased to aid dispersion. This diluted ink is sonicated until the nanoparticles are well dispersed before spray coating. The Nafion membrane is cut into a square of 1.5 cm × 1.5 cm and taped in the bottom of a glass petri dish so that the exposed area is 1.2 cm × 1.2 cm. Then the petri dish is placed on a hot plate at 90 °C. The diluted ink is spray coated onto the CEL. To improve uniformity, the petri dish is rotated 90° every 10 spray bursts. After the spray coating, the petri dish is removed from the hot plate, and the tape is removed carefully to prevent damage to the CEL. H_2O is added around the CEL so that it absorbs water and delaminates from the petri dish. The coated CEL is transferred to a container with H_2O before use.

For the spin-coated samples, a mother ink of 10 wt% TiO_2-P25 in water/IPA mixture (1:1 by weight) is prepared. The mother ink is horn sonicated for 10 min and filtered through a 5 μm syringe filter to remove larger aggregates (Acrodisc® 32 mm syringe filter with 5 μm Supor® membrane). The mother ink is diluted with water/IPA mixture (1:1 by weight) to make the spin

coating inks of the concentrations indicated. The CEL is cut into a square of 1.5 cm × 1.5 cm and its edges are taped on a glass slide for spin coating. Drops of the ink are added on the membrane until it is fully covered. The membrane is then spun at 3000 rpm for 30 s. The 2.0 wt% sample is made by spin coating two layers of the 1.0 wt% ink.

The electrolyzer was built from PEM fuel-cell hardware (Fuel Cell Store). A homemade stainless-steel flow field was used instead of the original graphite anode. The gaskets used in the assembly have an active area of 1.0 cm × 1.0 cm. To assemble the electrolyzer, several gaskets with a total thickness of 0.032″ are placed on top of the cathode flow field, and one Ti spacer (sintered Ti frits electroplated with 1 μm Pt, 1 cm × 1 cm, Baoji Yinggao Metal Materials Co., Ltd.) is placed in the square hole of the gasket, followed by the cathode GDL, with the HER catalyst side facing up. The BPM is then placed on top of the cathode GDL with WD catalyst sandwiched between the CEL and AEL. The CEL is in contact with the cathode GDL. After that, several gaskets with a total thickness of 0.037″ are placed around the BPM. The anode GDL is then placed in the square hole of the gasket with the OER catalyst facing the AEL. A second Ti frit spacer is then placed on top of the anode GDL. Finally, the anode flow field and current collector is bolted together to seal the system. The bolts are tightened by a torque wrench to 50 inch-pounds. Pure de-ionized H_2O heated at 60 °C is fed to both the anode and cathode. The electrochemical tests are started after the cell hardware reaches the equilibrium temperature (55 ± 2 °C, maximum fluctuation) using a BioLogic VSP-300 potentiostat.

The current density is first held at 10 mA cm^{-2} for 1 min, then stepped from 50 to 500 mA cm^{-2} with 50 mA cm^{-2} steps (1 min each step), and finally held at 500 mA cm^{-2} for 10 min.

For the BPMs with ACB, a larger voltage was observed during the initial steps of increasing current density, so the current steps were maintained for 1-70 min instead. Finally, the current density was stepped down in the reverse order and the voltage at each step was measured. The reported polarization curves are generated from the average voltages measured over the last second of each current step. The current is then stepped up again (10 s each step and then held at 500 mA cm^{-2} for 1 min) to prepare for electrochemical impedance spectroscopy (EIS). Impedance data are recorded at each current density step from 500 mA cm^{-2} down to 50 mA cm^{-2} with 50 mA cm^{-2} steps, as well as current densities of 40, 30, 20, 10 and 5 mA cm^{-2}. An AC amplitude of 6% of the applied DC current density is used from 500 to 20 mA cm^{-2}. For 10 and 5 mA cm^{-2}, the AC amplitude is 1 mA cm^{-2}. The frequency was scanned from 600 kHz to 20 mHz with 4 points per decade. Most of the EIS data are fitted using Bio-Logic EC-Lab V11.33. The stability EIS data were fit using impedance.py[38].

To support the formation of H_2 and O_2 in a 2:1 ratio and show near-unity Faradaic efficiency, we measured the amount of evolved gas with graduated cylinders at room temperature (22 °C, Figure A.14). Before passing current, two graduated cylinders (50 mL for O_2 and 100 mL for H_2) are filled with water and placed upside down in the water tank (total volume of water is ~5.5 L). The gas bubbles are generated at the electrodes under high local supersaturation during electrolysis and carried by the water flow (~100 mL min^{-1} for the anode and ~60 mL min^{-1} for the cathode) for collection in the inverted graduated cylinders in about 10 s. After the electrolysis, the volume of the gas is read by leveling the water inside the graduated cylinders with the water in the tank. We applied 500 mA for 20 min, and the theoretical volumes of H_2 and O_2 are 75.30

mL and 37.65 mL, while the experimental values are 75.5 ± 0.5 mL and 37.0 ± 0.5 mL (uncertainty of the graduated cylinder). Thus, the Faradaic efficiency is ~100% for H_2 and ~98% for O_2. Given the short transit time between bubble detachment at the electrode and collection in the cylinder, little O_2, and negligible H_2, is apparently lost due to dissolution in the recirculating water. The smaller O_2 Faradaic efficiency might also be due in part to oxidation of ionomer, as we have discussed and shown to limit durability of current alkaline-membrane pure-water electrolysis systems[37]. SEM images of a BPM after testing in the electrolyzer are shown in Figure A.15. No evidence for membrane breaking or cracking is observed.

Quantifying the loading and thickness of WD catalysts

Microscope cover-glass slides were used as substrates to quantify the loading and thickness of TiO_2-P25 because membrane mass is highly sensitive to water content and changes over the course of the measurement and processing. The ink is spray coated on the same sized cover glass as membrane (1.2 × 1.2 cm^2) and the mass change is measured using a semi-microbalance (Sartorius Quintix™, see Figure A.16). We found that the rate of TiO_2-P25 WD catalyst deposition was 27 ± 3 μg cm^{-2} (standard error of fitting) per mg of ink in the spray-coating solution. The thickness is then determined by cross-sectional environmental scanning electron microscopy (ESEM, pressure of 40 Pa in H_2O) and energy-dispersive X-ray spectroscopy (EDS) mapping (ThermoFisher Apreo 2S). The EDS signal of Ti is integrated and plotted as a function of position. A Gaussian function is used to fit the curve and the full width at half maximum (FWHM) is used to represent the thickness (Figure A.16). We found that the films were 0.59 ± 0.09 μm (standard error of fitting) in thickness per mg of TiO_2-P25 WD catalyst in

the ink. We thus conclude that for the best performance case (0.6 mg TiO_2-P25 in ink), the WD catalyst loading is ~18 μg cm^{-2} and the thickness is ~360 nm. The loadings of other WD catalysts are determined using a similar calibration method. The BPM cross-section samples are prepared by immobilization (LR White resin) and microtoming.

N_2 adsorption-desorption experiments

Nitrogen (N_2) adsorption/desorption isotherms were obtained at 77 K using Micromeritics ASAP 2020 surface area analyser. Specific surface areas (SSA) of the samples were calculated using Brunauer-Emmett-Teller (BET), while the pore volume (V_p) was calculated using the Barrett, Joyner, and Halenda (BJH) adsorption curves. Before measurements, the TiO_2 nanoparticles were dispersed in hexanes and dried at room temperature under vacuum for 18 h. Prior to analysis, the samples were activated at 423 K for at least 24 h to remove the solvent and trapped gas. Activation was considered complete when the outgassing rate fell below 2.5 μtorr min^{-1}. The sample mass was determined by the difference in mass between the empty sample tube and the loaded sample tube post-activation. Based on IUPAC classification, all TiO_2 nanoparticles showed type-III isotherms, which are indicative of macroporous materials. In all samples, a type H_3 hysteresis was observed demonstrating macroporosity with narrow slit-like pores.[39] BET surface areas and calculated pore volumes are given in Table A.2.

Electronic conductivity

The apparent electronic conductivities of WD catalysts are measured using a simple two-electrode setup. A pellet of the nanoparticles is made with a die and press (Quick Press Sigma-Aldrich®) and a homemade polyether-ether-ketone (PEEK) collar. Then the metal plungers on

the press are used as the two electrical contacts to measure the current-voltage response of the compressed powder pellet. A polarization curve is collected between ± 0.1 V at 5 mV s^{-1}. The curve is fitted linearly to extracted the apparent electronic conductance G. The apparent electronic conductivity κ is calculated by $\kappa = \frac{Gl}{A}$, where G is the conductance extracted from the current-voltage response, l is the thickness of the pellet determined by the difference of the length of the die set with and without the nanoparticles measured by a caliper, $A = 0.4\ \mathrm{cm}^2$ is the area of the pellet.

Numerical simulations

The BPM model was built in COMSOL Multiphysics® 5.5 with only two mobile ions, H^+ and OH^-, consistent with the BPM electrolyzer devices. The simulation model is built with the least-possible components, including reaction (catalytic and non-catalytic), transport (diffusion and migration), and the physical dimensions of the system such as the junction thickness. The purpose of the model is *i*) to illustrate the underlying fundamental physics of how the various potentials develop under operation to provide a framework for understanding how the introduction of catalytic materials with different dielectric properties can modulate this picture, and *ii*) to illustrate the fundamental trade-off between ionic resistance and catalyst loading in the junction in the context of the experimental data. It would be straightforward to increase the complexity of the model to include a series of chemical reaction steps for the catalysts, hypothesized electric-field effects explicitly, variable surface charge on the catalyst particles, etc. Yet doing so would not provide new insight and would likely make the model less useful due to the large numbers of adjustable parameters which are not known based on

experiment. Regardless of the mechanistic details, the net result is that in reverse bias H_2O is dissociated into H^+ and OH^-. We thus write k_f as the net forward WD rate constant, and k_r as the net reverse (recombination) rate constant. For simplicity, we treat activity coefficients as unity and use concentrations for the equilibrium constant. At equilibrium,

$$K_{eq} = \frac{c_{H^+} c_{OH^-}}{c_{H_2O} c^\circ} = \frac{K_w c^\circ}{c_{H_2O}} = \frac{k_f}{k_r c^\circ} \tag{2.1}$$

where K_{eq} is the equilibrium constant, c_i is the molar concentration of species i, $c^\circ = 1\ \text{mol L}^{-1}$ is the reference molar concentration, and K_w is the ionization constant of water (10^{-14} at 25 °C). We take $c_{H_2O} = 55.6\ \text{mol L}^{-1}$ as a constant. k_r has been determined experimentally in pure water using a high-voltage impulse[40]: $k_r = (1.3 \pm 0.2) \times 10^{11}\ \text{L mol}^{-1}\ \text{s}^{-1}$ (at 25 °C). Therefore, the WD rate constant can be calculated (in bulk, free water) as

$$k_f = \frac{K_w k_r (c^\circ)^2}{c_{H_2O}} \approx 2 \times 10^{-5}\ \text{s}^{-1}\ (\text{at } 25\ ^\circ\text{C}) \tag{2.2}$$

We built a 1-D geometry composed of three consecutive intervals, representing the AEL, the WD catalyst layer (junction), and the CEL accordingly from left to right (Figure 2.1b). The thicknesses of AEL and CEL are both fixed to be 50 μm, while the thickness of the junction d was varied. Transport of species i is driven by the gradient in electrochemical potential $\bar{\mu}_i$. The continuity equation (mass balance) at steady state requires that $\boldsymbol{\nabla} \cdot \boldsymbol{J}_i = R_i$, where $\boldsymbol{J}_i$ is the flux, and R_i production rate of species i, calculated by

$$R_{H^+} = R_{OH^-} = k_f c_{H_2O} - k_r c_{H^+} c_{OH^-} \tag{2.3}$$

Ignoring concentrated electrolyte effects, $\boldsymbol{J}_i$ is given by the Nernst–Planck equation (without convection)

$$\boldsymbol{J}_i = -\frac{c_i D_i}{RT}\boldsymbol{\nabla}\bar{\mu}_i = -D_i\boldsymbol{\nabla}c_i - \frac{c_i D_i z_i F}{RT}\boldsymbol{\nabla}\phi \quad (2.4)$$

where D_i is the diffusion coefficient (assumed to be 10^{-4} cm^2 s^{-1} for both H^+ and OH^- for simplicity, while in Figure A.4, $D_{H^+} = 9.311 \times 10^{-5}$ cm^2 s^{-1}, and $D_{OH^-} = 5.273 \times 10^{-5}$ cm^2 s^{-1} [41]), z_i is the charge number, ϕ is the electric potential. F, R, and T denote Faraday's constant, the gas constant, and temperature respectively. Poisson's equation is used to couple the charged species with electric potential

$$\boldsymbol{\nabla}^2\phi = -\frac{F[\sum c_+ - \sum c_-]}{\varepsilon_0\varepsilon_r} \quad (2.5)$$

where c_+ is the molar concentration of positive charges (e.g. H^+, and fixed charges in AEL, set to be 1 mol L^{-1}, while in Figure A.4 set to be 2.4 mol L^{-1} [35]), and c_- is the molar concentration of negative charges (e.g. OH^-, and fixed charges in CEL, also set to be 1 mol L^{-1}, while in Figure A.4 set to be 1.8 mol L^{-1} [31]). ε_0 is the vacuum permittivity and $\varepsilon_r = 78$ is the relative dielectric constant of bulk water. For the outer boundary of the CEL, we assume $c_{OH^-} = 10^{-14}$ mol L^{-1}, $c_{H^+} = 1$ mol L^{-1} (in Figure A.4 $c_{OH^-} = 10^{-14}/1.8$ mol L^{-1}, $c_{H^+} = 1.8$ mol L^{-1}), and set $\phi = 0$ V. For the outer boundary of the AEL, we assume $c_{OH^-} = 1$ mol L^{-1}, $c_{H^+} = 10^{-14}$ mol L^{-1} (in Figure A.4 $c_{OH^-} = 2.4$ mol L^{-1}, $c_{H^+} = 10^{-14}/2.4$ mol L^{-1}), and ϕ is variable. At equilibrium, ϕ at the outer boundary of AEL can be derived by equating $\bar{\mu}_i$ at two boundaries:

$$\phi_{eq} = \frac{RT}{z_i F}\ln\frac{c_i(\text{CEL})}{c_i(\text{AEL})} \approx 0.83 \text{ V (at 25 °C)} \quad (2.6)$$

whether calculated by H^+ or OH^-.

The mesh was defined by the maximum element size with denser elements at the interfaces. In AEL and CEL it is 1,000 times smaller than the membrane thickness. In the junction, it is 100 times smaller than the junction thickness. At the WD-catalyst|AEL and CEL|WD-

catalyst interfaces it is 10,000 times smaller than the junction thickness.

BRIDGE

Chapter II includes studies of water dissociation catalyst type and loading dependence in bipolar membranes, the electrochemical impedance analysis (EIS), and the effect of ionic and electronic conductivity. It forms the vital basis of Chapter III where the catalyst loading dependence and the effect of electronic conductivity are further investigated, and the EIS results are compared with the new results from the newly-developed method.

REFERENCES

1. Giesbrecht, P. K.; Freund, M. S., Recent advances in bipolar membrane design and applications. *Chem. Mater.* **2020,** *32* (19), 8060-8090.

2. Pärnamäe, R.; Mareev, S.; Nikonenko, V.; Melnikov, S.; Sheldeshov, N.; Zabolotskii, V.; Hamelers, H. V. M.; Tedesco, M., Bipolar membranes: A review on principles, latest developments, and applications. *J. Membr. Sci.* **2021,** *617*, 118538.

3. Fuller, C. S., Some analogies between semiconductors and electrolyte solutions. *Rec. Chem. Prog.* **1956,** *17*, 75-93.

4. Frilette, V. J., Preparation and characterization of bipolar ion exchange membranes. *J. Phys. Chem.* **1956,** *60* (4), 435-439.

5. Lovrecek, B.; Despic, A.; Bockris, J. O. M., Electrolytic junctions with rectifying properties. *J. Phys. Chem.* **1959,** *63* (5), 750-751.

6. Strathmann, H., Electrodialysis, a mature technology with a multitude of new applications. *Desalination* **2010,** *264* (3), 268-288.

7. Ahlfield, J. M.; Liu, L.; Kohl, P. A., PEM/AEM junction design for bipolar membrane fuel cells. *J. Electrochem. Soc.* **2017,** *164* (12), F1165-F1171.

8. Oener, S. Z.; Foster, M. J.; Boettcher, S. W., Accelerating water dissociation in bipolar membranes and for electrocatalysis. *Science* **2020,** *369* (6507), 1099-1103.

9. Oener, S. Z.; Twight, L. P.; Lindquist, G. A.; Boettcher, S. W., Thin cation-exchange layers enable high-current-density bipolar membrane electrolyzers via improved water transport. *ACS Energy Lett.* **2021,** *6* (1), 1-8.

10. Yan, Z.; Wycisk, R. J.; Metlay, A. S.; Xiao, L.; Yoon, Y.; Pintauro, P. N.; Mallouk, T. E., High-voltage aqueous redox flow batteries enabled by catalyzed water dissociation and acid–

base neutralization in bipolar membranes. *ACS Cent. Sci.* **2021,** *7* (6), 1028-1035.

11. Schulte, L.; White, W.; Renna, L. A.; Ardo, S., Turning water into a protonic diode and solar cell via doping and dye sensitization. *Joule* **2021**.

12. Kibsgaard, J.; Chorkendorff, I., Considerations for the scaling-up of water splitting catalysts. *Nat. Energy* **2019,** *4* (6), 430-433.

13. Li, Y. C.; Zhou, D.; Yan, Z.; Gonçalves, R. H.; Salvatore, D. A.; Berlinguette, C. P.; Mallouk, T. E., Electrolysis of CO_2 to syngas in bipolar membrane-based electrochemical cells. *ACS Energy Lett.* **2016,** *1* (6), 1149-1153.

14. Salvatore, D. A.; Weekes, D. M.; He, J.; Dettelbach, K. E.; Li, Y. C.; Mallouk, T. E.; Berlinguette, C. P., Electrolysis of gaseous CO_2 to CO in a flow cell with a bipolar membrane. *ACS Energy Lett.* **2018,** *3* (1), 149-154.

15. Li, Y. C.; Yan, Z.; Hitt, J.; Wycisk, R.; Pintauro, P. N.; Mallouk, T. E., Bipolar membranes inhibit product crossover in CO_2 electrolysis cells. *Adv. Sustain. Syst.* **2018,** *2* (4), 1700187.

16. Li, Y. C.; Lee, G.; Yuan, T.; Wang, Y.; Nam, D.-H.; Wang, Z.; García de Arquer, F. P.; Lum, Y.; Dinh, C.-T.; Voznyy, O.; Sargent, E. H., CO_2 electroreduction from carbonate electrolyte. *ACS Energy Lett.* **2019,** *4* (6), 1427-1431.

17. Balster, J.; Srinkantharajah, S.; Sumbharaju, R.; Pünt, I.; Lammertink, R. G. H.; Stamatialis, D. F.; Wessling, M., Tailoring the interface layer of the bipolar membrane. *J. Membr. Sci.* **2010,** *365* (1-2), 389-398.

18. Abdu, S.; Sricharoen, K.; Wong, J. E.; Muljadi, E. S.; Melin, T.; Wessling, M., Catalytic Polyelectrolyte Multilayers at the Bipolar Membrane Interface. *ACS Appl. Mater. Interfaces* **2013,** *5* (21), 10445-10455.

19. Yan, Z.; Zhu, L.; Li, Y. C.; Wycisk, R. J.; Pintauro, P. N.; Hickner, M. A.; Mallouk, T. E., The balance of electric field and interfacial catalysis in promoting water dissociation in bipolar membranes. *Energy Environ. Sci.* **2018,** *11* (8), 2235-2245.

20. Chen, Y.; Martínez, R. J.; Gervasio, D.; Baygents, J. C.; Farrell, J., Water splitting promoted by electronically conducting interlayer material in bipolar membranes. *J. Appl. Electrochem.* **2020,** *50* (1), 33-40.

21. Chen, Y.; Wrubel, J. A.; Klein, W. E.; Kabir, S.; Smith, W. A.; Neyerlin, K. C.; Deutsch, T. G., High-performance bipolar membrane development for improved water dissociation. *ACS Appl. Polym. Mater.* **2020,** *2* (11), 4559-4569.

22. Yan, Z.; Hitt, J. L.; Zeng, Z.; Hickner, M. A.; Mallouk, T. E., Improving the efficiency of CO_2 electrolysis by using a bipolar membrane with a weak-acid cation exchange layer. *Nat. Chem.* **2021,** *13* (1), 33-40.

23. Onsager, L., Deviations from ohm's law in weak electrolytes. *J. Chem. Phys.* **1934,** *2*

(9), 599-615.

24. Kunst, B.; Lovreček, B., Electrochemical properties of the ion-exchange membranes junction. II. *Croat. Chem. Acta* **1962,** *34* (4), 219-229.

25. Simons, R.; Khanarian, G., Water dissociation in bipolar membranes: Experiments and theory. *J. Membrane Biol.* **1978,** *38* (1), 11-30.

26. Simons, R., Strong electric field effects on proton transfer between membrane-bound amines and water. *Nature* **1979,** *280* (5725), 824-826.

27. Strathmann, H.; Krol, J. J.; Rapp, H. J.; Eigenberger, G., Limiting current density and water dissociation in bipolar membranes. *J. Membr. Sci.* **1997,** *125* (1), 123-142.

28. Kovtyukhova, N. I.; Ollivier, P. J.; Martin, B. R.; Mallouk, T. E.; Chizhik, S. A.; Buzaneva, E. V.; Gorchinskiy, A. D., Layer-by-layer assembly of ultrathin composite films from micron-sized graphite oxide sheets and polycations. *Chem. Mater.* **1999,** *11* (3), 771-778.

29. Mareev, S. A.; Evdochenko, E.; Wessling, M.; Kozaderova, O. A.; Niftaliev, S. I.; Pismenskaya, N. D.; Nikonenko, V. V., A comprehensive mathematical model of water splitting in bipolar membranes: Impact of the spatial distribution of fixed charges and catalyst at bipolar junction. *J. Membr. Sci.* **2020,** *603*, 118010.

30. Wrubel, J. A.; Chen, Y.; Ma, Z.; Deutsch, T. G., Modeling water electrolysis in bipolar membranes. *J. Electrochem. Soc.* **2020,** *167* (11), 114502.

31. Bui, J. C.; Digdaya, I.; Xiang, C.; Bell, A. T.; Weber, A. Z., Understanding multi-ion transport mechanisms in bipolar membranes. *ACS Appl. Mater. Interfaces* **2020,** *12* (47), 52509-52526.

32. Xu, Q.; Oener, S. Z.; Lindquist, G.; Jiang, H.; Li, C.; Boettcher, S. W., Integrated reference electrodes in anion-exchange-membrane electrolyzers: Impact of stainless-steel gas-diffusion layers and internal mechanical pressure. *ACS Energy Lett.* **2021,** *6* (2), 305-312.

33. ASTOM > Bipolar Membrane Electrodialyzer [ACILYZER BPED products]. http://www.astom-corp.jp/en/product/05.html.

34. Shen, C.; Wycisk, R.; Pintauro, P. N., High performance electrospun bipolar membrane with a 3D junction. *Energy Environ. Sci.* **2017,** *10* (6), 1435-1442.

35. Wang, J.; Zhao, Y.; Setzler, B. P.; Rojas-Carbonell, S.; Ben Yehuda, C.; Amel, A.; Page, M.; Wang, L.; Hu, K.; Shi, L.; Gottesfeld, S.; Xu, B.; Yan, Y., Poly(aryl piperidinium) membranes and ionomers for hydroxide exchange membrane fuel cells. *Nat. Energy* **2019,** *4* (5), 392-398.

36. Cooper, K., Characterizing through-plane and in-plane ionic conductivity of polymer electrolyte membranes. *ECS Trans.* **2019,** *41* (1), 1371-1380.

37. Lindquist, G. A.; Oener, S. Z.; Krivina, R.; Motz, A. R.; Keane, A.; Capuano, C.; Ayers, K. E.; Boettcher, S. W., Performance and durability of pure-water-fed anion exchange

membrane electrolyzers using baseline materials and operation. *ACS Appl. Mater. Interfaces* **2021,** *13* (44), 51917-51924.

38. Murbach, M. D.; Gerwe, B.; Dawson-Elli, N.; Tsui, L.-k., Impedance.py: A python package for electrochemical impedance analysis. *J. Open Source Softw.* **2020,** *5* (52), 2349.

39. Thommes, M., Physical adsorption characterization of nanoporous materials. *Chem. Ing. Tech.* **2010,** *82* (7), 1059-1073.

40. Eigen, M.; Maeyer, L. d., Untersuchungen über die kinetik der neutralisation. I. *Z. Elektrochem.* **1955,** *59*, 986.

41. *CRC handbook of chemistry and physics: A ready-reference book of chemical and physical data*. 97th ed.; CRC Press Boca Raton: 2017.

CHAPTER III

KINETICS AND MECHANISM OF HETEROGENEOUS VOLTAGE-DRIVEN WATER-DISSOCIATION CATALYSIS

Published as **Chen, L.**; Xu, Q.; Boettcher, S. W. Kinetics and mechanism of heterogeneous voltage-driven water-dissociation catalysis. *Joule* **2023**, *7* (8), 1867-1886. S.W.B. conceived the experiments and led the project. L.C. performed most experiments. Q.X. and L.C. performed pilot experiments. L.C. and S.W.B. wrote the manuscript with input from all authors.

INTRODUCTION

When water is consumed as a reactant in chemical and (electro)catalytic processes, water dissociation (WD, $H_2O \quad H^+ + OH^-$), is often a critical elementary step. In a bipolar membrane (BPM), for example, water is dissociated at the junction between an ionomer anion-exchange layer (AEL) and a cation-exchange layer (CEL), usually accelerated by a catalyst sandwiched between the two and driven by an applied voltage (Figure 3.1A).[1-5] This catalyzed, voltage-driven WD process is not understood, even though BPMs are used in electrodialysis to produce acid/base from brine and to desalinate water,[6-9] in food processing to adjust pH,[10] and in a variety of recycling and separations processes.[11] BPMs can also couple different-pH microenvironments leading to novel uses in fuel cells,[12-13] flow batteries,[14] and water[15-16] and CO_2 electrolyzers[17-18] that can be impurity-tolerant,[19] and enable the use of efficient and abundant electrocatalysts. Elementary reaction steps similar to WD are also likely key in electrocatalytic reactions including

hydrogen evolution and CO_2 reduction that require protons in neutral-to-basic media where water is the only available proton donor. These analogous proton-transfer processes may also be voltage-driven in the electrochemical double layer and accelerated via surface reactions.[15, 20-22]

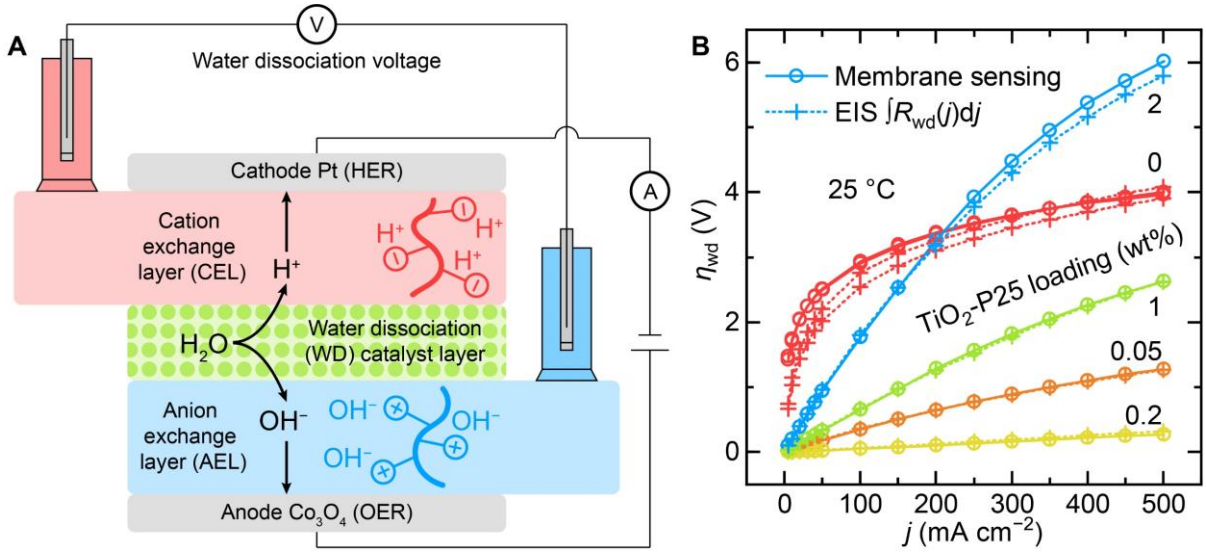

Figure 3.1 Schematic of membrane-potential sensing in a bipolar-membrane (BPM) electrolyzer and comparison between the electrochemical-impedance-spectroscopy (EIS) and membrane-potential-sensing methods of determining η_{wd}

(A) In the AEL, positive functional groups (e.g. quaternary ammonium cations) are fixed to the polymer backbone while small anions like OH^- are mobile. In the CEL, negative groups (e.g. sulfonate) are fixed to the polymer backbone and small cations like H^+ are mobile. Pure water is fed to cathode and anode gas-diffusion electrodes and diffuses into the BPM. WD occurs at the junction of the AEL and CEL. The voltage between the two reference electrodes connected to the AEL and CEL by membrane strips are recorded as a function of applied current. By subtracting the values at open circuit, the WD overpotential η_{wd} is calculated. **(B)** The impedance spectra from the entire cell were measured at different current densities j. The WD resistances R_{wd} were extracted by fitting the spectra and η_{wd} was calculated by integrating R_{wd} as a function of j. Loading is represented by the spin-coat ink concentration; 0.2 wt% yields ~10 μg cm^{-2} or ~200-nm-thick nanoparticle films.

The efficiency of WD is central to the performance of BPMs. We recently showed that metal-oxide nanoparticles dramatically accelerate the WD reaction both in BPMs and as a step

in electrocatalysis,[15] and that the ability of the WD catalyst to screen and focus the interfacial electric field in the BPM junction is important.[23] Previously either an electric-field effect (the so-called second Wien effect),[24-27] a catalytic effect,[15, 28-29] or a combination of two[23, 30-31] has been invoked to explain WD kinetics in the BPM orders-of-magnitude faster than the equilibrium rates in bulk water, but how the field and catalysis interact at the microscopic/mechanistic level is largely unknown.

These previous studies are also limited in how they assess the WD voltage, usually in H-cells or multi-compartment cells with supporting electrolytes that contain salt ions (other than H^+ and OH^-) such as Na^+ and Cl^-. The current carried by salt ions complicates the analysis of the polarization curves and the study of WD with unknown contributions from series resistance. Temperature-dependent kinetics are central to understand mechanisms and extract activation energies (E_a), but these are rarely done for BPMs due to the experimental difficulties in isolating the WD overpotential (i.e. the thermodynamic driving force for WD)[15] from other temperature-dependent processes. The few previous studies have found widely ranging apparent activation energies from ~10-80 kJ mol^{-1}, primarily measured for commercial BPMs where the interface chemistry and structure where WD occurs are unknown.[28, 32-35] The WD rate constant also depends on the pre-exponential factor (or frequency factor) A, which is seldom discussed in the above, as is unfortunately typical in electrochemistry, despite its importance.[36-39]

We previously avoided these complications by using BPMs in a pure-water electrolyzer, without salt ions, where H^+ and OH^- are the only ionic charge carriers.[15, 40] We also demonstrated that the (areal) WD resistance R_{wd} can be isolated from the total impedance (that includes

electrode reaction and transport) via electrochemical impedance spectroscopy (EIS).[23] The WD overpotential/overvoltage η_{wd} is calculated from R_{wd} by

$$\eta_{wd} = \int_0^j R_{wd}(j)\mathrm{d}j \tag{3.1}$$

where j is the current density. R_{wd} is a differential resistance that is a function of j (or equivalently, η_{wd}, the driving force for WD). R_{wd} decreases with driving force and thus j. When R_{wd} does not depend on j, Equation 3.1 reduces to Ohm's law. Estimating η_{wd} in this way requires measuring EIS at different j, which is slow due to the need for low-frequency data. Some BPMs also degrade during prolonged testing, making it difficult to separate temperature-dependent kinetics from other processes because degradation will underestimate E_a in a temperature-step-up experiment but overestimate E_a in a temperature-step-down experiment. In Nyquist plots, the WD semicircle is sometimes not well-separated and low-frequency inductive loops can appear, complicating the analysis and introducing error.

Here we report a "membrane-potential sensing" method to directly measure η_{wd} in BPM electrolyzers as a function of temperature and current and use it to discover new underlying physical processes controlling WD rates. We used a simpler setup in anion-exchange-membrane electrolyzers to separate the anode and cathode voltage with one reference electrode,[41] as also reported earlier for fuel cells.[42-44] An AEL and a CEL membrane-sensing strip are connected to the AEL and CEL of the BPM, respectively (Figure 3.1A), with separate reference electrodes attached to each strip. After subtracting the open-circuit values, η_{wd} is the voltage between the two references (the ohmic drop across AEL and CEL is small and can be ignored, see more discussion in the Experimental Procedures). We demonstrate that η_{wd} measured by membrane-

potential sensing is almost identical to that from EIS, corroborating both approaches. We use the method to study temperature-dependent WD kinetics on model TiO_2-P25 catalyst. We discover that uncatalyzed BPMs show decreasing E_a with driving force, as expected from typical electrode-kinetics models such as the Butler-Volmer model. In contrast, WD in catalyzed BPMs has an apparent E_a that is almost independent of η_{wd}, but a pre-exponential factor A that surprisingly increases linearly with η_{wd}. We develop a semi-empirical "BPM equation" to quantitatively describe the temperature-dependent kinetics based on the equilibrium activation energy $E_{a,0}$, the effective proton-transfer coefficient α (to describe the effect of η_{wd} on the activation barrier), and a pre-exponential factor A that depends linearly on η_{wd}. Kinetic-isotope experiments show that BPMs fed D_2O have higher η_{wd} than H_2O, with similar E_a and different A. Adding electronically conducting acetylene carbon black (ACB) to a thick layer of TiO_2-P25 both lowers E_a and increases the sensitivity of E_a on η_{wd}, supporting the hypothesis that the electric field is concentrated by conductors to increase WD kinetics. With this data, we then elaborate a new mechanism of field/voltage-driven WD catalysis that includes field-dependent organization of surface water that facilitates proton transfer between near-surface water and the (polarized) metal-oxide WD catalyst, and proton transport across the nanoparticle catalyst surface.

RESULTS AND DISCUSSION

Comparison between membrane-potential-sensing and EIS methods

Previously we showed that EIS can be used to isolate the WD resistance R_{wd} from the total-cell impedance (Figure B.1).[23] In a Nyquist plot, the high-frequency semicircle is related to WD while the low-frequency semicircles are related to anode and cathode charge-transfer

resistances and capacitances. Equivalent-circuit fits are used to extract R_{wd} for each different j. Integrating R_{wd} as a function of j, we calculate $\eta_{wd} = \int_0^j R_{wd}(j)\mathrm{d}j$. To corroborate the membrane-potential-sensing and EIS methods, we compare the two ways to calculate η_{wd} for the same sample (Figure 3.1B). The methods produce similar $\eta_{wd} - j$ curves, regardless of WD catalyst loadings. Because the EIS measurement is slow, making degradation effects more serious and complicating the temperature-dependence measurement, we use the data from membrane-potential sensing in the analysis below.

Temperature dependence and Arrhenius analysis

The WD polarization curves with different TiO_2-P25 loadings from 25–55 °C are shown in Figure 3.2 and Figure B.2. We chose TiO_2-P25 as the model catalyst due to its abundance, low cost, and good performance as a single-composition catalyst in BPM electrolyzers. The optimal loading is 0.2 wt% (represented by the spin-coat ink concentration; equivalent to ~10 μg cm^{-2} and ~200 nm in thickness).[23] Seven loadings were tested and, as expected, when the WD catalyst loading decreases, the polarization curves converge to the pristine BPM without WD catalyst (Figure B.3). In pristine BPMs without WD catalyst, j increases exponentially with η_{wd}, like a typical electrochemical reaction with Tafel-like behavior (or Marcus / Butler-Volmer behavior, which are fundamentally related). In contrast, BPMs with optimal loading of TiO_2-P25 show a linear dependence of j on η_{wd}, more like a resistor that follows Ohm's law. Polarization curves of BPMs with other loadings lie between these two cases, i.e., with a (nearly) linear shape when η_{wd} is small and more exponential when η_{wd} is large. The linear relationship is analogous to the limiting case of the Butler-Volmer model when the exchange current density j_0 is large, or in

other words, the electrode charge-transfer kinetics is fast and only a small overpotential η is needed to drive a large current density (see discussion below).

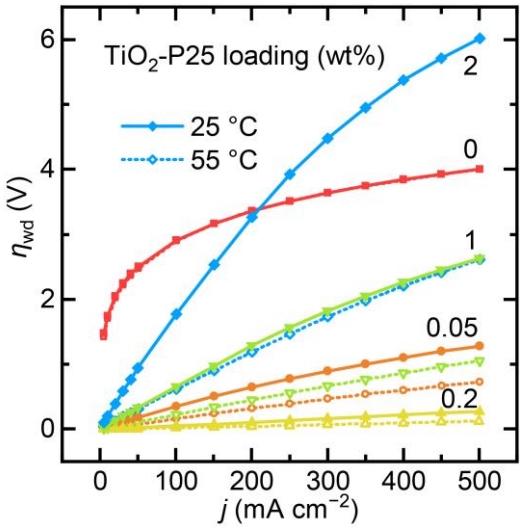

Figure 3.2 Temperature-dependent polarization curves of BPMs with different mass loadings of TiO_2-P25 WD catalyst

Notice the transition from exponential, to linear, and then to combination of linear and exponential $j - \eta_{wd}$ response with increasing loading. Temperatures tested were 25, 35, 45, and 55 ± 2 °C, but only data at 25 and 55 °C are shown here for clarity. The uncatalyzed BPM (labelled 0) has almost no apparent temperature dependence at the high current densities tested here due to concomitant degradation processes. See also Figure B.2.

Increasing the temperature lowers η_{wd} in most cases, except for the BPM without catalyst. This artifact was because the pristine uncatalyzed BPM performance degrades during testing, obscuring the temperature dependence. The reason that pristine, uncatalyzed BPMs degrade so fast is yet unclear, but could be due to chemical degradation of the fixed-charge groups on the ionomer at the sharp BPM interface in the presence of the strong electrochemical potential gradient over the abrupt interface under bias, or due to current-driven ionomer intermixing. Further studies that combine various spectroscopy techniques are needed to elucidate these

mechanisms of uncatalyzed BPM degradation (the optimized catalyzed BPMs have stable WD performance). Therefore, for pristine BPM data reported below, we use only low current densities and a small correction for the calibrated degradation rate (Figure B.4). To analyze the data from BPMs with and without WD catalysts, we use an Arrhenius-type model

$$j = Ae^{-\frac{E_a}{RT}} \tag{3.2}$$

where A is the pre-exponential factor, E_a is the apparent activation energy, R is the gas constant, and T is the temperature. Notice A has the same unit as j (mA cm^{-2}). Since the concentration of the reactant, i.e., water, is unknown inside the BPM junction, we did not normalize A to unit concentration.[36] We assume the concentration of water is largely constant as we apply ≤ 500 mA cm^{-2}, significantly above which water transport into the BPM can be limiting.[40] This assumption is justified because the differential resistance of the polarization curves usually increases when the water transport is limited, as observed at >700 mA cm^{-2} for similar systems previously.[40] Here, the differential resistance decreases or remains constant as j increases (Figure 3.2).

Our aim is to analyze E_a and A at a fixed η_{wd} (but not j) because η_{wd} represents the driving force while j represents the WD reaction rate. There are no salt ions to otherwise carry current so all measured current must be associated with WD. Because we collect data under current control, the $j - \eta_{wd}$ data are interpolated with cubic splines (Figure 3.3A) to generate the Arrhenius plots ($\ln j$ plotted against $1/T$) at constant driving force (η_{wd}). We choose cubic splines to capture the curvature of the polarization curves.

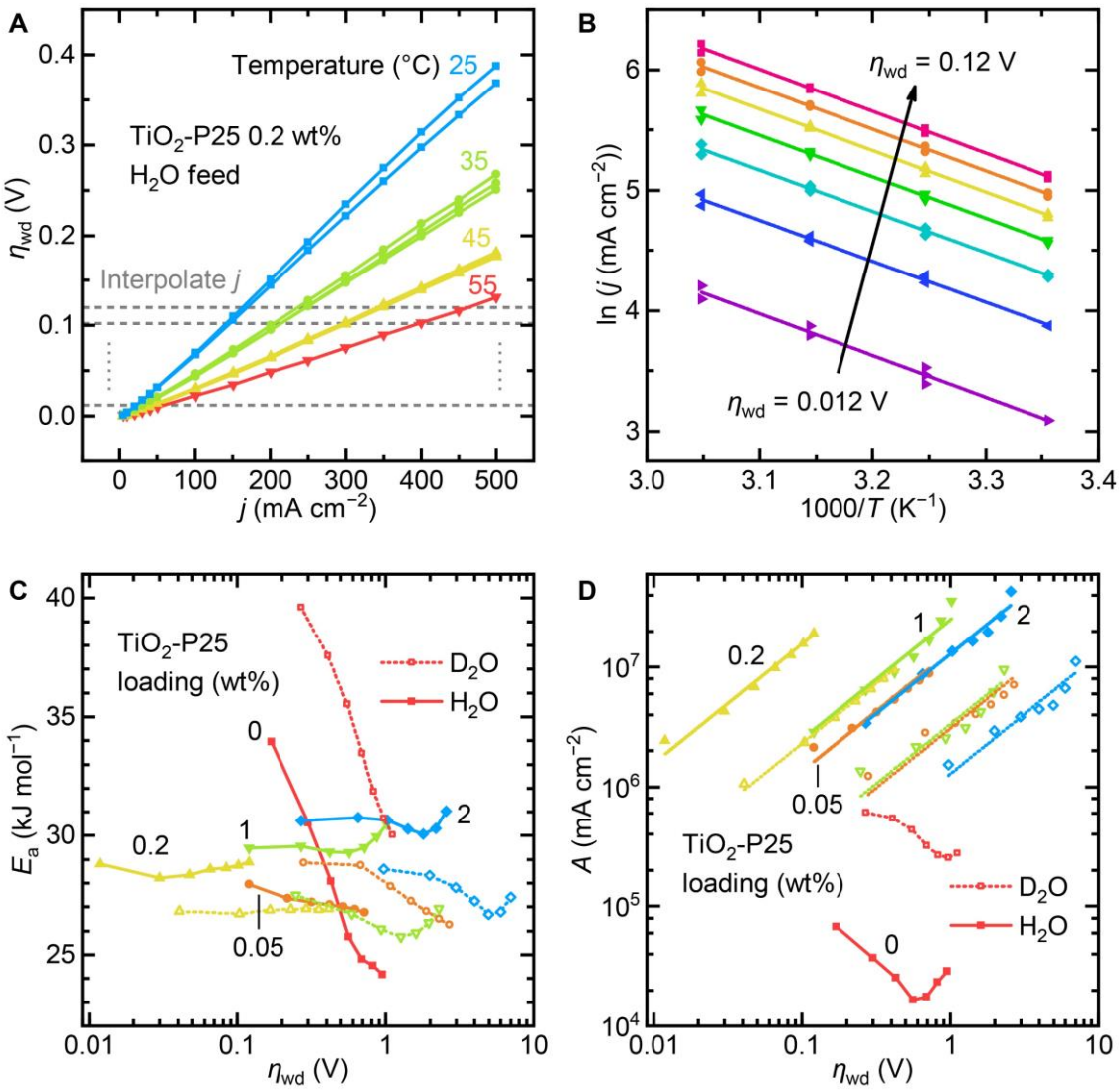

Figure 3.3 Arrhenius analysis of temperature-dependent BPM polarization curves

(A) Temperature-dependent polarization curves of a BPM with 0.2 wt% TiO_2-P25 and fed by H_2O. The same sample is cycled between 25 and 55 °C. Current density j is interpolated at certain η_{wd}. **(B)** Arrhenius plots of a BPM with 0.2 wt% TiO_2-P25 and fed by H_2O at different η_{wd}'s. Lines are least-squares linear fits of the experimental data. **(C)** Apparent activation energy E_a as a function of η_{wd}. Different loadings of TiO_2-P25 are used as WD catalyst. The electrolyzer is fed by either H_2O or D_2O. Notice the log scale on the horizontal axis. **(D)** The pre-exponential factor A as a function of η_{wd}. Notice the log scale on both axes. Lines are least-squares linear fits with fixed slope of one except the loading of 0. Voltage increases the pre-exponential factor for catalyzed samples instead of lowering the activation barrier.

For a fixed η_{wd}, the Arrhenius-plot slope and vertical intercept from linear fitting yields

E_a and A, respectively. The procedure is repeated for different η_{wd} (Figure 3.3B) to understand how the driving force for WD modulates kinetics and possible mechanisms. The slope does not change with $1/T$ (within the temperature range of the experiment); E_a and A are thus independent of T. In the next section we discuss how E_a and A depend on η_{wd} and WD-catalyst loading, as this informs the microscopic picture of catalyzed WD reactions in BPMs, and more broadly in electrocatalysis where reactions also take place in the presence of a large interfacial electric field.[21, 45-46]

Overpotential and mass-loading dependence of kinetic parameters

The apparent E_a and A as a function of η_{wd} with different TiO_2-P25 loadings are shown in Figure 3.3C. For the pristine BPM without WD catalyst, E_a decreases from 34 to 24 kJ mol^{-1} as η_{wd} increases from 0.2 to 1 V. This behavior is like those observed for interfacial faradaic processes, where the activation energy for electron transfer (e.g., in the Butler-Volmer or Marcus models) is lowered with increasing absolute overpotential. For BPMs with TiO_2-P25 catalyst, however, E_a is essentially constant with η_{wd}. The similar independence of E_a on transmembrane voltage has also been observed occasionally in other studies of BPMs, as mentioned above.[28, 34]

Differences in WD processes in BPMs compared with WD in pure water are also apparent (Table 3.1). In pure water, Eigen and de Maeyer determined the apparent E_a for WD $E_a(k_D)$ = 64.9–69.0 kJ mol^{-1} while for recombination/neutralization $E_a(k_R)$ = 8–13 kJ mol^{-1}, where k_D and k_R denote the rate constant of WD and H^+/OH^- recombination/neutralization respectively[47-48]. Natzle and Moore found $E_a(k_R)$ = 15 ± 3 kJ mol^{-1}.[49] Since $E_a(k_D)$ and $E_a(k_R)$ are related by the standard enthalpy of WD as $\Delta H° = E_a(k_D) - E_a(k_R)$ = 56 kJ mol^{-1},[50-51] and thus $E_a(k_D)$ = 71 ± 3

kJ mol^{-1}, which is comparable with the results of Eigen and de Maeyer. Interestingly, the E_a for WD in BPMs is lower than $E_a(k_D)$ in pure water by a factor of two, suggesting a different mechanism and/or solvation environment.

Table 3.1 Kinetic and thermodynamic parameters of H_2O and D_2O dissociation

	H_2O	D_2O	H/D
Dissociation rate constant k_D (10^{-5} s^{-1})	2.5 [48]; 2.56 [52]; 2.04 [49]	0.25 [52]; 0.186 [49]	~11
Apparent activation energy $E_a(k_D)$ (kJ mol^{-1})	64.9–69.0 [48]	76* [52]	~0.88
Neutralization rate constant k_R (10^{11} M^{-1} s^{-1})	1.4 [48]; 1.43 [52]; 1.12 [49]	0.84 [52]; 0.741 [49]	~1.7
Apparent activation energy $E_a(k_R)$ (kJ mol^{-1})	8–13 [48]; 15 [49]	15* [52]	~0.85
Dissociation constant K_w (10^{-14})	1.0 [51]	0.11 [51]	~9.1
Standard Gibbs free energy $\Delta G°$ (kJ mol^{-1})	79.87 [51]	85.23 [51]	~0.94
Standard enthalpy $\Delta H°$ (kJ mol^{-1})	55.82 [51]	60.87 [51]	~0.92
Standard entropy $\Delta S°$ (J mol^{-1} K^{-1})	−80.67 [51]	−81.75 [51]	~0.97

* Extracted from Arrhenius analysis using the literature values.

Unexpectedly, we find that the pre-exponential factor A increases almost linearly with η_{wd} for catalyzed BPMs (Figure 3.3D, notice the log–log scale and the unit-slope lines), in contrast with classic Butler-Volmer models where E_a decreases linearly with η, and A is independent of η.[36] The Butler-Volmer model, of course, was developed for *electron*-transfer electrode reactions, while WD is a *proton*-transfer reaction. However, both involve interfacial *charge*-transfer driven by electrochemical potential gradients. We use the Butler-Volmer equation as a well-known model to compare with and discuss a microscopic physical picture below.

The BPM equation

The above Arrhenius analysis (based on interpolation and linear fitting) is limited by the η_{wd} of the highest test temperature (e.g., 0.12 V in Figure 3.3A), as above that there are only data for three temperatures or fewer. We thus developed a semi-empirical equation to fit all the data and minimize the errors due to interpolation. We hypothesize, following the Butler-Volmer model, that

$$E_a = E_{a,0} - \alpha F \eta_{wd} \tag{3.3}$$

where $E_{a,0}$ is the "equilibrium activation energy" and $\alpha \geq 0$ is the "proton-transfer coefficient", a unitless number which describes how E_a for proton transfer changes with η_{wd} and determines the shape of the polarization curve. An α tending to 0 results in a linear $j - \eta_{wd}$ response (e.g., with optimal TiO_2-P25 loading) while a larger α leads to an exponential shape (e.g., as for the pristine BPMs). Because the prefactor A is proportional to η_{wd}, we have

$$A = G_0 \eta_{wd} \tag{3.4}$$

where the new constant $G_0 = A/\eta_{wd}$ has the unit of areal conductance (mS cm^{-2}). Note that the pre-exponential factor A is proportional to η_{wd}, but G_0 itself is independent of η_{wd}. Substituting these relations into the Arrhenius equation yields a semi-empirical "BPM equation" to describe WD in BPMs (the forward and reverse reaction contributions are not separated explicitly, see more discussion below)

$$j_{wd} = G_0 \eta_{wd} e^{-\frac{E_{a,0} - \alpha F \eta_{wd}}{RT}} = \left(G_0 e^{-\frac{E_{a,0}}{RT}} \right) \eta_{wd} e^{\frac{\alpha F \eta_{wd}}{RT}} \tag{3.5}$$

where G_0, $E_{a,0}$ and α depend on catalyst type and loading. By fitting j as a function of η_{wd} at different T, we extract the parameters G_0, $E_{a,0}$ and α using the entire data set (Figure 3.4). For

most polarization curves, the fitting provides $R^2 > 0.99$ and the parameter-fitting errors are usually less than 10% of the parameter values (Figure B.2). The fit requires variable-temperature polarization curves, since at a fixed T, and with fixed catalyst and loading, G_0 and $E_{a,0}$ are interdependent and lumped into the term as $G_0 e^{-\frac{E_{a,0}}{RT}}$. At small η_{wd}, $e^{\frac{\alpha F \eta_{wd}}{RT}} \rightarrow 1$ and the linearized BPM equation is

$$j_{wd} = \left(G_0 e^{-\frac{E_{a,0}}{RT}}\right)\eta_{wd} \tag{3.6}$$

The classical linearized Butler-Volmer equation at small overpotential η provides

$$j_{BV} = \left(\frac{j_{0,BV}F}{RT}\right)\eta \tag{3.7}$$

In analogy with Equation 3.6, we can define a WD exchange current density j_0

$$j_{0,wd} = \frac{RT}{F} G_0 e^{-\frac{E_{a,0}}{RT}} \tag{3.8}$$

Higher G_0 and lower $E_{a,0}$ give a larger j_0, and j_0 increases with temperature. The parameter G_0 can be called the driving-force-independent "proton-transfer conductance" and is likely related to the number of active proton acceptor/donor sites on the WD catalyst surface and the frequency by which water molecules interact with those sites to accommodate proton transfer (see below).

The parameters G_0, $E_{a,0}$ and α depend on TiO_2-P25 loading. $E_{a,0}$ increases from ~25 to ~30 kJ mol^{-1} for the BPM without catalyst to one with optimal loading (0.2 wt%, ~10 μg cm^{-2} and ~200 nm) then increases slowly and approaches $E_{a,0}$ ~32 kJ mol^{-1} when the loading is higher than 1 wt% (Figure 3.4A). The shape of the polarization curve is related to α (compare Figure 3.2 and Figure 3.4A). A smaller α results in a linear $j - \eta_{wd}$ response, as in the case for optimal loading ($\alpha = 0$), while a larger α yields a more-exponential dependence, as in the very low

loadings and without catalyst. Interestingly, G_0 increases substantially with TiO_2-P25 loading before the optimal value (notice the log scale), and then slightly decreases. Lower $E_{a,0}$, higher α, and higher G_0 lead to a better performance. In the case of TiO_2-P25, G_0 appears to be the dominant factor and is correlated with η_{wd} (Figure 3.4A, top and bottom panels).

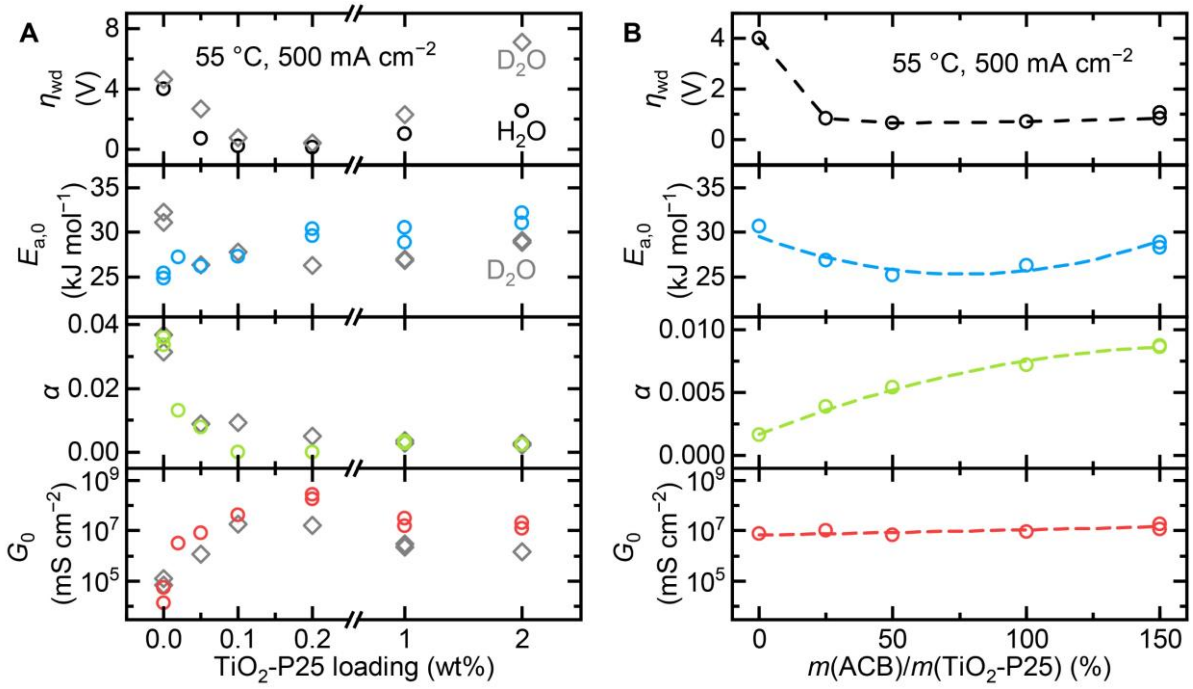

Figure 3.4 Temperature-dependence analysis using the semi-empirical BPM equation

$j_{wd} = G_0 \eta_{wd} e^{-\frac{E_{a,0} - \alpha F \eta_{wd}}{RT}}$, where $E_{a,0}$ is the "equilibrium activation energy", α is the "proton-transfer coefficient", and G_0 is the "proton-transfer conductance". To compare with BPM performance, η_{wd} at 55 °C and 500 mA cm^{-2} is also included. Notice the log scale on the vertical axis for G_0. **(A)** Different loadings of TiO_2-P25 are used as WD catalyst. The electrolyzer is fed by either H_2O or D_2O. Notice the log scale on the horizontal axis. **(B)** Different mass ratios of acetylene carbon black (ACB) and TiO_2-P25 are used as WD catalyst. The mass of TiO_2-P25 is kept constant while the mass of ACB is varied. The electrolyzer is fed by H_2O. The increase of the proton-transfer coefficient α with conductive additive is consistent with electric-field screening and focusing. Lines serve as a guide for the eye.

Kinetic isotope effects

To obtain information on the rate-limiting step in WD, we fed the BPM electrolyzer with D_2O and measured kinetic-isotopic effects (Figure B.5). For the catalyzed BPMs, η_{wd} in D_2O is ~2 to 4 larger than in H_2O (Figure 3.4A, top panel) despite both $E_{a,0}$ and α being relatively similar. The larger η_{wd} in D_2O is largely due to a lower G_0 (and thus A), which is evident in Figure 3.3D. For pristine BPMs, D_2O has a higher E_a than H_2O, while catalyzed BPMs have E_a similar or smaller for D_2O compared to H_2O (Figure 3.3C). In the pristine BPMs, WD likely occurs more like in bulk water, i.e., proton transfer between water molecules under the strong electric field. The H/D ratio of E_a is ~0.8, comparable to the $E_a(k_D)$ for bulk water ~0.88 (Table 3.1). For catalyzed BPMs,WD occurs on the catalyst surface, and the D_2O-related species might have a lower binding energy to the catalyst surface compared to H_2O, similar to the inverse kinetic isotope effect in the oxygen-reduction reaction.[53] These isotope effects can be compared with those found for diffusion coefficients and associated activation energies for H_2O, D_2O, and their ions (Table 3.2). Diffusion of these species follows an Arrhenius model with an activation energy of $E_a(D)$. Although the diffusion coefficients show H/D ratios (defined as the value of H species relative to D species, such as H_2O/D_2O, H^+/D^+, and OH^-/OD^-) ranging from 1.2 to 1.7, the H/D ratios of $E_a(D)$ are close to unity. Bulk H_2O and D_2O also show different in dissociation kinetics (Table 3.1). Compared to D_2O, the dissociation equilibrium constant K_w and dissociation rate constant k_D of H_2O is 9 and 11 times larger, respectively, while both $E_a(k_D)$ are similar. These data are consistent with our experimental results of H_2O and D_2O in voltage-driven catalyzed WD reaction in the BPM; the rates/current densities are substantially slower for D_2O

(characterized by A or G_0), but the temperature dependence (characterized by E_a) are similar. These data point to the pre-exponential factor A being associated not only with the number of catalyst proton acceptor/donor sites on the surface, but also with the facility by which water molecules can organize via molecular motion for the charge-transfer step, as discussed below.

Table 3.2 Diffusion coefficients and associated activation energies for H_2O, D_2O and their ions

	H_2O	D_2O	H/D
Diffusion coefficient D (10^{-5} cm^2 s^{-1})	2.299 [54]	1.872 [54]	~1.2
Apparent activation energy $E_a(D)$ (kJ mol^{-1})	18–20 [54]	19–21 [54]	~0.95
	H^+	D^+	H/D
Diffusion coefficient D (10^{-5} cm^2 s^{-1})	9.311 [55]	6.655 [55]	~1.4
Apparent activation energy $E_a(D)$ (kJ mol^{-1})	10.6 [56]; 10.0* [57]	10.0* [57]	~1
	OH^-	OD^-	H/D
Diffusion coefficient D (10^{-5} cm^2 s^{-1})	5.273 [55]	3.169 [55]	~1.7
Apparent activation energy $E_a(D)$ (kJ mol^{-1})	13 [56]; 12.6* [57]	13.0* [57]	~1

*Activation energy of ionic conductivity is used due to the lack of data.

Effect of electronic conductivity

We previously showed that adding electronic conductors such as acetylene carbon black (ACB) nanoparticles to a thick layer (~120 μg cm^{-2} and ~2.4 μm) of TiO_2-P25 WD catalyst improves the BPM performance substantially, likely through focusing the electric at the AEL|catalyst and catalyst|CEL interfaces.[23] We measured the temperature dependence of these thick TiO_2-P25 WD layers mixed with different ratios of ACB (by mass) as WD catalyst. Adding

ACB lowered η_{wd} (the optimal ratio is between 50% and 100%) consistent with previous results[23] (Figure 3.4B). Analysis of the new temperature-dependent data shows that adding ACB lowers $E_{a,0}$ from ~30 to ~26 kJ mol^{-1} when the mass ratio increases from 0 to 50%, and increases α by a factor of ~5 (from ~0.002 to ~0.09) when the mass ratio increases from 0 to 150%, but does not change G_0 significantly. Simpler Arrhenius analysis also shows that E_a is lowered (Figure B.6), consistent with the BPM-equation analysis. Adding electronically conductive material to the region of WD thus appears to improve kinetics for thick catalyst layers by screening and increasing local-electric-field strength that serves to lower E_a with increasing applied voltage.

A new microscopic model for voltage-driven catalyzed WD

The sum of the kinetic data and analysis lead us to propose a new tentative model for WD on metal-oxide surfaces (Figure 3.5). This new model is relevant not only for BPMs but also for interfacial electrocatalytic processes where WD is required to provide protons, e.g., CO_2 or H_2O reduction in neutral to basic conditions.[17] Acid-base reactions, H^+ and OH^- transfer, and WD, all involve the interconversion between O–H and hydrogen bonds. The Grotthuss mechanism of H^+ and OH^- transport in water involves the movement of charge through a series of protonation and deprotonation steps on different water molecules (i.e., the interconversion between O–H bonds and hydrogen bonds and non-vehicular transport). Similar mechanisms could occur on the surface of oxide nanoparticles due to species such as bridging and terminal oxo and hydroxyl groups that can be protonated or deprotonated and that interact strongly with interfacial water that may mediate proton transport.[58-59] The surface of metal oxides thus may serve as a "sink" or "source" of protons which can transport on the nanoparticle surface through the surface

oxo/hydroxyl groups. *The oxide surface can thus serve as both proton reservoir and proton conductor.*

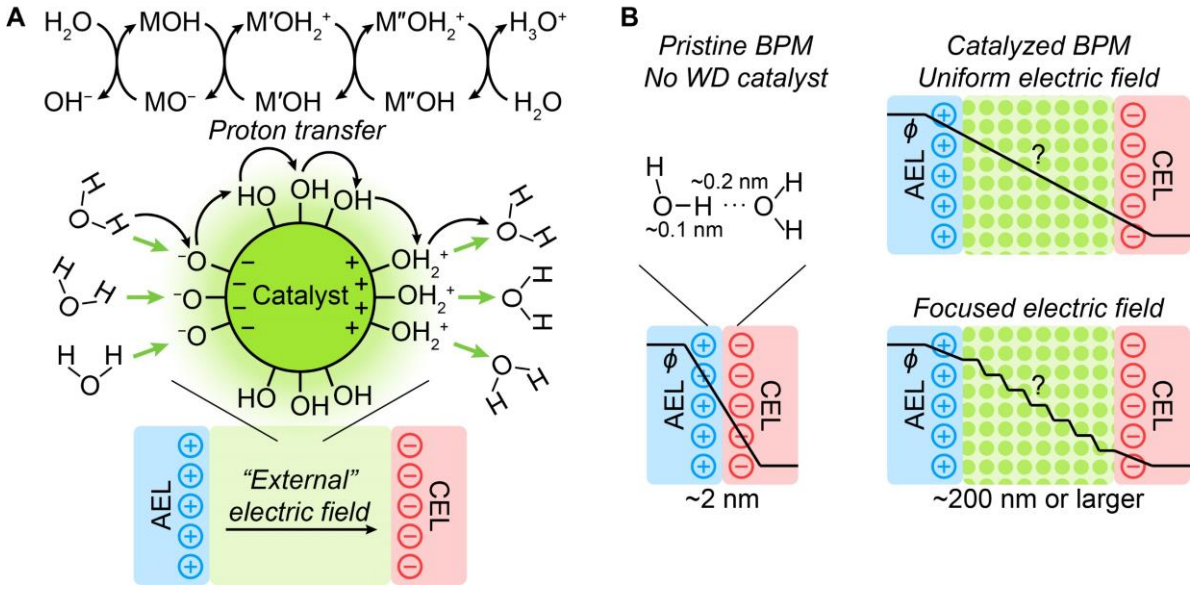

Figure 3.5 Proposed mechanism for voltage-driven catalyzed WD

(A) The "external" electric field originates from the unbalanced fixed charges in the AEL and CEL. The local electric field (shown in green arrows) originates from the protonation and deprotonation of the nanoparticle surface hydroxyls, and further modulated by electronic polarization of free carriers or dielectric inside the nanoparticles, as well as the external electric field. The local electric field induces the water molecules to orient, facilitating WD and proton transfer. M, M′, and M″ denote different sites on the catalyst surface. **(B)** Possible electric-potential ϕ profiles of pristine BPMs and catalyzed BPMs. The hydrogen bond between water molecules is also shown for comparison.

Local equilibrium between the WD catalyst and liquid water further leads to interfacial electrostatic effects in the form of a double-layer electric field whenever the local pH is not at the point of zero charge (PZC) of the nanoparticle. The strength of this local interfacial field is likely important for proton transfer reactions between the surface of the catalyst particle and the water, because the electric field modulates substantially interface-water structure and properties, like

the effective dielectric constant and average orientation.[60-62]

In the BPM junction, however, the situation is further affected by the *external* electric field originating from the uncompensated fixed charges at the AEL and CEL. If the nanoparticle has high electronic conductivity (e.g., IrO_x, $Sb:SnO_2$, etc.), the electrons inside the nanoparticle will redistribute to screen the electric field and the nanoparticle will be polarized, much like a nanoscale bipolar electrode.[63] These conductive catalysts could even drive faradaic reactions (such as electrolysis) if sufficiently polarized, but for our catalysts the applied WD overpotential is typically too low for such reactions to occur. WD catalysts with a high dielectric constant (e.g., TiO_2), will similarly screen the electric field inside the particle and increase the electric field outside the particle within the effective Debye length defined by the local ion concentrations and dielectric constant at the particle surface.[64]

In both high-dielectric and conductive particles, the polarization of the particle by the external electric field across the BPM should enhance the local electric field near the nanoparticle surface, driving water molecules to orient and align, on average, their dipole moment with electric field.[62, 65] Under reverse-bias operation, i.e., where the BPM is driving WD at the junction, the space-charge regions in the AEL and CEL increase with applied bias leading to an increasing average electric-field strength across the WD catalyst layer and increasing the degree of water orientation.

We propose that the water organization at the WD catalyst/water interface, driven by the external electric field, is responsible for the experimentally measured pre-exponential factor, i.e., representing a process that describes the fraction of time, and frequency at which, the system is

poised for proton transfer. Our model explains the proportionality between A and η_{wd}. As the local electric field increases with η_{wd}, water molecules are, on average, better oriented for donating a proton to one side of the WD catalyst particle (i.e., partial-positive proton on H_2O pointed toward the surface) and accepting a proton on the other side of the WD catalyst (i.e., with the partial-negative O on H_2O pointed toward the surface), as depicted in Figure 3.5A. The fact that D_2O has a smaller A than H_2O is consistent with the slower vibrational frequency and molecular motions of heavier D_2O.

While the above argument provides an explanation for how the local electric field, both at equilibrium and increasing with applied reverse bias, might lead to an increase in the pre-exponential factor describing WD kinetics, we must also consider the field effect on the WD activation barrier. In the classic Butler-Volmer model, increasing applied overpotential leads to an increase in electron-transfer rate by lowering activation barrier. The transfer coefficient, typically called α (which can be equated to the symmetry factor β of the free-energy surface for elementary reaction steps),[66] is often taken to be 0.5. This assumption is based on the notion that the electron transfer occurs through the width of the double layer (i.e., it is an outer-sphere process) and that the free-energy surface is symmetric with respect to approach to the transition state. We consider the overall reaction in our analysis, and define α here the proton-transfer coefficient (instead of symmetry factor).

While we use a similar formulation to describe the rate of proton transfer in WD, the experimental values for the proton-transfer coefficient α are much smaller, i.e., from 0 to ~0.04, resulting in a weak E_a dependence on η_{wd} for catalyzed BPMs, compared with typical

electrochemical reactions. The electric-field dependence of WD rate has historically been interpreted in the context of the second Wien effect where the strong local field increases the dissociation rate of weak electrolytes, although others have questioned whether a sufficiently strong field in fact exists in the BPM junction.[15, 25] Our new experimental data shed light on this fundamental process. Increasing electric field, represented by a larger driving force for WD through η_{wd}, does decrease the experimental activation barrier, supporting the field-effect argument. Yet this effect is only significant for BPMs without catalyst that have a narrow junction thickness and hence high electric field (and thus very poor WD and BPM performance).

In BPMs, the electric potential drop mainly occurs at the junction, thus the *electric potential drop* distance is roughly the junction thickness. For pristine BPM without catalyst, the junction thickness is ~1–5 nm including the depletion region, interface roughness, and intermixing between AEL and CEL (Figure 3.5B).[2, 67-69] For a hydrogen bond in liquid water (O–H···O), the O–H bond length is ~0.1 nm and the H···O bond length is ~0.2 nm.[70] Thus the proton-transfer distance for WD ($2H_2O \rightarrow H_3O^+ + OH^-$) is ~0.1 nm. If we take the junction thickness to be ~2 nm, then the ratio between proton-transfer distance and the overall potential-drop distance is ~0.05, which is comparable to the experimental α of pristine BPMs ~0.04; that is, only about 5% of the potential drop across the entire interface is available, on average, to facilitate any given proton transfer step.

The situation is more complicated when WD catalysts are introduced because the spatial electric-field profile in the junction, especially near the catalyst surface where WD occurs, is unknown. From previous work, the TiO_2-P25 thickness at optimal loading (0.2 wt%) is ~200

nm.[23] Thus the ratio between proton-transfer distance and the overall potential-drop distance is ~0.0004 which is comparable to the experimental $\alpha \sim 0$ of optimal-loading samples. If the electric field were uniform inside the BPM junction, further increasing the WD catalyst loading and thus junction thickness, should decrease α. However, the experimental result for the much thicker 2 wt% is $\alpha \sim 0.002$. By adding ACB, α for similar samples increases to ~0.01. This data suggests that the catalyst screens the electric field inside the nanoparticles, thus focusing the electric field outside the particle where WD takes place. Continuum, molecular-dynamics (MD), and density-functional-theory (DFT) modelling would help test the above hypothesis.

To test the role of interface-layer thickness, and thus resulting electric-field distribution, in the absence of the catalytic metal-oxide particles, we used polystyrene nanospheres (non-functionalized, diameter of 100 nm). BPMs fabricated with about two layers of the beads on the CEL (to make a ~200 nm spacing between AEL and CEL, similar to the optimal TiO_2 WD catalysts) yield extremely poor performance (Figure B.7), much worse than even the pristine BPM. The resulting $j - \eta_{wd}$ curve, however, was much more linear compared with the pristine BPM, indicating a much smaller α, consistent with the much-lower electric-field strength. We also tested non-catalytic, but electrically conductive, ACB. While we found BPM junctions with ACB to be unstable at high current, we were able to collect temperature-dependent data at $\leqslant 50$ mA cm^{-2}. Analysis of the data after correction for degradation (like the correction for pristine BPMs, Figure B.4), yielded α of 0.02 to 0.04 (Figure B.8), much larger than for the TiO_2-P25 catalyzed BPM. This finding is consistent with our interpretation of α here, and the fact that ACB is an electronic conductor that screens and focuses the electric field to the boundaries of the BPM

interfacial layer.

In bulk water, WD occurs through rare electric-field fluctuations and the generated ions recombine quickly if they are not sufficiently separated.[71] This is likely also the case for the pristine BPM without WD catalyst and why it requires a large η_{wd}. The situation is different when there are nanoparticle catalysts where H_2O can transfer H^+ to the oxide surface which can be transported on the nanoparticle surface towards the CEL, while OH^- can be transported in the water "matrix" surrounding the nanoparticles towards the AEL. *Thus, one might view the WD catalyst as facilitating the correct configuration of water and surface for successful proton transfer and the WD reaction to occur.* Compared to the uncatalyzed BPM, our data shows that adding a WD catalyst leads to a dramatic increase in the driving-force-independent proton-transfer conductance G_0, which can be explained by the large number of sites for proton transfer on the catalyst surface. In the isotope experiment, G_0 follows the same dependence on loading for both H_2O and D_2O, and the ratio $G_0(H_2O)/G_0(D_2O)$ is ~10. This is comparable with the ratio of k_D and K_w (Table 3.1), suggesting that G_0 represents both the number density of catalytic sites and the "intrinsic" WD activity of H_2O and D_2O related to their atomic motions. In the experiment where conducting carbon was added, G_0 does not change because the mass of TiO_2-P25 was kept constant as the mass of carbon was varied. Adding carbon further focuses the electric field and thus WD becomes more sensitive to the change in the electric field, which manifests in the increasing α. We further analyzed the relation between E_a and log A to check for compensation effects that have been identified in hydrogen evolution reaction.[37] For catalyzed BPMs, log A is essentially independent of E_a, while for pristine BPMs, some correlation is

observed (Figure B.9).

A molecular interpretation of WD catalysis

We propose a molecular proton-transfer mechanism, where M, M′, and M″ denote different proton acceptor/donor sites on the catalyst surface (Figure 3.5A):

$$H_2O + MO^- \rightarrow OH^- + MOH \quad \text{(R1)}$$

$$MOH + M'OH \rightarrow MO^- + M'OH_2^+ \quad \text{(R2)}$$

$$M'OH_2^+ + M''OH \rightarrow M'OH + M''OH_2^+ \quad \text{(R3)}$$

$$M''OH_2^+ + H_2O \rightarrow M''OH + H_3O^+ \quad \text{(R4)}$$

This mechanism is reminiscent of the basic and acidic two-step mechanism proposed previously.[15] Here we use the acidic two-step mechanism (R5 and R6) for discussion, but the basic case is analogous.

$$H_2O + MOH_2^+ \rightarrow MOH + H_3O^+ \qquad K_5 = K_a \quad \text{(R5)}$$

$$MOH + H_2O \rightarrow MOH_2^+ + OH^- \qquad K_6 = K_w/K_a \quad \text{(R6)}$$

In the previously proposed two-step mechanisms,[15] there is an underlying assumption that the catalytic cycle occurs on the same site, which means that H_3O^+ and OH^- are produced in close proximity. This constrains the optimal K_a of the example MOH_2^+ site; if the K_a is large (more acidic), then R5 is more favored (and usually faster), but this means that R6 is less favored (and usually slower) because its equilibrium constant is K_w/K_a (if we assume a constant K_w). This is why previous calculations conclude that a pK_a (or equivalently pK_b) of ~7 of the catalytic site should give the best performance.[30]

The new mechanism proposed here involving surface proton transfer (R2 and R3) enables

R1 and R4 to occur at different sites (M and M″) on the catalyst surface and thus generate H_3O^+ and OH^- which are separated in space. The K_a of the M and M″ site are less constrained than in the single-site model. The M site could be basic so that R1 is favored and fast, while M″ site could be acidic so that R4 is favored and fast, and the relevant surface K_a will also depend on the degree of polarization of the nanoparticle catalysts[72]. The rate-determining step likely depends on the WD catalyst type, because chemically different surfaces will have different acid-base behavior and surface proton-adsorption isotherms. When the loading is small, R1 or R4 might be rate determining. Since these two steps might be more sensitive to the local electric field, we might observe a larger α. In contrast, at optimal loading, the surface-transport steps (R2 and R3) might be rate determining leading to Ohmic behavior ($\alpha = 0$), as the experiment shows. Interestingly, we note that theoretical calculations find a free-energy barrier of 25 ± 4 kJ mol^{-1} for proton transfer and 32 ± 4 kJ mol^{-1} for dissociative adsorption of water on the TiO_2 anatase (101) surface in water,[59] values similar to our experimental results. R2 and R3 thus may have a free-energy barrier ~25 kJ mol^{-1}, while for R1 and R4 it may be ~32 kJ mol^{-1}.

CONCLUSIONS

We developed a membrane-potential-sensing method with two integrated reference electrodes in BPM electrolyzers to directly measure the WD overpotential. Through variable-temperature studies and Arrhenius-type analysis with TiO_2-P25 as a model, but effective, WD catalyst, we found that the apparent activation energy E_a only weakly depends on η_{wd} while the pre-exponential factor A is directly proportional to η_{wd}. D_2O requires higher η_{wd} to drive WD than H_2O, but surprisingly the E_a are similar and the higher η_{wd} is due to the lower pre-exponential

factor. Electronically conducting acetylene carbon black (ACB) improves the performance by lowering E_a, consistent with a field-focusing effect. We developed a "BPM equation" with three parameters to quantitatively describe the temperature-dependent kinetics and discussed the physical meaning of these parameters. We proposed a new molecular mechanism involving rate-determining proton transfer to/from water and proton transport across the catalyst surface under applied voltage. These findings provide insights into, and inspire new strategies for development of, other electrochemical process where WD is relevant, e.g., alkaline hydrogen evolution reaction (HER) and CO_2 electroreduction.[21, 45-46]

One limitation of the present work is the lack of direct evidence for the proposed mechanism due to the inherent difficulty of studying buried interfaces like the BPM junction. More experimental and computational studies, at an appropriately high level of theory that captures the molecular details of water and surfaces, are needed to test the new model presented here. The proposed BPM equation is also semi-empirical. Developing an analytical formalism based on a detailed molecular mechanism remains challenging due to the complexity of the BPM junction and it being a buried interface. A general equation for the current density in a one-dimensional model is

$$j = F \int_{\mathrm{BPM}} \left(k_{\mathrm{D}} c_{\mathrm{H_2O}} - k_{\mathrm{R}} c_{\mathrm{H^+}} c_{\mathrm{OH^-}}\right) dx \qquad (3.9)$$

where k_D and k_R are net dissociation and recombination reaction rate constants, c is the concentration, x is the coordinate perpendicular to the planar junction. The values for k_D, k_R, and c probably all depend on x, η_{wd} or electric field, and the details of the catalyst.[73-74] However, there is no experimental data regarding the electric potential/field and H_2O, H^+, and OH^- concentration

profiles in the BPM junction. *Operando* measurements of pH, pOH, and electric-field profiles in the BPM junction, perhaps with fluorescent indicators and Stark-effect-based probes, would be valuable.[75]

Accurate simulations of the interface molecular and continuum chemistry and physics of the system are also needed.[68, 76] MD and DFT calculations to test the various proton-transfer WD-reaction mechanisms at nanoparticle/water interface under a strong electric field will provide insight into elementary reaction barriers and reaction pathways. We also note that in the Eyring equation from transition-state theory, the pre-exponential factor A is related to the entropy of activation $\Delta S^{\ddagger}$.[77] Our observation that A is proportional to η_{wd} may also mean that $\Delta S^{\ddagger}$ changes with η_{wd}, which can be elucidated by theory and computation. It also remains unclear whether all the nanoparticles participate in the WD reaction or only those near the AEL and CEL. At the molecular scale, we don't know what sites are active for WD on the surface. We presume the bridging and/or terminal oxo/hydroxyl species are the active sites as proton acceptors or donors, but there may be other WD sites. Molecularly precise analogs would be of value to study, for example, small molecules with well-defined pK_a's can be tethered to surfaces of nanoparticles (*e.g.*, –COOH, –NH_2, –PO_3H from commercial silanes, etc.).

Nonetheless, the developed BPM equation sets a foundation for WD catalyst development and future fundamental studies. Any theory should reduce to the semi-empirical equation under appropriate assumptions. The BPM equation also does not explicitly separate the forward WD reaction and reverse H^+/OH^- recombination reaction, which may proceed via different mechanisms or with different rate-determining steps. With further experimental

optimization, future work could assess larger ranges of current and η_{wd} to better determine the α values that describe the reaction kinetics. Temperature-dependence and kinetic-isotopic-effect experiments for different WD catalysts in both forward and reverse bias (to obtain full polarization curves) are needed, probably using a H_2-pump-type cell instead of a water electrolyzer platform.[78]

EXPERIMENTAL PROCEDURES

The experimental procedures are modified from our previous report [23]. The anode gas-diffusion electrode/layer (GDE/GDL) was fabricated by spray coating one vial of anode ink (dispersed by sonication), containing 0.2 g Co_3O_4 (30–50 nm, US Research Nanomaterials, Inc.), 1.0 g H_2O, 3.4 g isopropyl alcohol (IPA), and 0.2 g PiperION-A5 Ionomer Suspension (TP-85, 5% w/w, Versogen), onto a 5 cm × 5 cm stainless steel 25AL3 (Bekaert Bekipor®) support taped on a hot plate of 90 °C. The loading was ~2 mg cm^{-2}. Then PiperION-A5 ionomer suspension (as received) was sprayed onto the catalysts until the mass of the ionomer reached 10%–20% of the catalyst mass. The GDL was cut into 1.0 cm × 1.0 cm coupons. The cathode GDL was fabricated in a similar way with Toray Carbon Paper 090 (wet proofed, Fuel Cell Store) as the substrate, and two vials of ink containing 0.1 g Pt black (high surface area, Fuel Cell Store), 1.5 g H_2O, 1.7 g IPA, 0.1 g D520 Nafion™ dispersion (alcohol-based 1000 EW at 5 wt%, Fuel Cell Store).

PiperION-A40-HCO3 (TP-85, 40-μm thick, Versogen) membrane was soaked in 0.5 M KOH for > 1 h, stored in fresh 0.5 M KOH, and rinsed in ultrapure H_2O before being used as the anion exchange layer (AEL). The Nafion™ 212 (Fuel Cell Store) membrane was soaked and

stored in H_2O and used as the cation exchange layer (CEL). Both membranes are cut into 1.5 cm × 1.5 cm for use as the AEL and CEL in the BPM, and 1.5 cm × 7.5 cm as the AEL and CEL sensing strips. The WD catalyst was spin-coated onto the CEL. TiO_2-P25 (Aeroxide® Nippon Aerosil Co., Ltd.) was dispersed in a H_2O/IPA mixture (1:1 by weight) with different wt% solids to make the ink. The edges of a CEL (1.5 cm × 1.5 cm) were taped on a glass slide. The ink was added onto CEL until fully covered and then the sample spun at 3000 rpm for 30 s to create a uniform thin layer of WD catalyst. Polystyrene beads (Alpha Nanotech, non-functionalized, 100 nm, 10 mg/ml) were diluted with IPA to make a 0.5 wt% dispersion in H_2O/IPA mixture (1:1 by weight) and spun twice onto the CEL in the same way.

Due to the poor dispersibility of acetylene carbon black (ACB), spin coating does not give good quality catalyst coating. Therefore, spray coating was used. A 2 wt% mother ink of TiO_2-P25 was prepared in water and sonicated until well dispersed. Based on the target mass ratio of ACB and TiO_2-P25, ACB was weighed in a 20 mL vial (e.g., 50 wt% required 2 mg of ACB), then 200 mg of the 2 wt% TiO_2-P25 mother ink (equivalent to 4 mg of TiO_2-P25) is added. Water is added until the total mass reaches 0.5 g, then 1.7 g of IPA is added and the mixture is sonicated until well dispersed. A CEL of 1.5 cm × 1.5 cm is taped on a petri dish and placed on a hot plate of 90 °C. The ink is spray coated onto the CEL. To improve the uniformity, the dish is rotated 90° every 10 spray bursts. After spraying, the tapes were removed and the coated CEL was moved into pure water for later use.

The electrolyzer uses PEM fuel-cell hardware (Fuel Cell Store) with the original graphite anode flow field replaced by a homemade stainless-steel one. For step-by-step procedures

regarding cell construction and assembly, see the **Supplemental Experimental Procedures**. The active geometric area (1 cm^2) is defined by the gaskets and current is normalized to this geometric area to give current density in all the provided plots. Ultrapure H_2O (18.2 MΩ cm) heated at different temperatures was fed to both the anode and cathode so that the electrolyzer temperature was 25, 35, 45, or 55 ± 2 °C (error estimated as the maximum fluctuation). D_2O (99.9%, Cambridge Isotope Laboratories) is used instead of H_2O for kinetic-isotope effect experiments. Conventionally, Ag|AgCl reference electrodes are usually used measure WD voltage of BPMs in H-cells, but the frits dissolve in strong base and the potentials are unreliable due to formation of AgO. We used a saturated calomel electrode (SCE) in 0.1 M H_2SO_4 and a Hg|HgO reference electrode (RE) in 0.1 M KOH. The WD voltage V_{wd} was then measured as $V_{\mathrm{wd}} = V_{\mathrm{wd}}^{\mathrm{raw}} + \Delta V_{\mathrm{RE}}$, where $V_{\mathrm{wd}}^{\mathrm{raw}}$ is the as-measured voltage between Hg|HgO and SCE during test, and $\Delta V_{\mathrm{RE}} = 0.136$ V (measured in saturated KCl solution) is the correction factor for the difference between Hg|HgO and SCE in the same solution at equilibrium without the effect of transmembrane voltages. To calculate η_{wd}, it is not strictly necessary to correct for ΔV_{RE} as

$$\eta_{\mathrm{wd}} \equiv V_{\mathrm{wd}} - V_{\mathrm{wd,eq}} = (V_{\mathrm{wd}}^{\mathrm{raw}} + \Delta V_{\mathrm{RE}}) - \left(V_{\mathrm{wd,eq}}^{\mathrm{raw}} + \Delta V_{\mathrm{RE}}\right) = V_{\mathrm{wd}}^{\mathrm{raw}} - V_{\mathrm{wd,eq}}^{\mathrm{raw}} \qquad (3.10)$$

where the subscript "eq" denotes the equilibrium value, i.e., when current density $j = 0$ mA cm^{-2}.

The ionic conductivity of the AEL (PiperION TP-85) at 25 °C is ~80 mS cm^{-1}. With a thickness of 40 μm, the areal ionic resistance of the AEL is ~0.05 Ω cm^2.[79] The reported ionic conductivity of the CEL (Nafion 212) ranges from ~50 to ~100 mS cm^{-1} at 30 °C.[80-81] Assuming it is ~75 mS cm^{-1} and a thickness of 50 μm, the areal ionic resistance of the CEL is ~0.07 Ω cm^2. The measured R_{wd} is ~0.6 Ω cm^2 for optimal TiO_2-P25 loading at 25 °C (Figure B.1) and only

about half of the combined AEL and CEL ohmic voltage drop is measured along with η_{wd} using our membrane potential sensing approach. We thus ignore effects of AEL and CEL ionic resistance in our analyses.

The electrochemical tests were performed with a two-channel BioLogic VSP-300 potentiostat. For channel 1, the P1 and S1 leads were connected to the anode current collector, P2, S2 and S3 were connected to the cathode current collector (P = power lead, S = sense lead). For channel 2, S1 was connected to the Hg|HgO RE, S2 to the cathode current collector, and S3 to the SCE RE. P1 and P2 were not used. Channel 1 and channel 2 are synchronized during the experiment. Channel 2 records voltage every 0.1 s. The current was applied by Channel 1 and stepped up at j = 10, 50, 100, 150, …, 500 mA cm^{-2} (10 s each step) and held at 500 mA cm^{-2} for 10 min (if the voltage exceeds the maximum range of the potentiostat, then held at the highest j). Then galvanostatic electrochemical impedance spectroscopy (GEIS) was measured from 600 kHz to 60 mHz with four points per decade at 500, 450, 400, …, 100, 50, 40, 30, 20, 10, 5 mA cm^{-2} with an AC amplitude of 6% of the applied DC current density (for 10 and 5 mA cm^{-2}, an amplitude of 1 mA cm^{-2} was used). The impedance data were fit with impedance.py.[82-83] The $R(j)$ plot is extrapolated by cubic spline to j = 0 mA cm^{-2} so that the integral $\eta_{wd} = \int_0^j R_{wd}(j)\mathrm{d}j$ begins at 0. For the temperature-dependent tests, after GEIS, j was stepped up again (5 s each step) and held at 500 mA cm^{-2} for 2 min. Then j was stepped down at 500, 450, 400, …, 100, 50, 40, 30, 20, 10, 5 mA cm^{-2} (5 s each step). The last three seconds of each step was averaged to produce the polarization curves. For the BPM without catalyst, j was decreased by a factor of 100 to prevent large voltage polarizations. The temperature was then changed, and the procedure

repeated. Temperatures from 25 to 55 °C (every 10 °C) and back to 25 °C were used. Two temperature cycles were performed for each test. A degradation (increase in voltage) was sometimes observed in the first temperature step up process for low-catalyst-loading samples, after which the performance (at the same temperature) was repeatable during cycling. Thus, the first 25, 35, and 45 °C data were not used for the temperature-dependence analysis for those samples (Figure B.2).

BRIDGE

Chapter III includes studies of temperature dependence of water dissociation catalyst in bipolar membranes, and the analysis of water dissociation kinetics and mechanism analysis. It extended the studies in Chapter III to a more fundamental level.

REFERENCES

1. Giesbrecht, P. K.; Freund, M. S., Recent advances in bipolar membrane design and applications. *Chem. Mater.* **2020,** *32* (19), 8060-8090.

2. Pärnamäe, R.; Mareev, S.; Nikonenko, V.; Melnikov, S.; Sheldeshov, N.; Zabolotskii, V.; Hamelers, H. V. M.; Tedesco, M., Bipolar membranes: A review on principles, latest developments, and applications. *J. Membr. Sci.* **2021,** *617*, 118538.

3. Blommaert, M. A.; Aili, D.; Tufa, R. A.; Li, Q.; Smith, W. A.; Vermaas, D. A., Insights and challenges for applying bipolar membranes in advanced electrochemical energy systems. *ACS Energy Lett.* **2021,** *6* (7), 2539-2548.

4. Yan, Z.; Mallouk, T. E., Bipolar membranes for ion management in (photo)electrochemical energy conversion. *Acc. Mater. Res.* **2021,** *2* (12), 1156-1166.

5. Miesiac, I.; Rukowicz, B., Bipolar membrane and water splitting in electrodialysis. *Electrocatalysis* **2022,** *13* (2), 101-107.

6. Strathmann, H., Electrodialysis, a mature technology with a multitude of new applications. *Desalination* **2010,** *264* (3), 268-288.

7. Shehzad, M. A.; Yasmin, A.; Ge, X.; Ge, Z.; Zhang, K.; Liang, X.; Zhang, J.; Li, G.; Xiao, X.; Jiang, B.; Wu, L.; Xu, T., Shielded goethite catalyst that enables fast water dissociation in bipolar membranes. *Nat. Commun.* **2021,** *12* (1), 9.

8. Fu, R.; Wang, H.; Yan, J.; Li, R.; Jiang, C.; Wang, Y.; Xu, T., Asymmetric bipolar membrane electrodialysis for acid and base production. *AIChE J.* **2022,** *n/a* (n/a), e17957.

9. Lu, H.; Wang, L.; Wycisk, R.; Pintauro, P. N.; Lin, S., Quantifying the kinetics-energetics performance tradeoff in bipolar membrane electrodialysis. *J. Membr. Sci.* **2020,** *612*, 118279.

10. Bazinet, L.; Lamarche, F.; Ippersiel, D., Bipolar-membrane electrodialysis: Applications of electrodialysis in the food industry. *Trends Food Sci. Technol.* **1998,** *9* (3), 107-113.

11. Tongwen, X., Electrodialysis processes with bipolar membranes (EDBM) in environmental protection—a review. *Resour. Conserv. Recycl.* **2002,** *37* (1), 1-22.

12. Ahlfield, J. M.; Liu, L.; Kohl, P. A., PEM/AEM junction design for bipolar membrane fuel cells. *J. Electrochem. Soc.* **2017,** *164* (12), F1165-F1171.

13. Peng, S.; Xu, X.; Lu, S.; Sui, P.-C.; Djilali, N.; Xiang, Y., A self-humidifying acidic–alkaline bipolar membrane fuel cell. *J. Power Sources* **2015,** *299*, 273-279.

14. Yan, Z.; Wycisk, R. J.; Metlay, A. S.; Xiao, L.; Yoon, Y.; Pintauro, P. N.; Mallouk, T. E., High-voltage aqueous redox flow batteries enabled by catalyzed water dissociation and acid–base neutralization in bipolar membranes. *ACS Cent. Sci.* **2021,** *7* (6), 1028-1035.

15. Oener, S. Z.; Foster, M. J.; Boettcher, S. W., Accelerating water dissociation in bipolar membranes and for electrocatalysis. *Science* **2020,** *369* (6507), 1099-1103.

16. Powers, D.; Mondal, A. N.; Yang, Z.; Wycisk, R.; Kreidler, E.; Pintauro, P. N., Freestanding bipolar membranes with an electrospun junction for high current density water splitting. *ACS Appl. Mater. Interfaces* **2022,** *14* (31), 36092-36104.

17. Xie, K.; Miao, R. K.; Ozden, A.; Liu, S.; Chen, Z.; Dinh, C.-T.; Huang, J. E.; Xu, Q.; Gabardo, C. M.; Lee, G.; Edwards, J. P.; O'Brien, C. P.; Boettcher, S. W.; Sinton, D.; Sargent, E. H., Bipolar membrane electrolyzers enable high single-pass CO_2 electroreduction to multicarbon products. *Nat. Commun.* **2022,** *13* (1), 3609.

18. Blommaert, M. A.; Sharifian, R.; Shah, N. U.; Nesbitt, N. T.; Smith, W. A.; Vermaas, D. A., Orientation of a bipolar membrane determines the dominant ion and carbonic species transport in membrane electrode assemblies for CO_2 reduction. *J. Mat. Chem. A* **2021,** *9* (18), 11179-11186.

19. Marin, D. H.; Perryman, J. T.; Hubert, M. A.; Lindquist, G. A.; Chen, L.; Aleman, A. M.; Kamat, G. A.; Niemann, V. A.; Stevens, M. B.; Boettcher, S. W.; Nielander, A. C.; Jaramillo, T. F., Hydrogen production with seawater-resilient bipolar-membrane electrolyzers. *Joule* **2023,** *in review*.

20. Subbaraman, R.; Tripkovic, D.; Strmcnik, D.; Chang, K. C.; Uchimura, M.; Paulikas, A. P.; Stamenkovic, V.; Markovic, N. M., Enhancing hydrogen evolution activity in water splitting by tailoring Li^+-$Ni(OH)_2$-Pt interfaces. *Science* **2011,** *334* (6060), 1256-1260.

21. McCrum, I. T.; Koper, M. T. M., The role of adsorbed hydroxide in hydrogen evolution reaction kinetics on modified platinum. *Nat. Energy* **2020,** *5* (11), 891-899.

22. Marcandalli, G.; Monteiro, M. C. O.; Goyal, A.; Koper, M. T. M., Electrolyte effects on CO_2 electrochemical reduction to CO. *Acc. Chem. Res.* **2022,** *55* (14), 1900-1911.

23. Chen, L.; Xu, Q.; Oener, S. Z.; Fabrizio, K.; Boettcher, S. W., Design principles for water dissociation catalysts in high-performance bipolar membranes. *Nat. Commun.* **2022,** *13* (1), 3846.

24. Onsager, L., Deviations from ohm's law in weak electrolytes. *J. Chem. Phys.* **1934,** *2* (9), 599-615.

25. Kunst, B.; Lovreček, B., Electrochemical properties of the ion-exchange membranes junction. II. *Croat. Chem. Acta* **1962,** *34* (4), 219-229.

26. Cai, J.; Griffin, E.; Guarochico-Moreira, V. H.; Barry, D.; Xin, B.; Yagmurcukardes, M.; Zhang, S.; Geim, A. K.; Peeters, F. M.; Lozada-Hidalgo, M., Wien effect in interfacial water dissociation through proton-permeable graphene electrodes. *Nat. Commun.* **2022,** *13* (1), 5776.

27. Cai, J.; Griffin, E.; Guarochico-Moreira, V.; Barry, D.; Xin, B.; Huang, S.; Geim, A. K.; Peeters, F. M.; Lozada-Hidalgo, M., Photoaccelerated water dissociation across one-atom-thick electrodes. *Nano Lett.* **2022,** *22* (23), 9566-9570.

28. Simons, R.; Khanarian, G., Water dissociation in bipolar membranes: Experiments and theory. *J. Membrane Biol.* **1978,** *38* (1), 11-30.

29. Simons, R., Strong electric field effects on proton transfer between membrane-bound amines and water. *Nature* **1979,** *280* (5725), 824-826.

30. Strathmann, H.; Krol, J. J.; Rapp, H. J.; Eigenberger, G., Limiting current density and water dissociation in bipolar membranes. *J. Membr. Sci.* **1997,** *125* (1), 123-142.

31. Yan, Z.; Zhu, L.; Li, Y. C.; Wycisk, R. J.; Pintauro, P. N.; Hickner, M. A.; Mallouk, T. E., The balance of electric field and interfacial catalysis in promoting water dissociation in bipolar membranes. *Energy Environ. Sci.* **2018,** *11* (8), 2235-2245.

32. Ramírez, P.; Rapp, H. J.; Reichle, S.; Strathmann, H.; Mafé, S., Current‐voltage curves of bipolar membranes. *J. Appl. Phys.* **1992,** *72* (1), 259-264.

33. Aritomi, T.; van den Boomgaard, T.; Strathmann, H., Current-voltage curve of a bipolar membrane at high current density. *Desalination* **1996,** *104* (1), 13-18.

34. Hurwitz, H. D.; Dibiani, R., Investigation of electrical properties of bipolar membranes at steady state and with transient methods. *Electrochim. Acta* **2001,** *47* (5), 759-773.

35. Hurwitz, H. D.; Dibiani, R., Experimental and theoretical investigations of steady and transient states in systems of ion exchange bipolar membranes. *J. Membr. Sci.* **2004,** *228* (1), 17-43.

36. He, Z.-D.; Chen, Y.-X.; Santos, E.; Schmickler, W., The pre-exponential factor in electrochemistry. *Angew. Chem. Int. Ed.* **2018,** *57* (27), 7948-7956.

37. Narangoda, P.; Spanos, I.; Masa, J.; Schlögl, R.; Zeradjanin, A. R., Electrocatalysis beyond 2020: How to tune the preexponential frequency factor. *ChemElectroChem* **2022,** *9* (4), e202101278.

38. Zeradjanin, A. R.; Narangoda, P.; Masa, J.; Schlögl, R., What controls activity trends of electrocatalytic hydrogen evolution reaction?—Activation energy versus frequency factor. *ACS Catal.* **2022,** *12* (19), 11597-11605.

39. Zeradjanin, A. R.; Grote, J.-P.; Polymeros, G.; Mayrhofer, K. J. J., A critical review on hydrogen evolution electrocatalysis: Re-exploring the volcano-relationship. *Electroanalysis* **2016,** *28* (10), 2256-2269.

40. Oener, S. Z.; Twight, L. P.; Lindquist, G. A.; Boettcher, S. W., Thin cation-exchange layers enable high-current-density bipolar membrane electrolyzers via improved water transport. *ACS Energy Lett.* **2021,** *6* (1), 1-8.

41. Xu, Q.; Oener, S. Z.; Lindquist, G.; Jiang, H.; Li, C.; Boettcher, S. W., Integrated reference electrodes in anion-exchange-membrane electrolyzers: Impact of stainless-steel gas-diffusion layers and internal mechanical pressure. *ACS Energy Lett.* **2021,** *6* (2), 305-312.

42. Adler, S. B., Reference electrode placement in thin solid electrolytes. *J. Electrochem. Soc.* **2002,** *149* (5), E166.

43. He, W.; Nguyen, T. V., Edge effects on reference electrode measurements in PEM fuel cells. *J. Electrochem. Soc.* **2004,** *151* (2), A185.

44. Zeng, R.; Slade, R. C. T.; Varcoe, J. R., An experimental study on the placement of reference electrodes in alkaline polymer electrolyte membrane fuel cells. *Electrochim. Acta* **2010,** *56* (1), 607-619.

45. Intikhab, S.; Snyder, J. D.; Tang, M. H., Adsorbed hydroxide does not participate in the volmer step of alkaline hydrogen electrocatalysis. *ACS Catal.* **2017,** *7* (12), 8314-8319.

46. Huang, B.; Rao, R. R.; You, S.; Hpone Myint, K.; Song, Y.; Wang, Y.; Ding, W.; Giordano, L.; Zhang, Y.; Wang, T.; Muy, S.; Katayama, Y.; Grossman, J. C.; Willard, A. P.; Xu, K.; Jiang, Y.; Shao-Horn, Y., Cation- and pH-dependent hydrogen evolution and oxidation reaction kinetics. *JACS Au* **2021,** *1* (10), 1674-1687.

47. Eigen, M.; Maeyer, L. d., Untersuchungen über die kinetik der neutralisation. I. *Z. Elektrochem.* **1955,** *59*, 986.

48. Eigen, M.; De Maeyer, L.; Bernal, J. D., Self-dissociation and protonic charge transport in water and ice. *Proc. R. Soc. A: Math. Phys. Eng. Sci.* **1958,** *247* (1251), 505-533.

49. Natzle, W. C.; Moore, C. B., Recombination of hydrogen ion (H^+) and hydroxide in pure liquid water. *J. Phys. Chem.* **1985,** *89* (12), 2605-2612.

50. Sweeton, F. H.; Mesmer, R. E.; Baes, C. F., Acidity measurements at elevated temperatures. VII. Dissociation of water. *J. Solution Chem.* **1974,** *3* (3), 191-214.

51. Shoesmith, D. W.; Lee, W., The ionization constant of heavy water (D_2O) in the temperature range 298 to 523 K. *Can. J. Chem.* **1976,** *54* (22), 3553-3558.

52. Ertl, G.; Gerischer, H., Ein vergleich der kinetik der neutralisationsreaktionen des leichten und schweren wassers. *Z. Elecktrochem.* **1962,** *66*, 560.

53. Yang, Y.; Agarwal, R. G.; Hutchison, P.; Rizo, R.; Soudackov, A. V.; Lu, X.; Herrero, E.; Feliu, J. M.; Hammes-Schiffer, S.; Mayer, J. M.; Abruña, H. D., Inverse kinetic isotope effects in the oxygen reduction reaction at platinum single crystals. *Nat. Chem.* **2023,** *15* (2), 271-277.

54. Mills, R., Self-diffusion in normal and heavy water in the range 1-45°. *J. Phys. Chem.* **1973,** *77* (5), 685-688.

55. *CRC handbook of chemistry and physics: A ready-reference book of chemical and physical data*. 97th ed.; CRC Press Boca Raton: 2017.

56. Lee, S. H.; Rasaiah, J. C., Proton transfer and the mobilities of the H^+ and OH^- ions from studies of a dissociating model for water. *J. Chem. Phys.* **2011,** *135* (12), 124505.

57. Gierer, A., Anomale D^+ -und OD^- -ionenbeweglichkeit in schwerem wasser. *Z. Naturforsch. A* **1950,** *5* (11), 581-589.

58. Bourikas, K.; Kordulis, C.; Lycourghiotis, A., Titanium dioxide (anatase and rutile): Surface chemistry, liquid–solid interface chemistry, and scientific synthesis of supported catalysts. *Chem. Rev.* **2014,** *114* (19), 9754-9823.

59. Calegari Andrade, M. F.; Ko, H.-Y.; Zhang, L.; Car, R.; Selloni, A., Free energy of proton transfer at the water–TiO_2 interface from *ab initio* deep potential molecular dynamics. *Chem. Sci.* **2020,** *11* (9), 2335-2341.

60. Bockris, J. O. M.; Devanathan, M. A. V.; Müller, K., On the structure of charged interfaces. *Proc. R. Soc. A: Math. Phys. Eng. Sci.* **1963,** *274* (1356), 55-79.

61. Willard, A. P.; Reed, S. K.; Madden, P. A.; Chandler, D., Water at an electrochemical interface—a simulation study. *Faraday Discuss.* **2009,** *141* (0), 423-441.

62. Gonella, G.; Backus, E. H. G.; Nagata, Y.; Bonthuis, D. J.; Loche, P.; Schlaich, A.; Netz, R. R.; Kühnle, A.; McCrum, I. T.; Koper, M. T. M.; Wolf, M.; Winter, B.; Meijer, G.; Campen, R. K.; Bonn, M., Water at charged interfaces. *Nat. Rev. Chem.* **2021,** *5* (7), 466-485.

63. Fosdick, S. E.; Knust, K. N.; Scida, K.; Crooks, R. M., Bipolar electrochemistry. *Angew. Chem. Int. Ed.* **2013,** *52* (40), 10438-10456.

64. Guerrero García, G. I.; Olvera de la Cruz, M., Polarization effects of dielectric nanoparticles in aqueous charge-asymmetric electrolytes. *J. Phys. Chem. B* **2014,** *118* (29), 8854-8862.

65. Mafé, S.; Ramírez, P.; Alcaraz, A., Electric field-assisted proton transfer and water dissociation at the junction of a fixed-charge bipolar membrane. *Chem. Phys. Lett.* **1998,** *294* (4), 406-412.

66. Bockris, J. O. M.; Nagy, Z., Symmetry factor and transfer coefficient: A source of confusion in electrode kinetics. *J. Chem. Educ.* **1973,** *50* (12), 839.

67. Wrubel, J. A.; Chen, Y.; Ma, Z.; Deutsch, T. G., Modeling water electrolysis in bipolar membranes. *J. Electrochem. Soc.* **2020,** *167* (11), 114502.

68. Bui, J. C.; Digdaya, I.; Xiang, C.; Bell, A. T.; Weber, A. Z., Understanding multi-ion transport mechanisms in bipolar membranes. *ACS Appl. Mater. Interfaces* **2020,** *12* (47), 52509-52526.

69. Mareev, S. A.; Evdochenko, E.; Wessling, M.; Kozaderova, O. A.; Niftaliev, S. I.; Pismenskaya, N. D.; Nikonenko, V. V., A comprehensive mathematical model of water splitting in bipolar membranes: Impact of the spatial distribution of fixed charges and catalyst at bipolar junction. *J. Membr. Sci.* **2020,** *603*, 118010.

70. Chen, B.; Ivanov, I.; Klein, M. L.; Parrinello, M., Hydrogen bonding in water. *Phys. Rev. Lett.* **2003,** *91* (21), 215503.

71. Geissler, P. L.; Dellago, C.; Chandler, D.; Hutter, J.; Parrinello, M., Autoionization in liquid water. *Science* **2001,** *291* (5511), 2121-2124.

72. Delley, M. F.; Nichols, E. M.; Mayer, J. M., Interfacial acid–base equilibria and electric fields concurrently probed by *in situ* surface-enhanced infrared spectroscopy. *J. Am. Chem. Soc.* **2021,** *143* (28), 10778-10792.

73. Stuve, E. M., Ionization of water in interfacial electric fields: An electrochemical view. *Chem. Phys. Lett.* **2012,** *519-520*, 1-17.

74. Che, F.; Gray, J. T.; Ha, S.; Kruse, N.; Scott, S. L.; McEwen, J.-S., Elucidating the roles of electric fields in catalysis: A perspective. *ACS Catal.* **2018,** *8* (6), 5153-5174.

75. Yan, Z.; Hitt, J. L.; Zeng, Z.; Hickner, M. A.; Mallouk, T. E., Improving the efficiency of CO_2 electrolysis by using a bipolar membrane with a weak-acid cation exchange layer. *Nat. Chem.* **2021,** *13* (1), 33-40.

76. Bui, J. C.; Corpus, K. R. M.; Bell, A. T.; Weber, A. Z., On the nature of field-enhanced water dissociation in bipolar membranes. *J. Phys. Chem. C* **2021,** *125* (45), 24974-24987.

77. Doyle, P. J.; Savara, A.; Raiman, S. S., Extracting meaningful standard enthalpies and entropies of activation for surface reactions from kinetic rates. *React. Kinet. Mech. Catal.* **2020,** *129* (2), 551-581.

78. Mitchell, J. B.; Chen, L.; Langworthy, K.; Fabrizio, K.; Boettcher, S. W., Catalytic proton–hydroxide recombination for forward-bias bipolar membranes. *ACS Energy Lett.* **2022,** *7* (11), 3967-3973.

79. Wang, J.; Zhao, Y.; Setzler, B. P.; Rojas-Carbonell, S.; Ben Yehuda, C.; Amel, A.; Page, M.; Wang, L.; Hu, K.; Shi, L.; Gottesfeld, S.; Xu, B.; Yan, Y., Poly(aryl piperidinium) membranes and ionomers for hydroxide exchange membrane fuel cells. *Nat. Energy* **2019,** *4* (5), 392-398.

80. Cooper, K. R., Progress toward accurate through-plane ion transport resistance measurement of thin solid electrolytes. *J. Electrochem. Soc.* **2010,** *157* (11), B1731.

81. Germer, W.; Harms, C.; Tullius, V.; Leppin, J.; Dyck, A., Comparison of conductivity measurement systems using the example of Nafion and anion exchange membrane. *Solid State Ionics* **2015,** *275*, 71-74.

82. Murbach, M. D.; Schwartz, D. T., Open Software and Datasets for the Analysis of Electrochemical Impedance Spectra. *The Electrochemical Society Interface* **2019,** *28* (1), 51.

83. Murbach, M. D.; Gerwe, B.; Dawson-Elli, N.; Tsui, L.-k., Impedance.py: A python package for electrochemical impedance analysis. *J. Open Source Softw.* **2020,** *5* (52), 2349.

CHAPTER IV

CONCLUDING REMARKS

Co-authored unpublished material with Shannon W. Boettcher.

In this dissertation, we studied the physics and chemistry of water dissociation in bipolar membranes. In Chapter I, we set up a platform using BPMs in a pure water eletrolyzer system and studied different kinds of WD catalysts. We found that there is an important role of the electronic conductivity of WD catalyst, probably affecting the electric field distribution by screening and focusing the electric field near the membrane|catalyst interfaces. There is a general U-shape loading dependence for electronically semiconducting and insulating WD catalyst, which might be a result of the tradeoff between increasing the catalytic sites amount and diluting the electric field. We also used electrochemical impedance method to isolate the WD related part from the total cell voltage. Through AEM and PEM electrolyzers measurements, we also demonstrated that ionic conductivity is not the main contributor to the U-shape loading dependence. Furthermore, in Chapter II, we developed a new technique by integrating two reference electrodes with the electrolyzer hardware to directly measure the WD overpotential. We investigated the temperature dependence of WD and extracted the kinetic parameters using Arrhenius analysis and our newly-proposed BPM equation. The possible physical meanings of the fitting parameters were discussed and finally we proposed a possible molecular mechanism to explain our results.

Further studies could combine experimental and theoretical techniques to investigate mechanisms of WD in the BPM junction in more detail. Here we summarize the possible mechanisms (Figure 4.1). **Mechanism I** is 'intrinsic' WD, where water dissociates in pure bulk water. **Mechanism II** involves the membrane molecular end groups of the AEL and CEL. Since they are organic basic or acidic groups, they might catalyze WD through protonation/deprotonation, *i.e.*, proton transfer.[1] Mechanisms I and II are primarily relevant to pristine BPMs without added WD catalysts. **Mechanism III** describes the WD catalytic effect of nanoparticles (mostly inorganic oxides or metals). We hypothesize two possible pathways. **Mechanism III-a** assumes H_2O dissociates by transferring H^+ to the nanoparticle surface, leaving OH^- in the liquid phase. H^+ transports on the nanoparticle surface towards the CEL and subsequently desorbs to make free H_3O^+. We hypothesize that **III-a** is the most-important mechanism for nanoparticles with surface OH groups, *e.g.*, oxides. **Mechanism III-b** gives an alternative pathway, where H_2O dissociatively adsorbs on the nanoparticle surface, generating H_{ad} and OH_{ad}, which transport on the surface and then desorb into the liquid phase as H^+ and OH^-. We hypothesize that this mechanism might occur on metal surfaces that do not have −OH groups, *e.g.* Pt. A key defining feature of the BPM is the *internal electric field at the BPM junction* (in analogy to a semiconductor *pn* junction), which points from AEL to CEL at equilibrium and under reverse bias, *i.e.*, when WD occurs. We hypothesize that the electric field is key to modulating all the mechanisms above. A major goal could be to understand how the electric field accelerates WD, in conjunction with the surface acid/base groups like −OH.

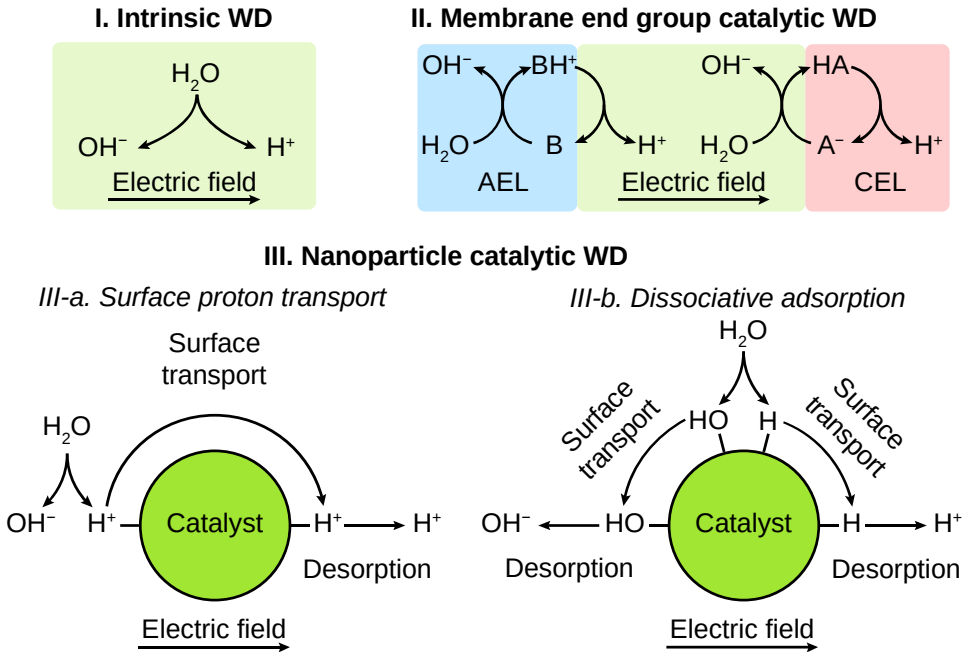

Figure 4.1 Possible mechanisms of WD in BPM junction

H^+ can be understood as combined with H_2O to form H_3O^+. **Mechanisms I** and **II** are mostly relevant to pristine BPMs without nanoparticle catalysts. We expect **III-a** to be the most important mechanism for nanoparticles with surface OH groups, *e.g.*, oxides. **III-b** probably occurs on metal nanoparticles. All mechanisms might be modulated by the electric field. We omit the H_2O which combines with H^+ to form H_3O^+.

One can explore isotopic labeling of the nanoparticle WD catalyst by either directly labeling the surface -OH (*e.g.*, ^{18}O for ^{16}O and D for H) or using groups that contain these isotopic components to functionalize the surface. This can be accomplished by boiling the metal-oxide particles in D_2O and $H_2{}^{18}O$ to drive the isotope exchange prior to building the BPM MEA. By feeding the electrolyzer with H_2O and analyzing if the products (H_2 and O_2) *contain labeled surface atoms from the WD catalyst particles using our GC-MS*, one will obtain precise information on which bond is broken and regenerated during WD on the surface of the WD catalyst in the BPM junction (Figure 4.1, **Mechanism III-a** and **III-b**). Computations could calculate several mechanisms to predict whether O- or H-exchange between the surface is more

likely.

There is a general trend that nanoparticle-catalyzed BPMs are far superior in performance to pristine BPMs without WD catalyst (*i.e.*, simply a laminated CEL and AEL), and the shapes of their polarization curves are different (Figure 3.2). In pristine BPMs, current density j increases exponentially with η_{wd}, like a typical electrochemical reaction with Tafel-like behavior (or Marcus or Butler-Volmer behavior, which are related fundamentally and give similar exponential increase in rate with driving force). In contrast, BPMs with "good" WD catalysts like TiO_2-P25, IrO_x, and bilayer catalysts[2] show a (nearly) linear dependence on η_{wd}. We will leverage electrochemical theory and the concepts of exchange current density j_0, transfer coefficient α, and conductance to empirically explain this difference. For example, we have recently discovered that the pristine BPM has a small j_0 but a large α (*i.e.*, strong dependence on the driving force η_{wd}), while catalyzed BPM has a large j_0 and an $\alpha \sim 0$. One aim is to understand why the systems have different values for these parameters, and how they inform on underlying mechanism.

First, we will consider the pristine BPM case, *i.e.*, without heterogeneous WD catalysts. It has been proposed that the end groups of the membrane polymer molecules have a catalytic effect (Figure 4.1, **Mechanism II**), especially if the group has a p$K_a \sim 7$.[1, 3-4] We use PiperION A40 as the AEL and Nafion 212 as the CEL. It would be difficult for their native end groups to have catalytic effects given the extremely low pK_a of the sulfonic acid group (~ -6) in Nafion and the fact that the nitrogen atom of the quaternary ammonium in PiperION is fully connected to carbon atoms and cannot be protonated. If this is true, then the WD in the pristine BPM is

entirely through a 'non-catalytic' pathway, *i.e.*, intrinsic WD (**Fig. 3**, **Mechanism I**) accelerated by the strong electric field present at the abrupt AEL/CEL interface that lacks intervening WD catalyst. Can this be described with the second Wien effect, as has been invoked (without proof) in the literature?[5] Or does the AEL have some number of $-N(Me)_3H^+$ end groups due to incomplete quaternization?[6] We note that Wien effects were originally observed in a very different context compared with BPMs.[7-10] The first and second Wien effects describe increases in ionic conductivity in electrolytes under high electric fields (i.e. a non-ohmic response). Ionic conductivity is proportional to ionic mobility and ion concentration. The first Wien effect is the ionic mobility of strong electrolytes increasing in high electric field. The second Wien effect is ion concentration in weak electrolytes increasing due to larger dissociation constants of weak electrolytes in high electric fields. Both effects lead to the increase of ionic conductivity by affecting different terms. Wien effects, however, have only be directly observed to our knowledge in *transient* experiments.[7-10] Wien intentionally kept the experiment time short to prevent the heating of the solution from convoluting the electric-field effect. The effects are also ascribed to *solute* in a *bulk solution*, but WD in BPMs is about a *steady-state* process of the *solvent* itself at an *interface(s)*. We hypothesize that that the direct application of the second Wien effect to explain the WD at the junction of BPMs is not completely appropriate, considering these major differences.

Moreover, at equilibrium (open circuit, no current flow), there is a built-in electric field at the BPM junction (like a solid-state semiconductor *pn* junction). Does that mean the dissociation constant of H_2O, K_w, is also changed according to the second Wien effect, even at

equilibrium? In previous simulation studies, the activity coefficients of H^+ and OH^- are set to be related to the electric-field-dependent dissociation rate constant to circumvent this serious issue,[11-12] but the justification for doing this is not apparent. The fully quantum-mechanical calculations, in the presence of a variable strength electric field, could be used to address these issues directly. The degree to which these processes and models are appropriate, and in agreement with experiment, could be directly addressed by comparing trends in activation barrier, mechanism, temperature dependence, field dependence, etc.

We hypothesize that WD catalysts speed up WD through a proton-transfer mechanism (Figure 4.1, **Mechanism III-a**), and the catalytic activity is related to the pK_a of the active groups.[1, 3-4] We also hypothesize that the local electric field at catalyst surfaces is in fact not speeding WD by a Wien effect, but by water pre-organization leading to more water molecules in the appropriate geometry to transfer a proton. This second hypothesis is consistent with the experimental observation that increased applied voltage increases the Arrhenius pre-factor and does not decrease the activation energy.

While pK_a is well-defined for small molecules, it is more difficult to define pK_a's of hydroxyl and other groups on a nanoparticle surface because of interactions with each other. Some have used the concept of "pK_a spectrum" to describe oxide surfaces, although we prefer to model these surfaces by their H^+ adsorption isotherms. In addition, H^+ can move across surfaces easily due to the proximity of protonizable groups, a feature that is not possible with molecular, spatially separated organic acids/bases. *We hypothesize that these special features, i.e. strong interactions and proton exchange on the inorganic oxide catalyst surface, are*

essential for the fast WD activity.

To test these hypotheses small molecules with well-defined groups of pK_a's (*e.g.*, –COOH, $–NH_2$, $–PO_3H$ from commercial silanes from Gelest, etc.) can be tethered to surfaces of nanoparticles. These nanoparticles should show different WD activities according to the proton-transfer mechanism and we predict a correlation between the surface group pK_a and η_{wd}. The limitation of this approach, however, is that each of the functional groups on the surface-attached ligand are electronically isolated from each other and thus a Langmuir-type proton absorption isotherm, which is not what is found on oxide surfaces. The functional group density can be controlled to test how communication via proton transfer between groups modulates WD activity and if Frumkin-type absorption is possible.

Second, one can study the acid-base chemistry of surface -OH groups and model the chemical details of the nanoparticle surfaces. Potentiometric titration and zeta-potential measurements can be used to study the acid-base properties and surface charge of the nanoparticles. Thermogravimetric analysis, solid-state NMR spectroscopy, and infrared spectroscopy will be used to characterize the surface −OH density and type. Using computation there are several possible treatments using different number of pK or pK_a values coupled with descriptions of electrostatic interactions.[13] The experimental measurements could be connected to the quantum mechanical models to identify suitable model surface structures and which computations best describe acid/base activity of the metal oxide surfaces.

The discussion above considered the electric-field induced dissociation of water and the catalytic effect independently, but the interplay between the electric field and the catalyst is an

even more entangling question. For example, the BPM is an *ionic* conductor, and there shouldn't be any *electron* flow at the BPM junction, and the *electronic* properties (*e.g.*, electronic conductivity, dielectric constant etc.) of the WD catalyst would thus naively be assumed to be irrelevant for WD at the BPM junction. Our experimental results show a surprising trend that *electronically* conductive materials (*e.g.*, IrO_x, Pt, $Sb:SnO_2$ etc.) have better performance than insulating materials (*e.g.*, SiO_2). Adding an *electronically* conductive, but non-catalytic material like acetylene carbon black (ACB), to a bad-performance thick layer of TiO_2-P25 significantly improves the WD performance. This result shows there is a synergistic effect between ACB and TiO_2-P25. We hypothesize that electronic conductors screen the electric field in the BPM junction and focus the electric field at the AEL/catalysts and catalyst/CEL interfaces.

These simple and qualitative ideas, however, are incomplete. We don't know whether all the nanoparticles, like TiO_2, participate in the WD reaction or only those near the AEL and CEL. Microscopically, we don't know what sites are active on the surface – the bridging OH, the terminal OH, or both? What are the rate constants for each elementary step? Computational works could add a field to DFT calculations and assess the effect on the material internal potential energy, projected on specific atoms, as well as activation energies using nudged elastic band methods. Mechanistic computational modelling could be used to test different surface sites and processes, and the experimental team can work to enrich those sites and rigorously assess possible correlations between the computational and experimental data.

Some metal nanoparticles (*e.g.*, Pt) are also good WD catalysts. It is unclear whether

the surfaces of Pt are also hydroxylated during operation. We propose that there may be other mechanisms for metals (Figure 4.1, **Mechanism III-b**), for example, dissociative adsorption of water ($H_2O \rightarrow H_{ad} + OH_{ad}$).[2] Then the question is: how does H_{ad} and OH_{ad} turn into H^+ and OH^-, which must be the ultimate current carrying species. We hypothesize that in the high-field limit, the nanoparticle is polarized and the charges redistribute on the surface leading to dissociation surface products more like H^+ and OH^- than charge neutral species. If true, the same process could also occur on oxide surfaces. In this mechanism, H_2O first dissociative adsorbs on the nanoparticle surface as H_{ad} and OH_{ad}, which then transport to different places on the surface (whether as H_{ad} and OH_{ad}, or as H^+ and OH^-) and finally desorb under the influence of electric field as H^+ and OH^-. These hypotheses will be assessed by the computational team by assessing the energetics of each intermediate and how the activation barriers are modulated by applied field strengths.

There are many experimental and theoretical studies on the molecular and dissociative adsorption of H_2O on metal and oxide surfaces, most of which are in vacuum.[14-15] Calculations have been used to extend this study to the liquid/solid interface,[16] and a few model nanoparticles explicitly instead of a facets of a crystal.[17] There are a few studies that incorporate the effect of charges at the interface,[18-19] but there is a lack of studies on the effect of an *external* electric field, which appears central to WD in BPMs. One intrinsic challenge is that nanoparticles are seldom well-defined, but calculations can only be completed on well-defined surfaces. Care thus must be taken whenever comparing experiments with calculations. Some key questions are: what is the activation energy of dissociative adsorption of H_2O on

nanoparticle surfaces, and how do the nanoparticle properties and the "external" electric field affect this? Is there a "volcano plot" between WD activity and surface bond energies? How does the interaction energy between neighboring proton absorption sites play a role?

The stability of BPM is also another important factor for applications. BPM separates the WD reaction from the electron transfer reaction at the electrode, thus we don't need to consider the stability of WD catalysts in an oxidative (or reducing) environment. However, the WD catalyst region at the AEL/CEL region must include materials stable in both strong acid and strong base. The BPM junction is a "bipolar" junction which has drastically different pH's at the AEL side and the CEL side. The dissolution of nanoparticles in either acid (*e.g.*, NiO), base (*e.g.*, SiO_2), or both (*e.g.*, Al_2O_3) seems to be the main contributor to the degradation of BPM over time. Searching for a stable and high-performance WD catalyst, or a strategy to prevent the dissolution but does not inhibit the catalytic activity is still an ongoing process. Designing different types of pristine BPM without catalyst is certainly another possible route, since we don't need to worry about the dissolution of WD catalysts at all, but surprisingly, the pristine BPM degrades much faster than a catalyzed BPM, at least in studies to date. There doesn't seem to be an obvious reason why this is so considering the BPM junction just provides the electric field for water to be dissociated. Thus, the degradation mechanisms of BPMs remain unknown and thus the underlying background degradation processes must be monitored for each catalyst so that the experimental data is trustworthy and suitable for comparing to the computational data.

REFERENCES

1. Simons, R.; Khanarian, G., Water dissociation in bipolar membranes: Experiments and theory. *J. Membrane Biol.* **1978,** *38* (1), 11-30.

2. Oener, S. Z.; Foster, M. J.; Boettcher, S. W., Accelerating water dissociation in bipolar membranes and for electrocatalysis. *Science* **2020,** *369* (6507), 1099-1103.

3. Simons, R., Strong electric field effects on proton transfer between membrane-bound amines and water. *Nature* **1979,** *280* (5725), 824-826.

4. Strathmann, H.; Krol, J. J.; Rapp, H. J.; Eigenberger, G., Limiting current density and water dissociation in bipolar membranes. *J. Membr. Sci.* **1997,** *125* (1), 123-142.

5. Onsager, L., Deviations from ohm's law in weak electrolytes. *J. Chem. Phys.* **1934,** *2* (9), 599-615.

6. Olsson, J. S.; Pham, T. H.; Jannasch, P., Tuning poly(arylene piperidinium) anion-exchange membranes by copolymerization, partial quaternization and crosslinking. *J. Membr. Sci.* **2019,** *578*, 183-195.

7. Wien, M., Über eine Abweichung vom Ohmschen Gesetze bei Elektrolyten. *Ann. Phys.* **1927,** *388* (11), 327-361.

8. Wien, M., Über den Spannungseffekt der Leitfähigkeit bei starken und schwachen Säuren. *Phys. Z.* **1931,** *32*, 545-547.

9. Schiele, J., Über den Spannungseffekt der Leitfähigkeit bei starken und schwachen Säuren. *Ann. Phys.* **1932,** *405* (7), 811-830.

10. Eckstrom, H. C.; Schmelzer, C., The Wien effect: Deviations of electrolytic solutions from Ohm's law under high field strengths. *Chem. Rev.* **1939,** *24* (3), 367-414.

11. Bui, J. C.; Digdaya, I.; Xiang, C.; Bell, A. T.; Weber, A. Z., Understanding multi-ion transport mechanisms in bipolar membranes. *ACS Appl. Mater. Interfaces* **2020,** *12* (47), 52509-52526.

12. Bui, J. C.; Corpus, K. R. M.; Bell, A. T.; Weber, A. Z., On the nature of field-enhanced water dissociation in bipolar membranes. *J. Phys. Chem. C* **2021,** *125* (45), 24974-24987.

13. Lützenkirchen, J., Comparison of 1-pK and 2-pK Versions of Surface Complexation Theory by the Goodness of Fit in Describing Surface Charge Data of (Hydr)oxides. *Environ. Sci. Technol.* **1998,** *32* (20), 3149-3154.

14. Diebold, U., The surface science of titanium dioxide. *Surf. Sci. Rep.* **2003,** *48* (5), 53-229.

15. Bourikas, K.; Kordulis, C.; Lycourghiotis, A., Titanium dioxide (anatase and rutile): Surface chemistry, liquid–solid interface chemistry, and scientific synthesis of supported catalysts. *Chem. Rev.* **2014,** *114* (19), 9754-9823.

16. Calegari Andrade, M. F.; Ko, H.-Y.; Zhang, L.; Car, R.; Selloni, A., Free energy of proton transfer at the water–TiO_2 interface from *ab initio* deep potential molecular dynamics. *Chem. Sci.* **2020,** *11* (9), 2335-2341.

17. Soria, F. A.; Di Valentin, C., Reactive molecular dynamics simulations of hydration shells surrounding spherical TiO2 nanoparticles: implications for proton-transfer reactions. *Nanoscale* **2021,** *13* (7), 4151-4166.

18. Cheng, J.; Sprik, M., Acidity of the Aqueous Rutile TiO2(110) Surface from Density Functional Theory Based Molecular Dynamics. *J. Chem. Theo. Comp.* **2010,** *6* (3), 880-889.

19. Cheng, J.; Sprik, M., The electric double layer at a rutile TiO2 water interface modelled using density functional theory based molecular dynamics simulation. *J. Phys.: Condens. Matter* **2014,** *26* (24), 244108.

APPENDICES

APPENDIX A

CHAPTER II SUPPLEMENTARY INFORMATION

Supplementary Discussion

Complexity of the BPM junction. The BPM junction is a complex system and difficult to study under operating conditions as it relies on the function of buried interface(s) inside the BPM and is usually operated in aqueous electrolytes. Electrochemical impedance and current-voltage analysis is the simplest way to characterize a BPM junction. Conventional BPMs electrochemical tests are carried out in H-cells with soluble supporting electrolytes[1], where salt ions other than H^+ and OH^- also contribute to the current. Due to the non-ideal selectivity of the AEL and CEL, "co-ion" transport complicates the analysis. To circumvent these problems, we have adopted the electrolyzer setup with pure-water feed and no co-ions[2].

Our previous work[2] showed a correlation between the point of zero charge (PZC) of oxide nanoparticles used as bilayer catalysts in the junction, the local pH, and the WD activity. The best systems had basic oxides such as NiO in contact with the AEL and acidic oxides such as IrO_2 in contact with the CEL. The bilayer system, although mechanistically and practically interesting in the context of controlling oxide chemistry for a specific local pH, increases the complexity and is not well-suited for careful studies of the interface BPM physics such as the electric field distribution and electrical/ionic conductivity in the junction. Further, the molecular details of WD remain unclear, particularly for metal nanoparticles where PZC is not a particularly useful concept due to the lack of substantial proton adsorption. The metals may catalyze WD instead

through dissociative adsorption ($H_2O \rightarrow H_{ad} + OH_{ad}$) and desorption, and the electronic conductivity may also be important. In the previous work we also only roughly controlled and studied the effects of WD catalyst loading[2]. In some cases, small amounts of ionomer were added to aid the dispersion of the WD-catalyst ink, which further increases BPM junction complexity. The complications led us to return to well-defined single-layer systems, avoid using ionomer in the junction, and work to make the films as uniform as possible. We expect the new physical insight gathered here will however also be applicable to more-complex multilayer WD-catalyst interfaces.

The second Wien effect. The original experiment that led to the discovery of the second Wien effect was quite different from a BPM. The second Wien effect was discovered by measuring the resistance change of an electrolyte in a cell under high electric field (up to ~2×10^7 V m^{-1}), generated by discharge through a spark gap[3-6]. The time constant of the circuit is ~10^{-5} s or less. The equivalent ionic conductivity of weak electrolytes increased with the electric field and it was proposed to be due to increased dissociation of weak electrolytes. Later Onsager developed a quantitative explanation of this phenomenon and derived an equation to describe the relationship between dissociation constant and electric field[7].

Although the second Wien effect has been used to explain enhanced weak electrolyte dissociation for decades, it is fundamentally not clear whether this is applicable directly to BPMs. As far as we know, the second Wien effect has only been investigated as a non-equilibrium phenomenon over short times. In contrast, a BPM is generally operated in reverse bias at steady state. Another subtly occurs when considering electrochemical equilibrium or open-circuit

voltage, *i.e.* conditions of no net current. Like a semiconductor *pn* junction, the BPM induces a junction electric field, even at equilibrium. If the second Wien effect plays a role here, does it mean that WD is accelerated at equilibrium? This would require that the ionization constant of water K_w is different in the region of large field from that in the field-free region. Answering these questions to cleanly elucidate WD mechanisms and catalysis in BPM junctions are important, but beyond the scope of this specific study.

However, we note that invoking the electric field alone as the source for the increased rate of WD does not seem strictly necessary. A similar interpretation could invoke the *gradient in the electrochemical potential of the ionic charge carriers*, H^+ and OH^-. At electrochemical equilibrium an electric field – *i.e.* a gradient in electric potential – exists in the WD catalyst region, although the gradient in the electrochemical potential of all mobile species is, by definition, zero. This is because, conceptually, the free-energy contribution for the charged species from the electric potential is exactly balanced by the free-energy contribution from the concentration gradient across the BPM junction. If WD dissociation was accelerated by a gradient in electrochemical potential – *i.e.* total free energy per ionic species – rather than gradient in electric potential alone, then the WD rate would not be accelerated at equilibrium and K_w would be a constant across the BPM. A gradient in electrochemical potential could change the rate of WD because if the charged products, H^+ and OH^-, are generated some finite distance from each other. The larger the gradient, the larger the driving force for WD to spatially separated ionic products.

The above interpretation is similar to the general observation that (electro)chemical reaction rates increase exponentially with driving force. For example, in the simple Butler-

Volmer model of charge transfer at an electrode surface, the rate of charge transfer increases exponentially with applied voltage. Some portion of applied potential serves to modulate the free energy of the products relative to the reactants and thus affects the transition state and activation energies. In Butler-Volmer theory, the overpotential driving the reaction is defined typically as $\eta = E - E_{eq}$, where E is the applied electrode potential and E_{eq} is the equilibrium electrode potential. This overpotential can be re-cast in terms of the interfacial electric potential drop $\Delta\phi$ across the double layer because the absolute number of electrons in a (metal) electrode changes little as the electrode potential is changed: $\eta = \Delta\phi - \Delta\phi_{eq}$. Like Butler-Volmer kinetics for electron transfer, we suspect that it is thus indeed not the magnitude of the interfacial electric field in the BPM that is important for accelerating WD, but in fact the local deviation from the equilibrium electric field at any given point within the junction. More work is needed to clarify these basic principles.

Comparison with previous work on electronically conducting materials. Chen *et al.*[8] presented the hypothesis that electronically conducting materials increase the electric field at the WD-catalyst/membrane interfaces to enhance WD. They used graphene and carbon nanotubes (CNT) as electronically conductive materials, and graphene oxide (GO) as an insulating WD catalyst. They tested two thickness (namely, "thin" and "thick") for each catalyst. All of these three catalysts lower the voltage compared to the BPM without catalyst. From quantum-chemistry calculations of proton binding and release, they concluded that graphene and CNTs are not catalytic for WD. GO was found to be a better WD catalyst than either graphene or CNTs although it is an electronically insulating material. GO "thin" films provided better performance than "thick" films, yet for CNTs and graphene there was no apparent thickness dependence. Thus,

they suggest that adding electronically conducting materials to a traditional catalyst could be strategy to improve performance, but do not directly demonstrate/prove the effect.

Here we tested key materials including electronic conductors, semiconductors, and insulators, each one with a quantitatively controlled loading/thickness range and, in some cases, different particle sizes and crystal structures. We show electronic conductors such as Pt and IrO_x achieve good performance at higher loadings compared with semiconducting TiO_2. Adding acetylene carbon black (ACB) to a thick, poorly performing TiO_2 layer substantially improved the performance. Since ACB itself is not catalytically active for WD, there is clearly synergistic effect between ACB and TiO_2. Presumably, TiO_2 provides the catalytic sites while ACB focuses the electric field at the interfaces. We also illustrate the weak role of ionic resistance for the oxide WD-catalyst interlayers and explain the U-shaped trend in voltage with catalyst loading.

Table A.1 Nanoparticles used as water dissociation (WD) catalysts

Material	Supplier
Aeroxide® TiO_2-P25	Nippon Aerosil Co., Ltd.
TiO_2 anatase, 99.5% 5 nm	US Research Nanomaterials, Inc.
TiO_2 anatase, 99.5% 15 nm	US Research Nanomaterials, Inc.
TiO_2 anatase, high purity, 99.98% 30 nm	US Research Nanomaterials, Inc.
TiO_2 anatase, 99%, 100 nm	US Research Nanomaterials, Inc.
TiO_2 rutile, high purity, 99.9+%, 30 nm	US Research Nanomaterials, Inc.
SiO_2 99+%, 20-30 nm	US Research Nanomaterials, Inc.
Antimony tin oxide (ATO, SnO_2:Sb_2O_3 = 90:10, 30 nm, high purity, 99.95+%)	US Research Nanomaterials, Inc.
IrO_x	Pajarito Powder
Platinum black (high surface area)	Fuel Cell Store
Acetylene carbon black (99.99%, 50% compressed)	Strem Chemicals

Table A.2 BET surface areas and cumulative pore volumes based on the BJH method for TiO_2 nanoparticles

Material	BET SSA ($m^2\ g^{-1}$)	Cumulative Pore Volume V_p ($cm^3\ g^{-1}$)
TiO_2-P25	92.6	0.703
TiO_2-Anatase 5 nm	285.9	0.596
TiO_2-Anatase 15 nm	77.7	0.368
TiO_2-Anatase 30 nm	53.3	0.297
TiO_2-Anatase 100 nm	14.3	0.038
TiO_2-Rutile 30 nm	23.0	0.054

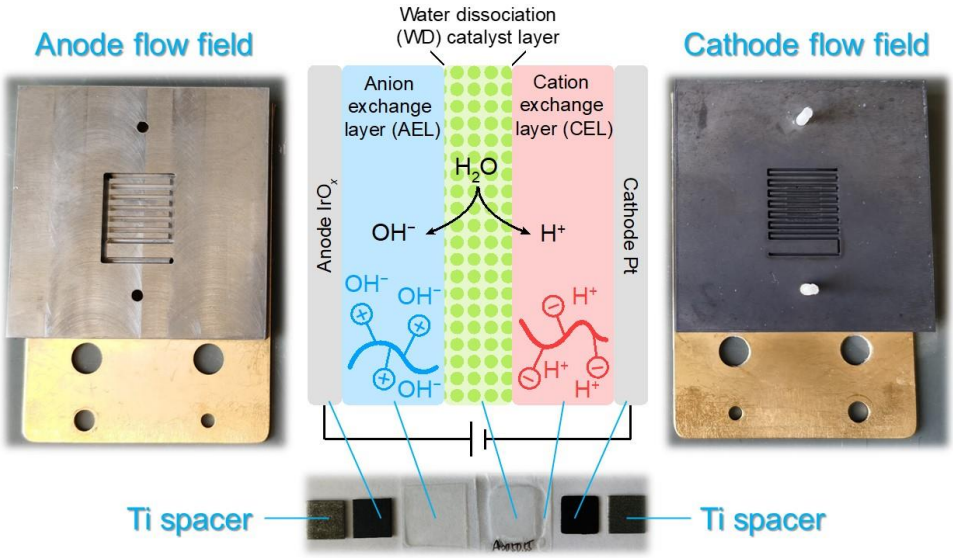
Anode flow field
Water dissociation
(WD) catalyst layer
Cathode flow field
Anion
exchange
layer (AEL)
Cation
exchange
layer (CEL)
H_2O
OH^-
H^+
Anode IrO_x
Cathode Pt
Ti spacer
Ti spacer

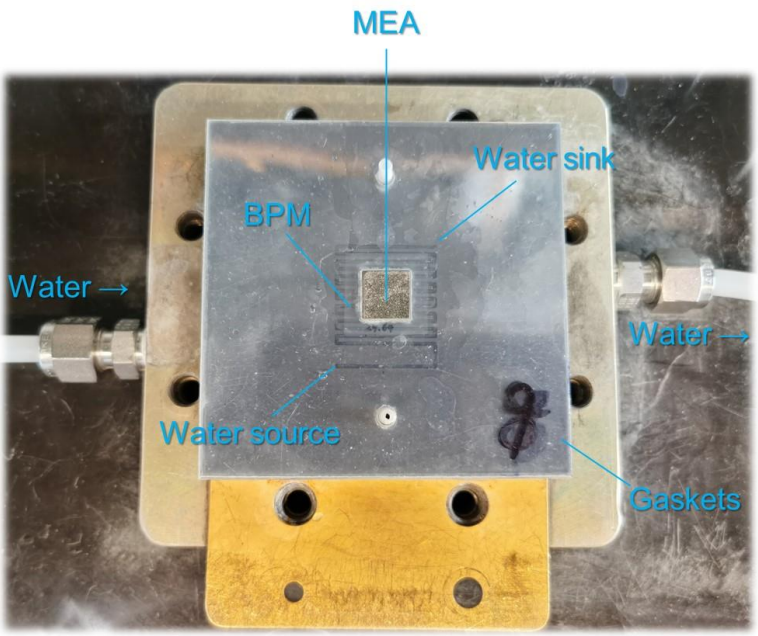
MEA
Water sink
BPM
Water →
Water →
Water source
Gaskets


O_2/Water →
Water →
Anode
H_2/Water →
Water →
Anode
Cathode

Figure A.1 MEA electrolyzer setup

Pure water is fed into both anode and cathode. Water flows along the serpentines on the flow fields and through the porous Ti spacers and GDLs to reach the BPM. The flow fields also serve as points to attach the potentiostat power and voltage sense leads. The construction follows standard procedures from the membrane-electrolyzer and fuel-cell community, as described in the Methods section. The electrocatalysts, not to be confused with the *water dissociation* (WD) catalysts in the BPM, are mixed with ionomer and sprayed onto gas diffusion layers (GDLs) which provide electrical connection to catalyst. Impedance measurements are made also on this cell. As discussed in the text, there is a resistance due to the ionomer layer, as well as the membrane itself, and these result in a lumped high-frequency ohmic resistance (R_s in Figure 2.5). The anode and cathode charge-transfer resistances and capacitances (R_{ct} and C_{ct}) are not easily separated. With our careful studies, however, we have rigorously identified and separated the impedance associated with the BPM junction (R_{wd}) where water is dissociated and transported to the CEL and AEL components of the BPM.

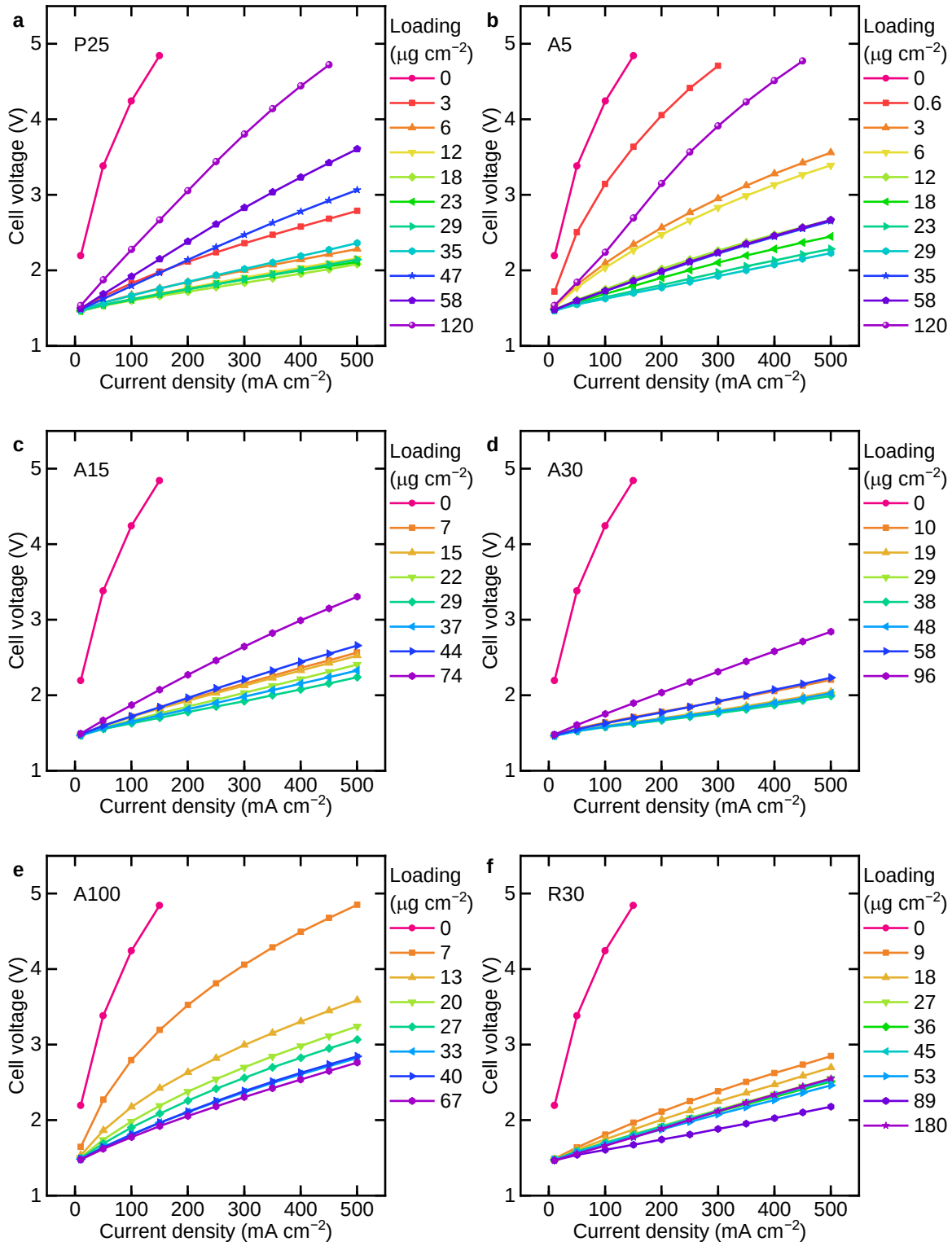

Figure A.2 Performance of BPM electrolyzers with various TiO_2 as WD catalysts

Polarization curves of BPM electrolyzers with different loading of WD catalysts deposited by spray coating. **a**, TiO_2-P25. **b**, Anatase 5 nm. **c**, Anatase 15 nm. **d**, Anatase 30 nm. **e**, Anatase 100 nm. **e**, Rutile 30 nm.

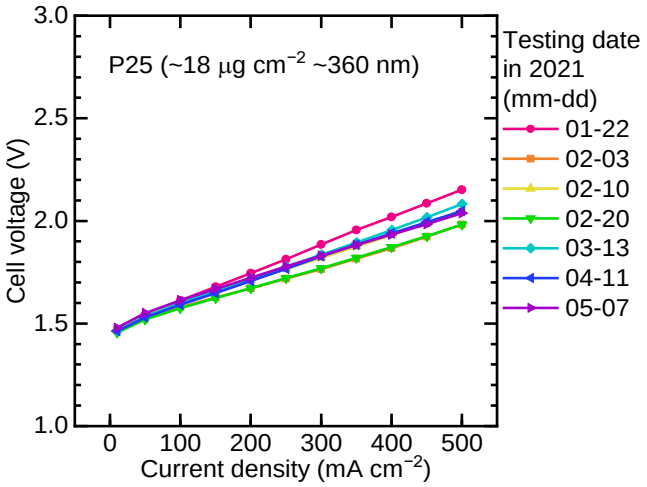

Figure A.3 Reproducibility of electrolyzer performance of optimal TiO_2-P25 loading

TiO_2-P25 (~18 μg cm^{-2}) was deposited by spray coating. Tests were carried out at different dates with different batches of GDLs. The cell voltage at 500 mA cm^{-2} is 2.05 ± 0.06 V (standard error of 7 samples). The temperature is maintained 55 ± 2 °C. Benchmark AEM electrolyzers[9] with the same anode/cathode catalysts and Piperion AEM (and the same temperature) operate at ~1.85 V at 0.5 A cm^{-2}. This is only slightly worse than the BPM electrolyzer reported here, even though the BPM includes more membrane resistance from the use of a PEL and AEL in series, than the AEM alone, and must drive the WD reaction. This is because the BPM electrolyzers operates the cathode hydrogen evolution reaction in acid which is much faster than for the AEM electrolyzer which operates the cathode in locally alkaline conditions where the hydrogen evolution kinetics are much slower. This result therefore shows the substantial opportunity of BPM electrolyzer platforms to achieve good performance while also controlling the ion transfer and thus the local pH environment at each electrode.

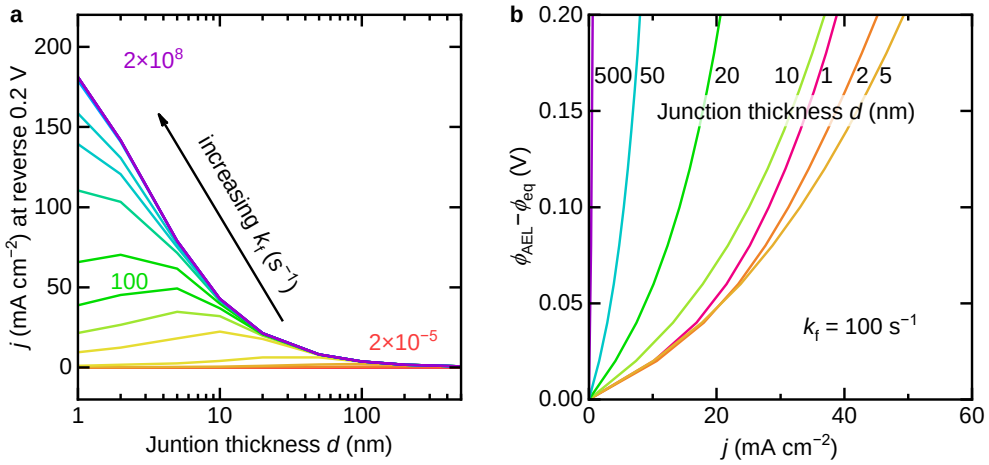

Figure A.4 Steady-state numerical simulated results of BPMs with different junction thickness and WD rate constant using the reported diffusion coefficients for H^+ and OH^- along with the fixed ion concentration in the membranes estimated based on the manufacturer specifications

a, Current density at reverse bias 0.2 V as a function of junction thickness at different WD rate constant in the junction. **b**, Polarization curves in reverse bias of different junction thickness with WD rate constant $k_f = 100$ s^{-1}. See Methods for more information.

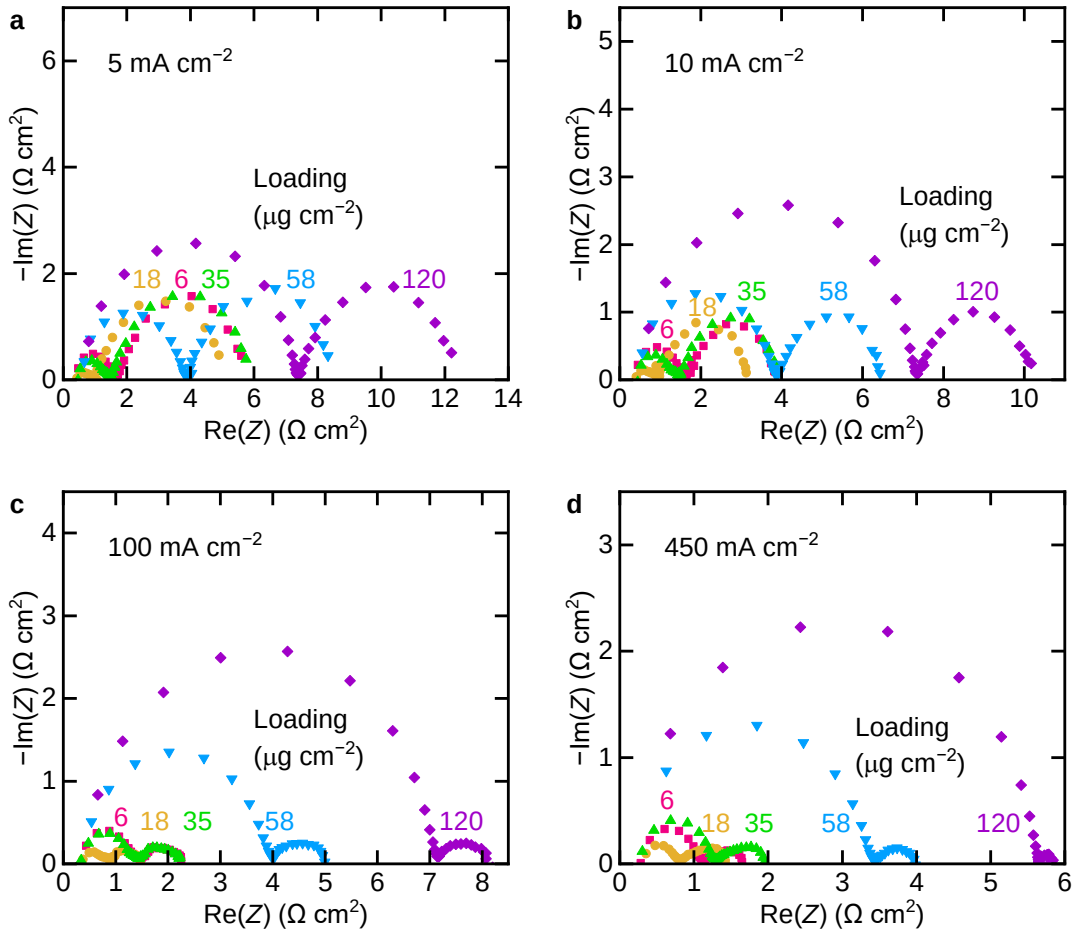

Figure A.5 Nyquist plots of BPM electrolyzers at different current densities with different loadings of TiO_2-P25 WD catalysts deposited by spray coating

The high frequency semicircle is assigned to describe WD, while the low frequency one to describe charge transfer at the anode and cathode. **a**, 5 mA cm^{-2}. **b**, 10 mA cm^{-2}. **c**, 100 mA cm^{-2}. **d**, 450 mA cm^{-2}.

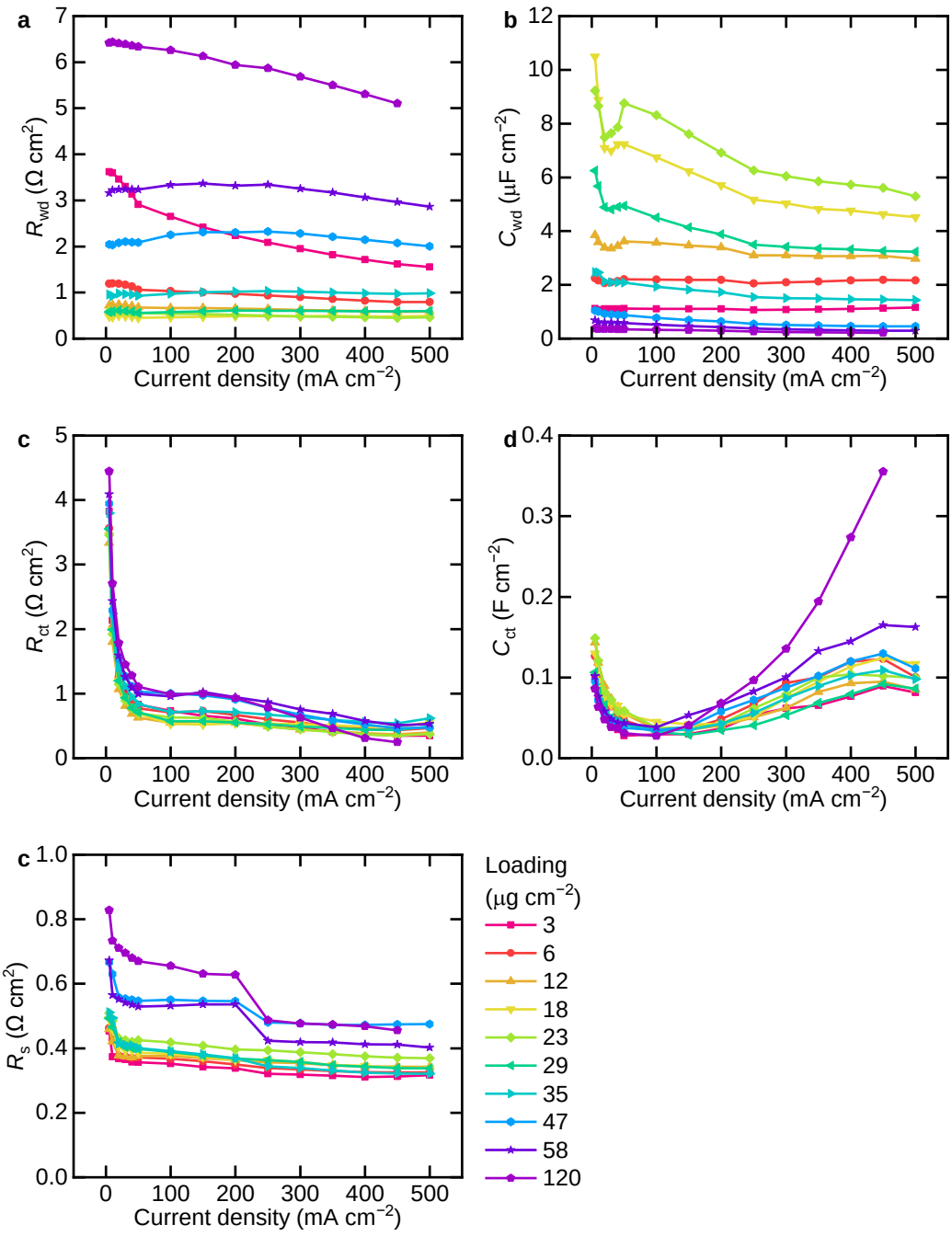

Figure A.6 Impedance fitting results of the BPM electrolyzers with different loadings of TiO_2-P25 WD catalysts deposited by spray coating

a, WD resistance R_{wd}. **b**, WD capacitance C_{wd}. **c**, CT resistance R_{ct}. **d**, CT capacitance C_{ct}. **e**, Series resistance R_s.

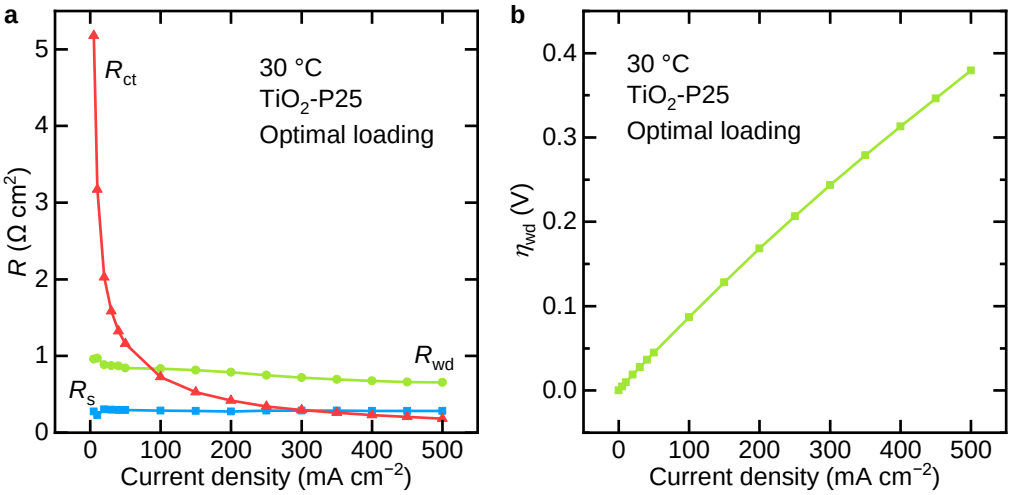

Figure A.7 Impedance analysis and estimation of WD overpotential

a, Impedance fitting results of the BPM electrolyzers with optimal TiO_2-P25 loading (~18 μg cm^{-2} by spin coating) at 30 °C. **b**, Estimated WD overpotential $\eta_{wd} = \int_0^j R_{wd}(j)dj$. The integral form of the total η_{wd} is necessary because the differential WD resistance R_{wd} depends on the voltage/current across the BPM junction. Much like related electrocatalytic processes, the differential resistance increases as driving force η_{wd} for the process increases.

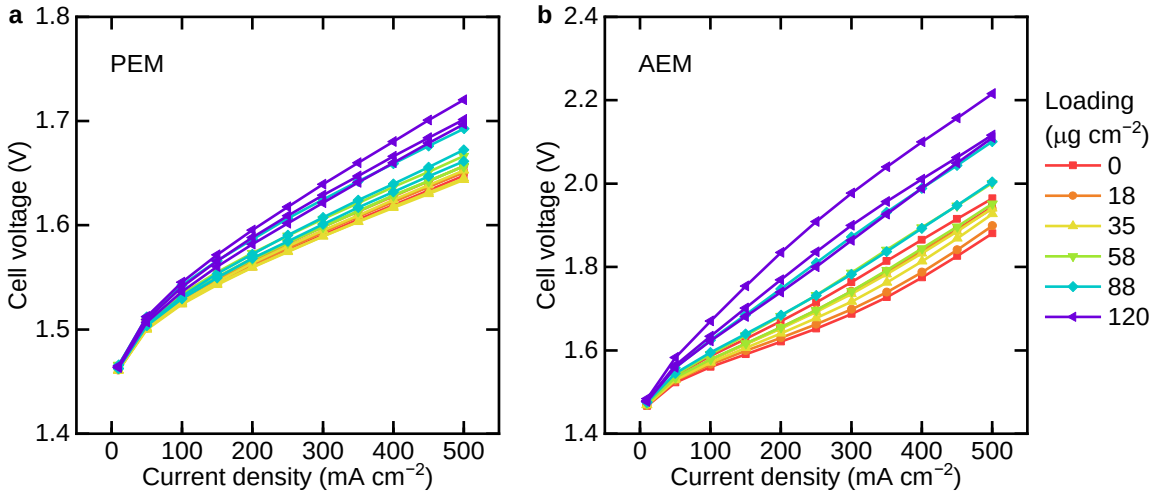

Figure A.8 Performance of PEM and AEM electrolyzers

The TiO_2-P25 layers of different loadings were sandwiched between either two identical PEMs or AEMs. The region from 300 to 500 mA cm^{-2} is fitted to a line obtain the differential resistance. **a**, Polarization curves of PEM electrolyzers. **b**, Polarization curves of AEM electrolyzers.

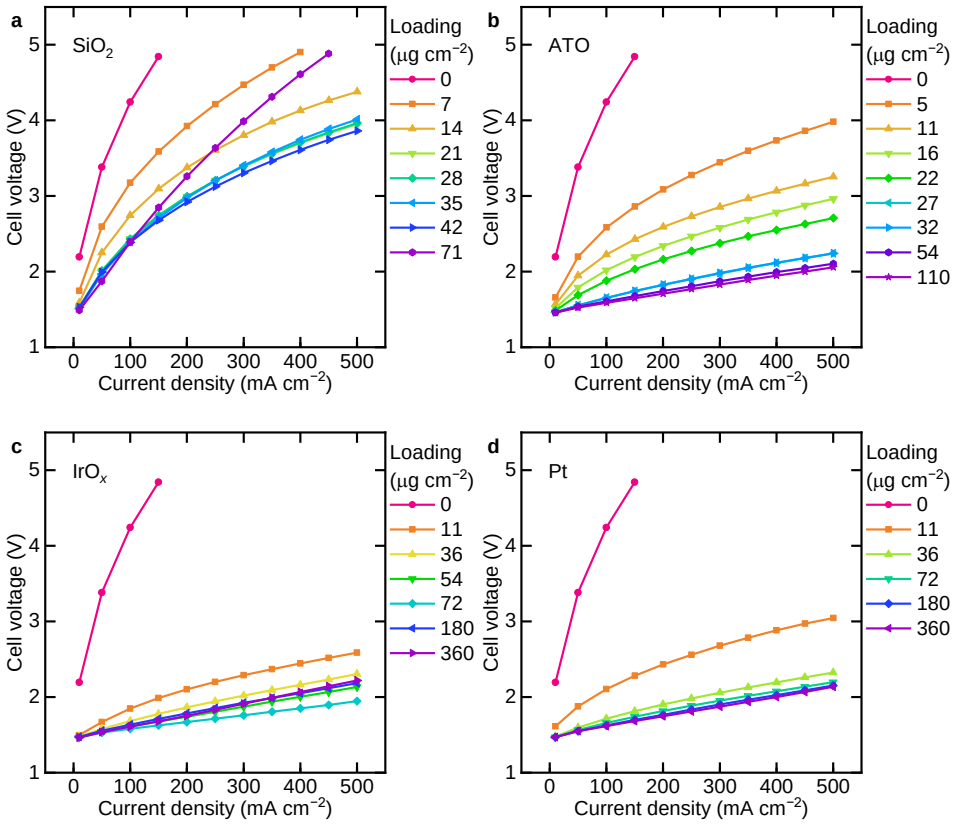

Figure A.9 Performance of BPM electrolyzers with nanoparticles of different electronic conductivity as WD catalysts

Polarization curves of BPM electrolyzers with different loadings of WD catalysts deposited by spray coating. **a**, SiO_2. **b**, Antimony-doped tin oxide (ATO). **c**, IrO_x. **d**. Pt.

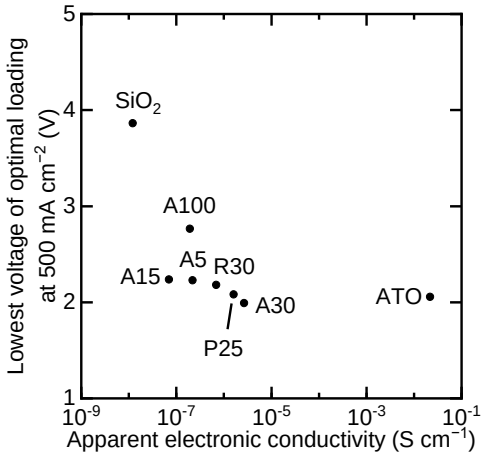

Figure A.10 Relationship between BPM electrolyzer performance and the apparent electronic conductivities of WD catalysts

BPM electrolyzers performance is denoted by the lowest voltage with optimal WD catalyst mass loading at 500 mA cm^{-2}. The apparent electronic conductivities are measured using a simple two-probe setup (and thus includes any relevant contact resistances). For the TiO_2 samples, A = anatase, R = rutile, and the number denotes the size of the nanoparticles (nm) provided by the manufacture. ATO = Sb:SnO_2.

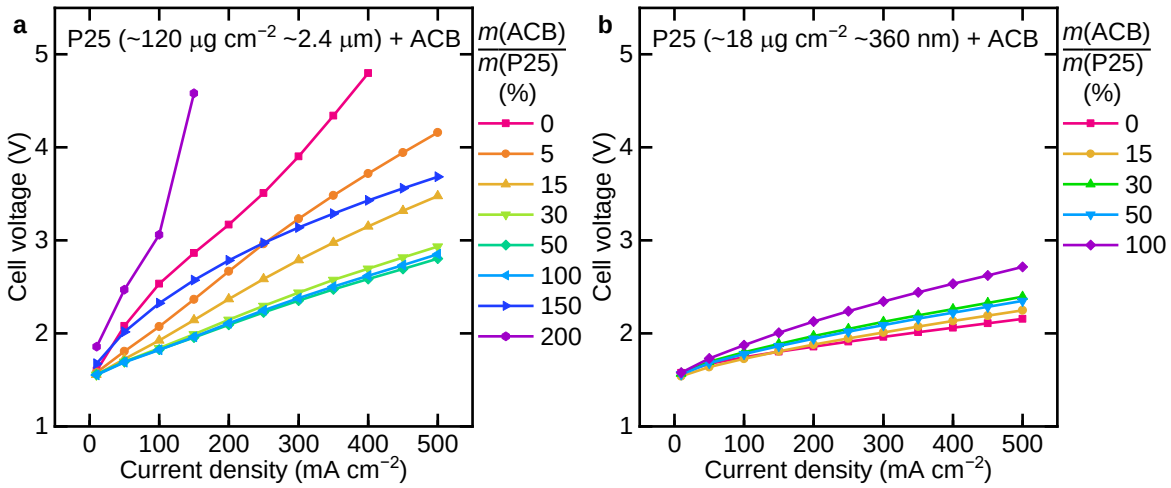

Figure A.11 Performance of BPM electrolyzers with TiO_2-P25 mixed with acetylene carbon black (ACB) as WD catalysts

Polarization curves of BPM electrolyzers with different mass ratio of ACB and TiO_2-P25 deposited by spray coating. **a**, A thick layer of ~120 μg cm^{-2} (~2.4 μm) TiO_2-P25. **b**, A thin layer of TiO_2-P25 at optimal loading ~18 μg cm^{-2} (~360 nm).

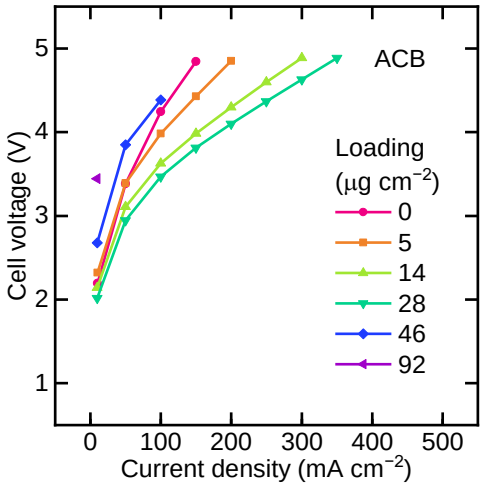

Figure A.12 Performance of BPM electrolyzers with acetylene carbon black (ACB) as WD catalyst

Polarization curves of BPM electrolyzers with different loadings of WD catalysts deposited by spray coating.

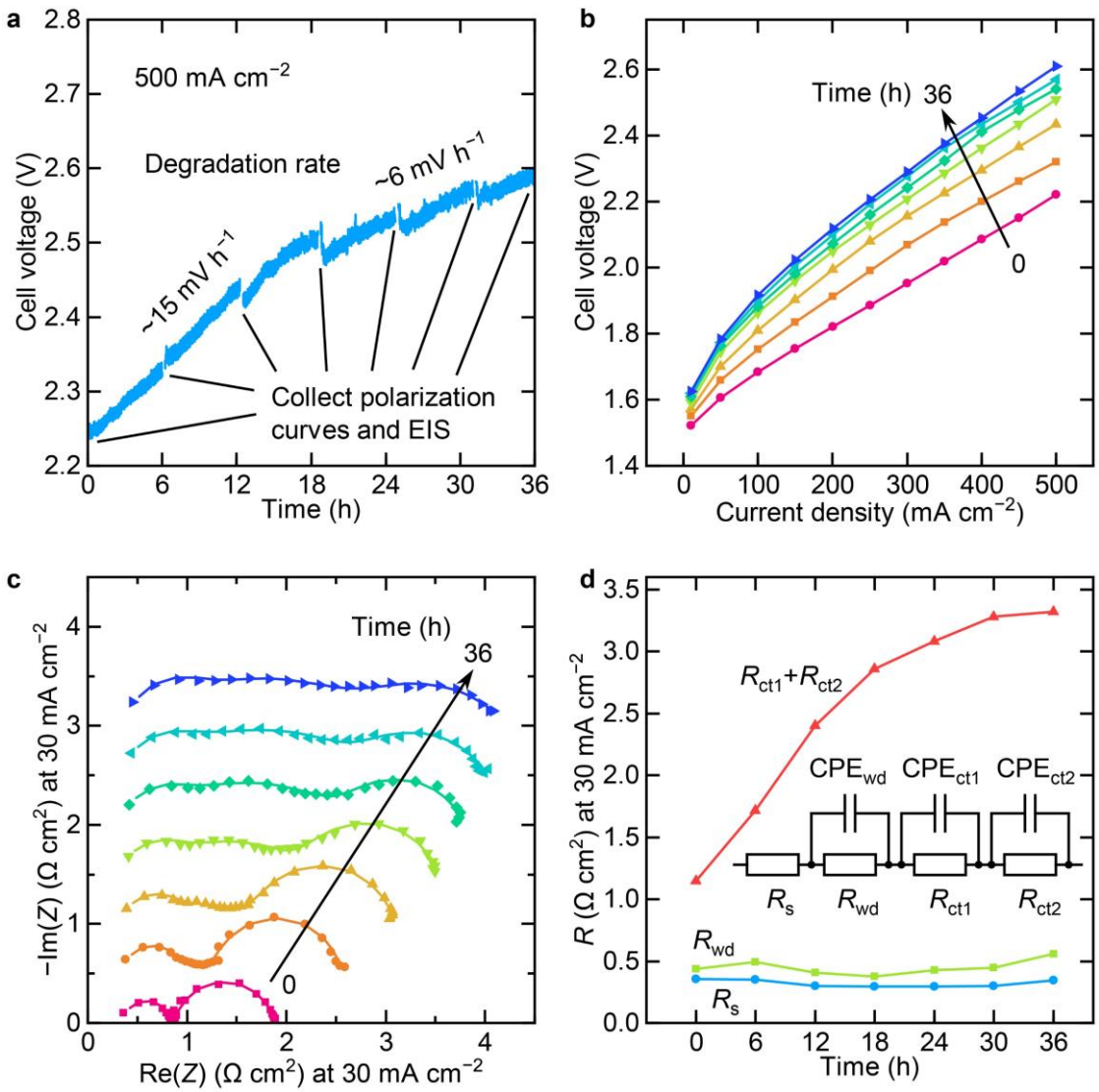

Figure A.13 Stability of the BPM electrolyzer with the best loading (~18 μg cm^{-2}) of TiO$_2$-P25 at 500 mA cm^{-2} and 55 °C

a, Cell voltage at 500 mA cm^{-2} as a function of time. **b**, Polarization curves collected every 6 h. **c**, Nyquist plots collected at 30 mA cm^{-2} every 6 h. Dots are experimental data. Lines are fitted data. Curves are shifted 0.5 unit between datasets vertically for clarity. **d**. Fitted resistances change as a function of time. Inset is the equivalent circuit used to fit the EIS data. CPE = constant phase element. We checked the pH of the recirculating feed water before and after the 36 h stability test using both pH paper and a pH meter. The pH paper shows a pH of 6-7, the pH meter shows a pH of ~6.1, and there is no observable difference between the pH value before and after the stability test.

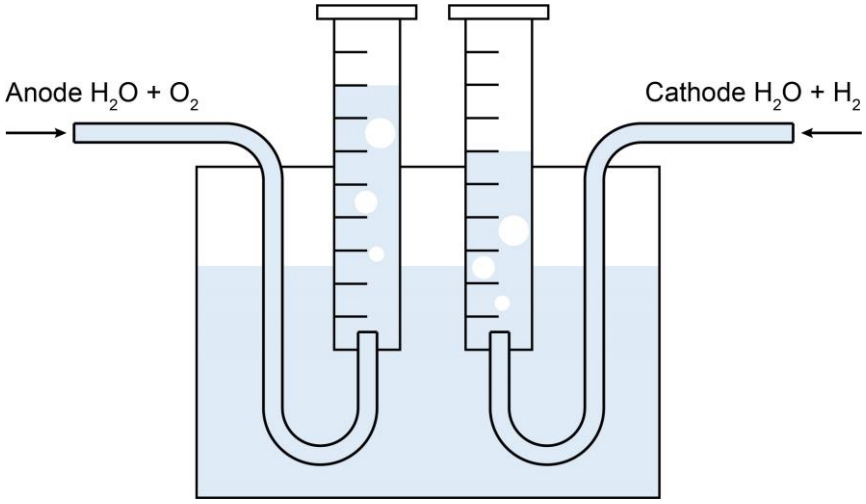

Figure A.14 Schematic diagram of the apparatus to measure gas volume

The total volume of water is ~5.5 L. The volumes of the graduated cylinders are 50 mL for O_2 and 100 mL for H_2. The whole experiment is carried out in air, so the water already contains dissolved O_2 set by the partial pressure of O_2 in air (~0.21 atm). The gas bubbles are generated at the electrodes and carried by the fast water flow (~100 mL min^{-1} for anode and ~60 mL min^{-1} for cathode) to collection in the inverted graduated cylinders. Given the short transit time of between bubble detachment at the electrode and collection in the cylinder (~10 s), little O_2 is apparently lost due to dissolution in the recirculating water.

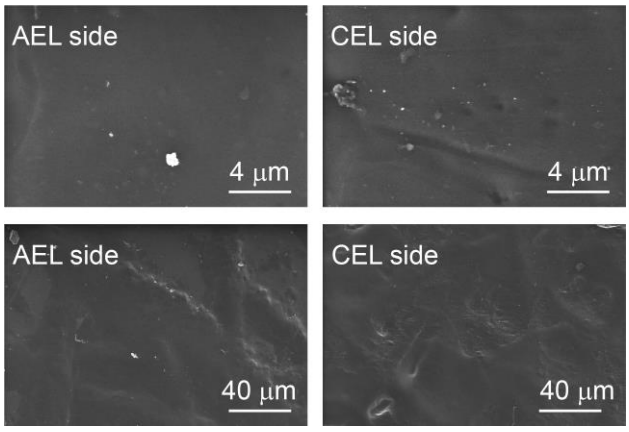

Figure A.15 SEM images of a BPM after testing in the electrolyzer

The uneven morphology is due to the fiber texture of the GDLs and there is no evidence of cracks, pinholes, or other forms of mechanical failure of the ionomer membranes.

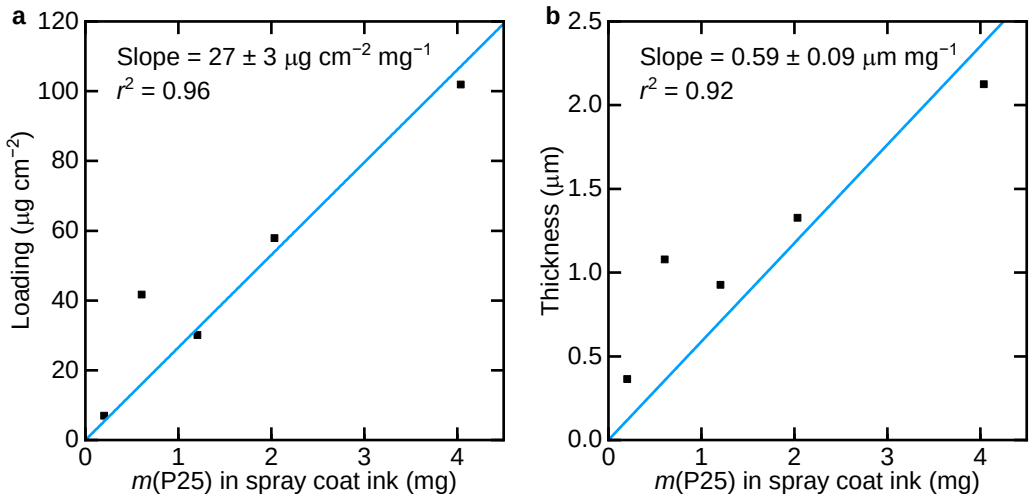

Figure A.16 Quantifying loading and thickness of TiO_2-P25 in BPMs

The linear least squares fit to the calibration data provides the conversion factor used to predict loading and thickness given an amount of ink used and the mass of WD catalyst particles in the ink. This is important because a significant fraction of the ink is lost as overspray and thus does not end up in the BPM.

REFERENCES

1. Giesbrecht, P. K.; Freund, M. S., Recent advances in bipolar membrane design and applications. *Chem. Mater.* **2020,** *32* (19), 8060-8090.

2. Oener, S. Z.; Foster, M. J.; Boettcher, S. W., Accelerating water dissociation in bipolar membranes and for electrocatalysis. *Science* **2020,** *369* (6507), 1099-1103.

3. Wien, M., Über eine Abweichung vom Ohmschen Gesetze bei Elektrolyten. *Ann. Phys.* **1927,** *388* (11), 327-361.

4. Wien, M., Über den Spannungseffekt der Leitfähigkeit bei starken und schwachen Säuren. *Phys. Z.* **1931,** *32*, 545-547.

5. Schiele, J., Über den Spannungseffekt der Leitfähigkeit bei starken und schwachen Säuren. *Ann. Phys.* **1932,** *405* (7), 811-830.

6. Eckstrom, H. C.; Schmelzer, C., The Wien effect: Deviations of electrolytic solutions from Ohm's law under high field strengths. *Chem. Rev.* **1939,** *24* (3), 367-414.

7. Onsager, L., Deviations from ohm's law in weak electrolytes. *J. Chem. Phys.* **1934,** *2* (9), 599-615.

8. Chen, Y.; Martínez, R. J.; Gervasio, D.; Baygents, J. C.; Farrell, J., Water splitting promoted by electronically conducting interlayer material in bipolar membranes. *J. Appl. Electrochem.* **2020,** *50* (1), 33-40.

9. Lindquist, G. A.; Oener, S. Z.; Krivina, R.; Motz, A. R.; Keane, A.; Capuano, C.; Ayers, K. E.; Boettcher, S. W., Performance and durability of pure-water-fed anion exchange membrane electrolyzers using baseline materials and operation. *ACS Appl. Mater. Interfaces* **2021,** *13* (44), 51917-51924.

APPENDIX B

CHAPTER III SUPPLEMENTAL INFORMATION

Supporting Figures

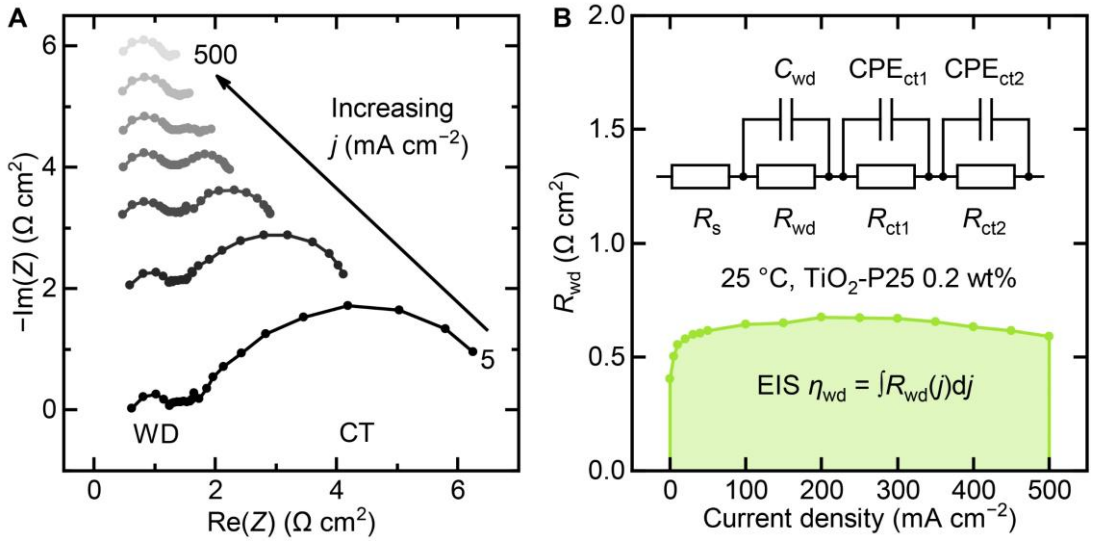

Figure B.1 Measured WD overpotential η_{wd} using electrochemical impedance spectroscopy (EIS)

(A) Nyquist plots of the total cell at different current densities. The imaginary parts are shifted to make the comparison clearer. The high-frequency semicircle is related to water dissociation (WD) while low frequency semicircles are related to charge transfer (CT) at the electrodes. **(B)** Fitting the EIS data with appropriate equivalent circuits enables the extraction of R_{wd} as a function of j. The inset shows the equivalent circuit used for this sample. Integrating R_{wd} with j results in $\eta_{wd} = \int_0^j R_{wd}(j)\mathrm{d}j$, which is the area under the $R_{wd}(j)$ curve.

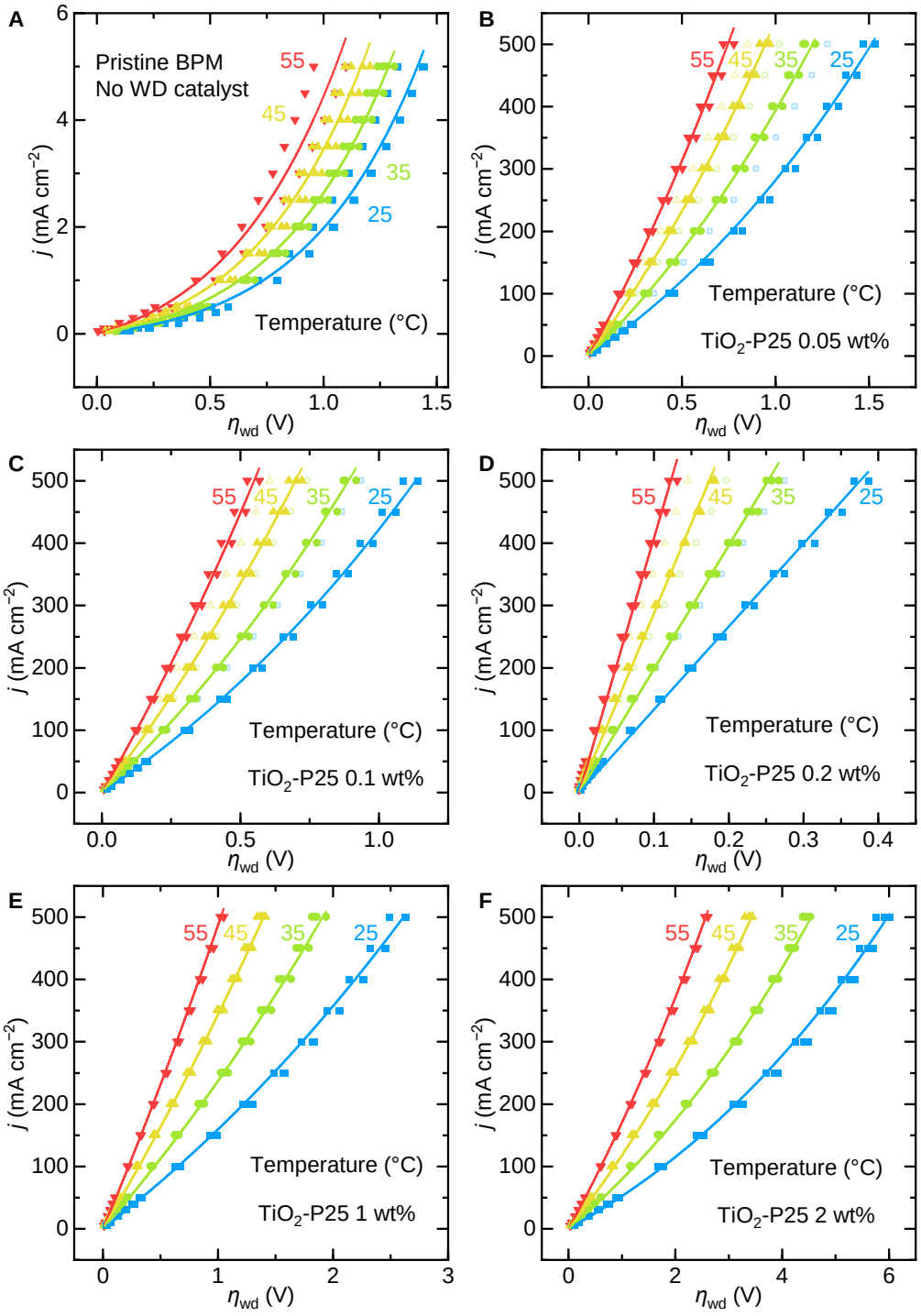

Figure B.2 Temperature-dependent WD polarization curves for BPMs with different loadings of TiO_2-P25 as WD catalyst

Dots are experimental data during temperature cycling. Lines are the fitting results to the BPM equation using the solid dots data. Hollow pale dots are excluded because they are not repeatable during temperature cycling. **(A)** Pristine BPM without WD catalyst. **(B)** 0.05 wt%. **(C)** 0.1 wt%. **(D)** 0.2 wt%. **(E)** 1 wt%. **(F)** 2 wt%.

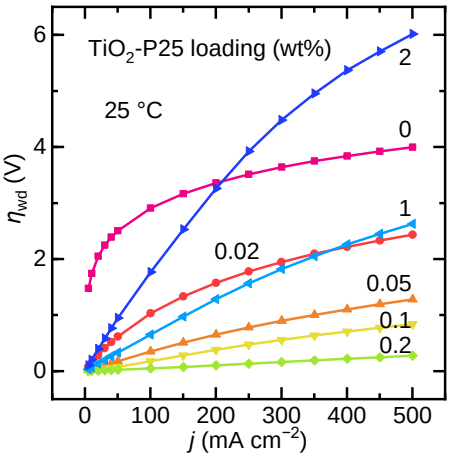

Figure B.3 Polarization curves of BPMs with different mass loadings of TiO_2-P25 WD catalyst at 25 °C

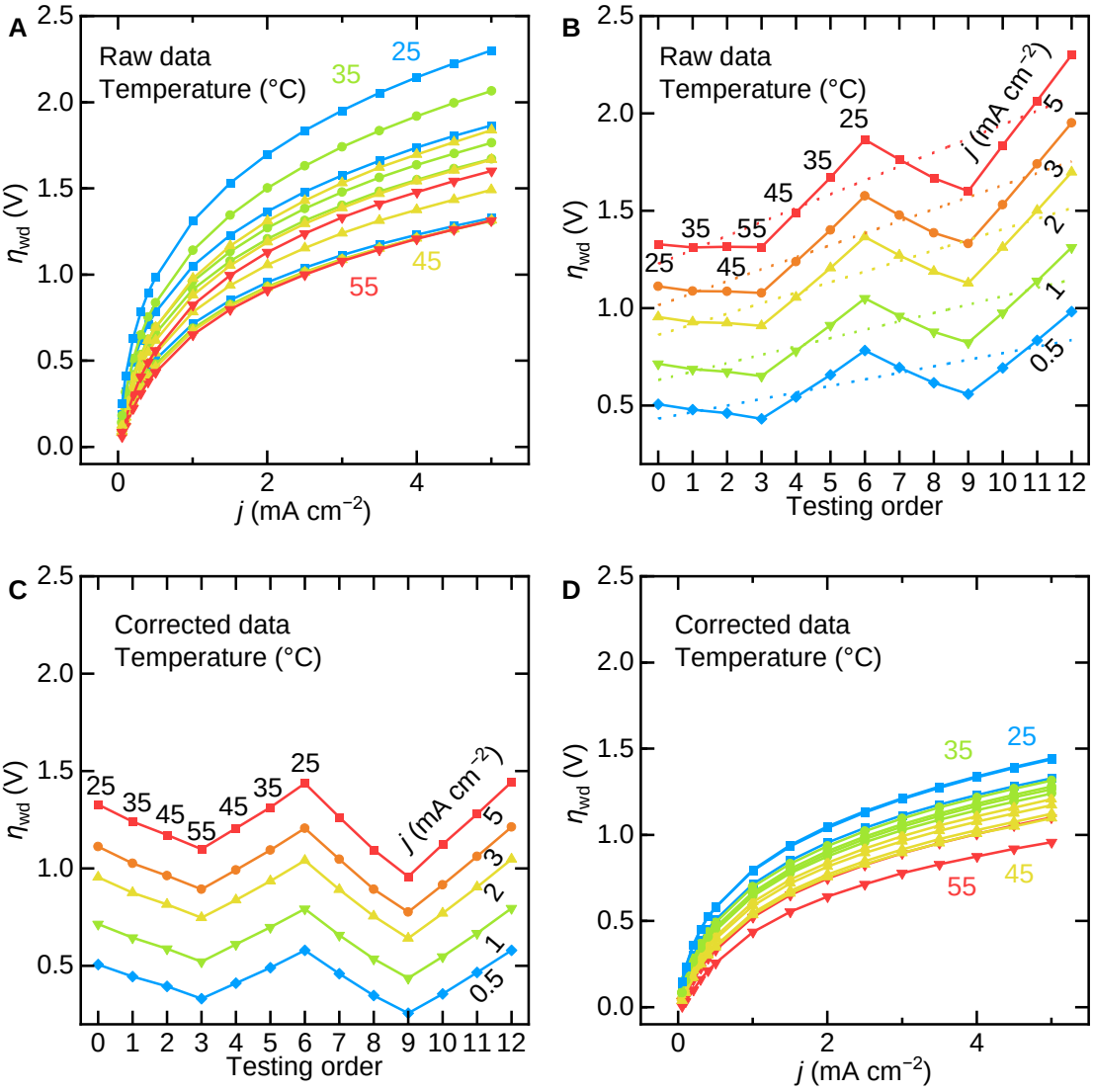

Figure B.4 Correction of degradation over time for a pristine, uncatalyzed BPM

The cell is tested at 0 to 5 mA cm^{-2} to reduce the effect of degradation over time. **(A)** Polarization curves of the raw data. The temperature dependence is obscured by the degradation during the temperature cycling over time. **(B)** Raw data of η_{wd} as a function of testing order, *i.e.*, time, at different j. A least-square linear fitting is used for each j to extract the degradation rate. **(C)** Corrected data showing η_{wd} as a function of testing order, *i.e.*, time, at different j, after subtracting the degradation. **(D)** Polarization curves of the corrected data after subtracting the degradation. The temperature dependence is clearer.

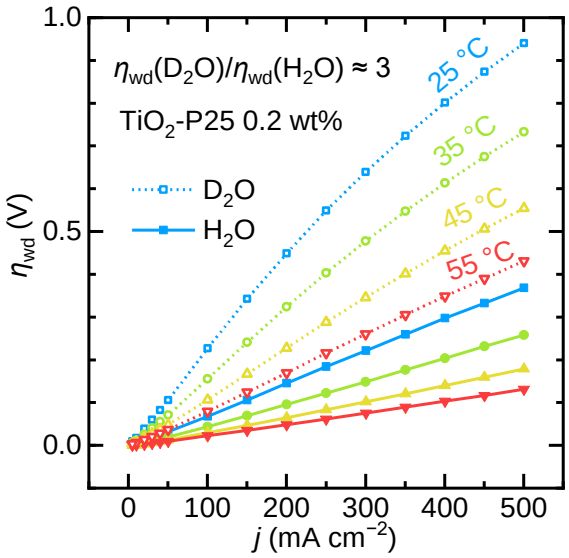

Figure B.5 Kinetic isotope effect. 0.2 wt% TiO_2-P25 is used as WD catalyst

The electrolyzer is fed by either H_2O or D_2O.

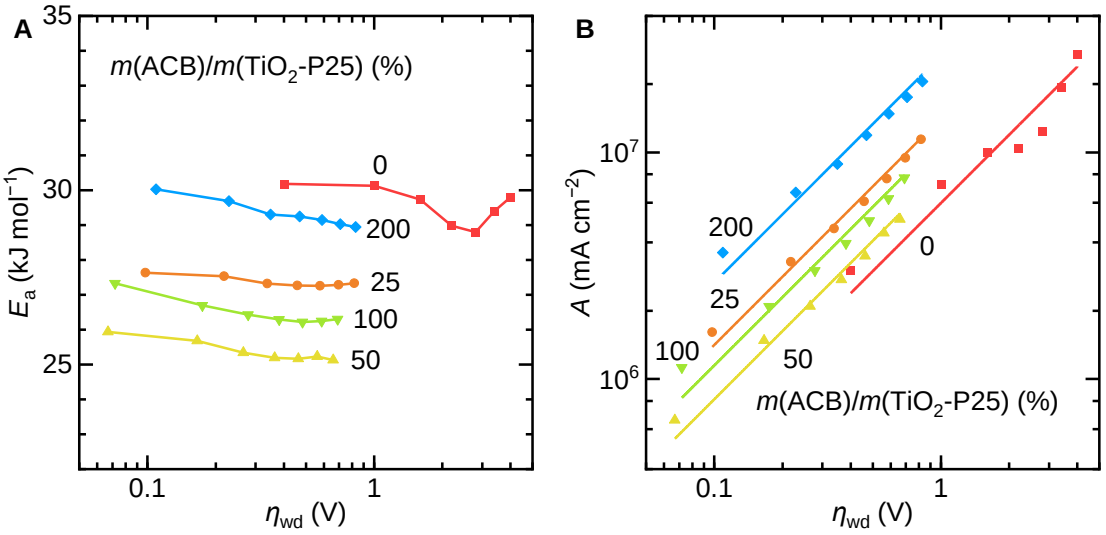

Figure B.6 Arrhenius analysis of the temperature-dependent polarization curves of BPMs with different mass ratio of ACB and TiO_2-P25

(A) Apparent activation energy E_a as a function of η_{wd}. Notice the log scale on the horizontal axis. **(B)** Pre-exponential factor A as a function of η_{wd}. Notice the log scale on both axes. Lines are least-squares linear fits with a fixed slope of one.

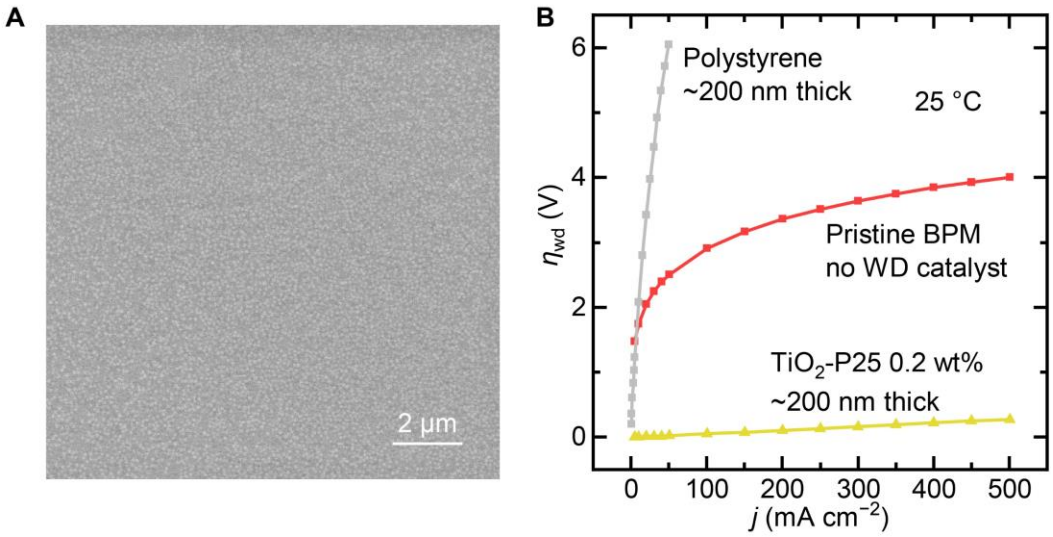

Figure B.7 Comparison of BPM response with catalytic TiO_2 layers and non-catalytic polystyrene nanospheres

The scale bar represents 2 µm. **(A)** Scanning electron microscope (SEM) image of polystyrene beads (non-functionalized, diameter 100 nm) spin-coated on the CEL. There are about two layers of polystyrene beads, making the total thickness ~200 nm. **(B)** Polarization curves of polystyrene, pristine BPM, and TiO_2-P25 at optimal loading (~200 nm). This data shows that at equivalent spacing using a non-catalytic interfacial layer in the BPM, the WD kinetics are very slow.

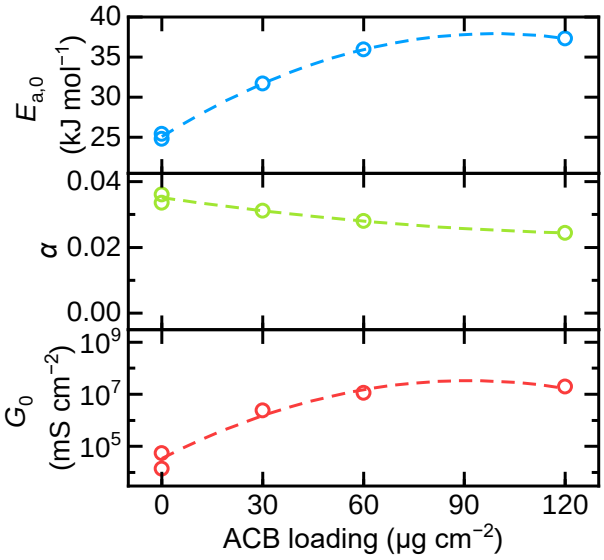

Figure B.8 Temperature-dependence analysis using the semi-empirical BPM equation for BPMs with different loadings of ACB

Lines serve as a guide for the eye.

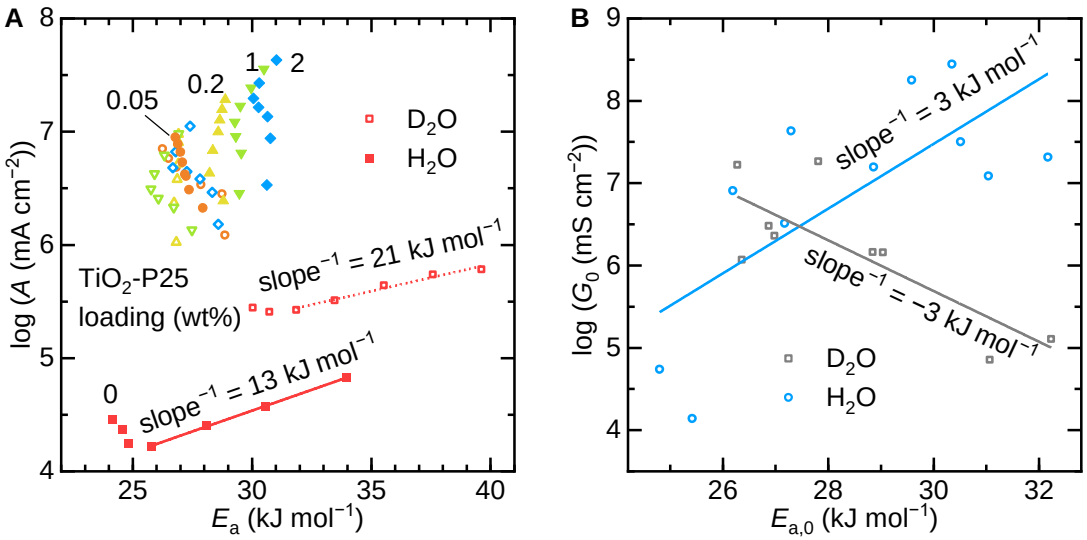

Figure B.9 Compensation effect check. Lines are least-squares linear fits

(A) log A (pre-exponential factor) as a function of E_a (apparent activation energy). **(B)** log G_0 (proton-transfer conductance) as a function of $E_{a,0}$ (equilibrium activation energy). At lower η_{wd}, log A increases linearly with E_a – in H_2O, A increases 10 times when E_a increases 13 kJ mol^{-1} ($R^2 = 0.999$), and in D_2O, A increases 10 times when E_a increases 21 kJ mol^{-1} ($R^2 = 0.975$), both are much larger than the 5.6 kJ mol^{-1} for HER in alkaline condition. Using $E_{a,0}$ and G_0 to analyze the data, there is a very weak correlation ($R^2 = 0.52$ for H_2O and 0.64 for D_2O).

Supplemental Experimental Procedures

Schematic diagram of the membrane electrode assembly (MEA).

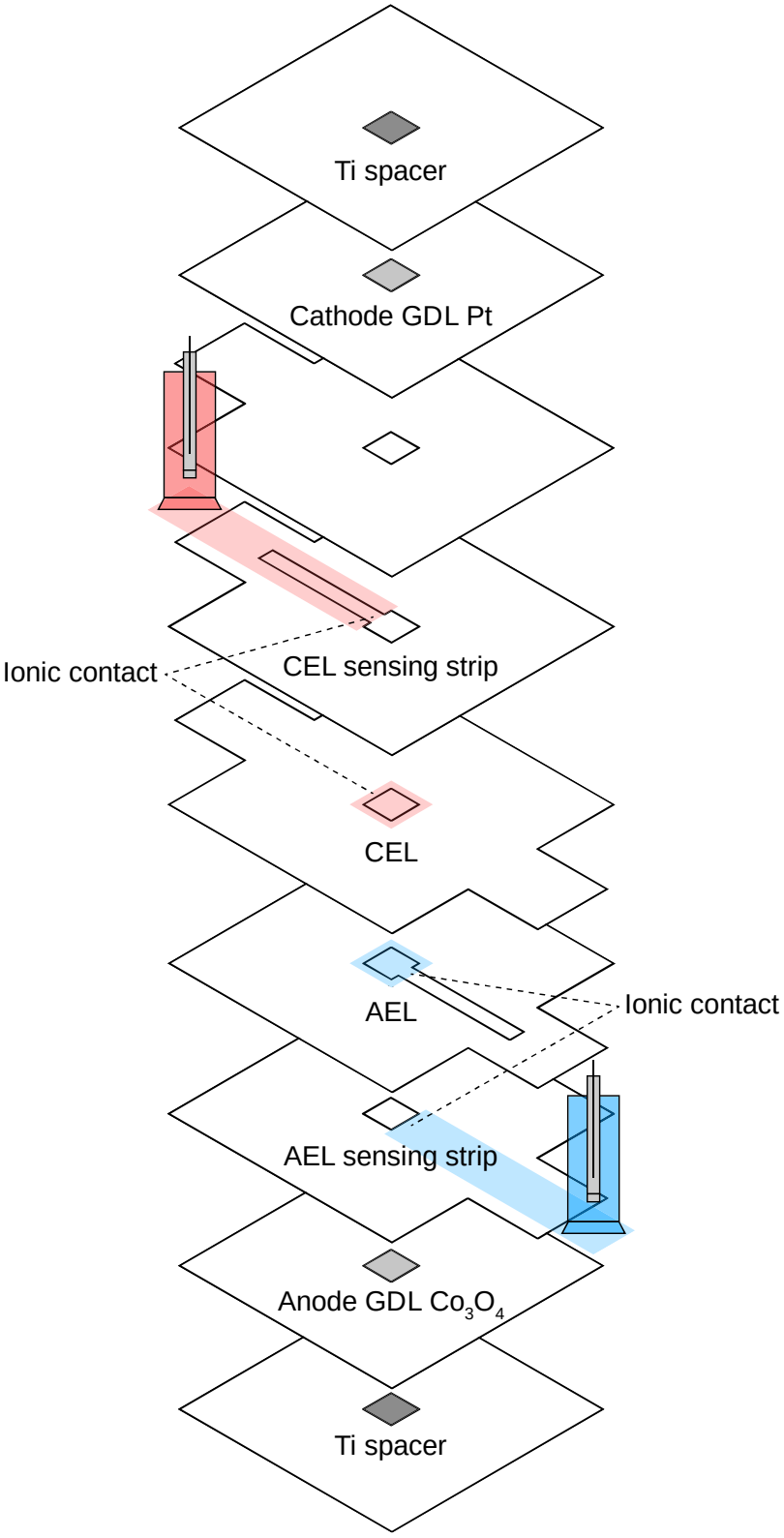

Place the anode flow field (homemade stainless-steel), supporting materials, and rubber pads in place for later use.

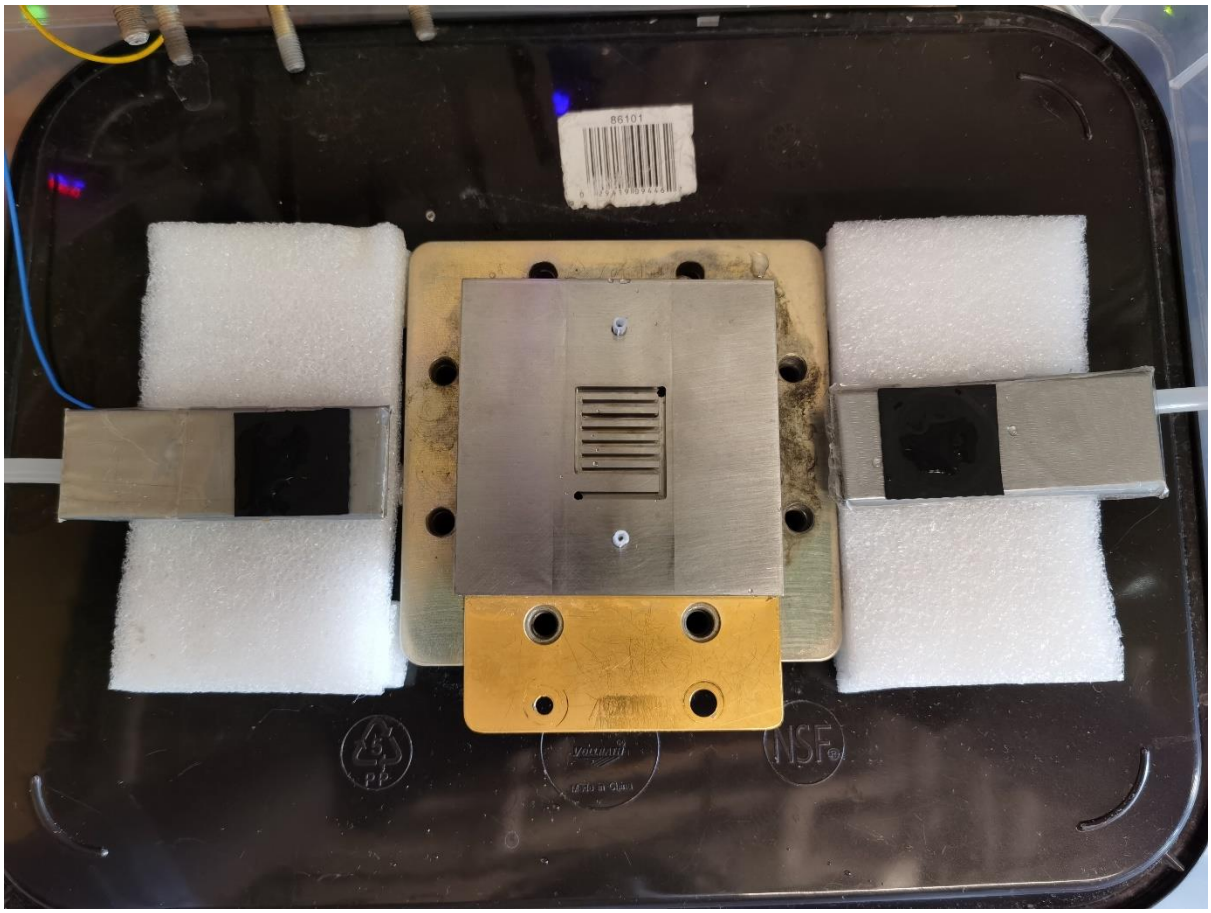

Place several gaskets (active area of 1.0 cm × 1.0 cm) of a total thickness of 0.035″ on top of the anode flow field.

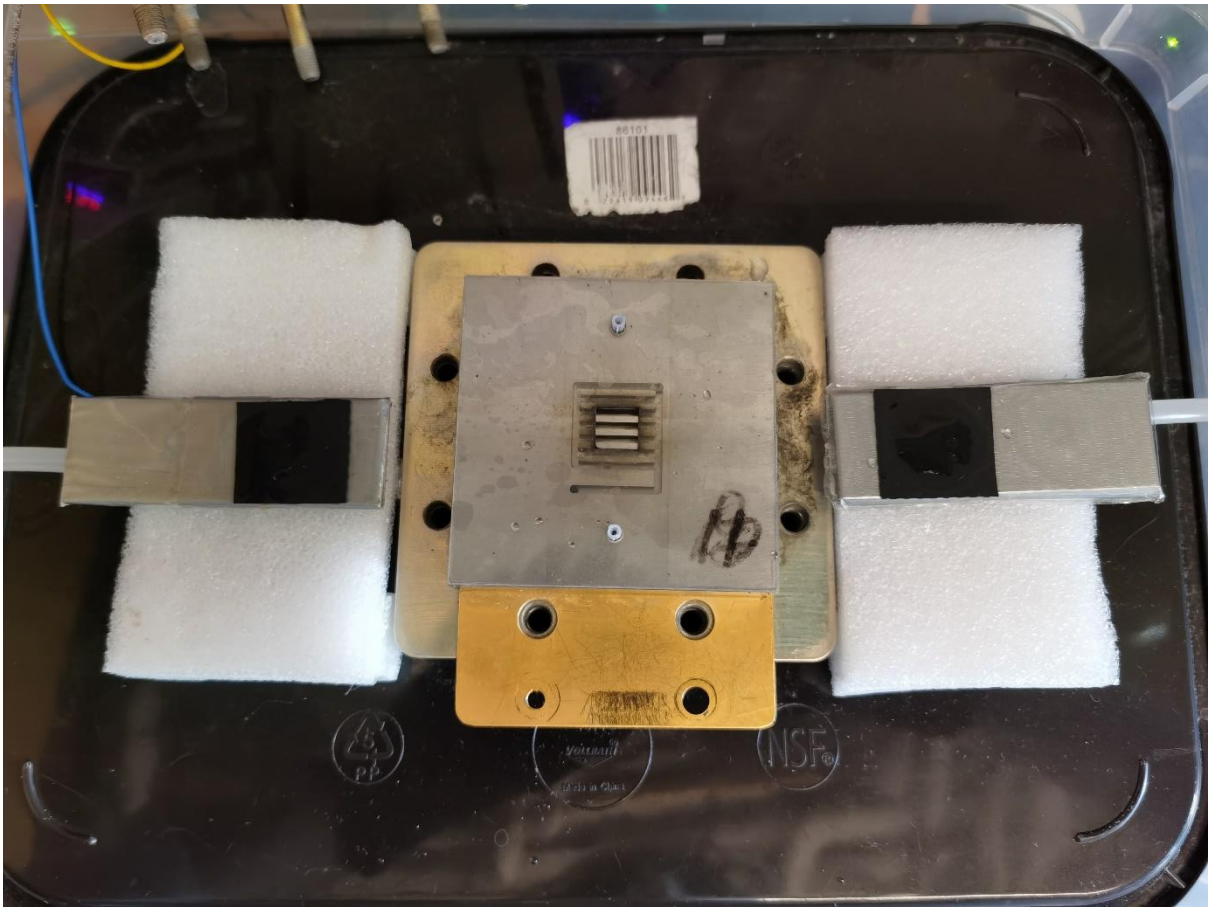

Install one Ti spacer (sintered Ti frits electroplated with 1 μm Pt, 1 cm × 1 cm, Baoji Yinggao Metal Materials Co., Ltd.) in the active region.

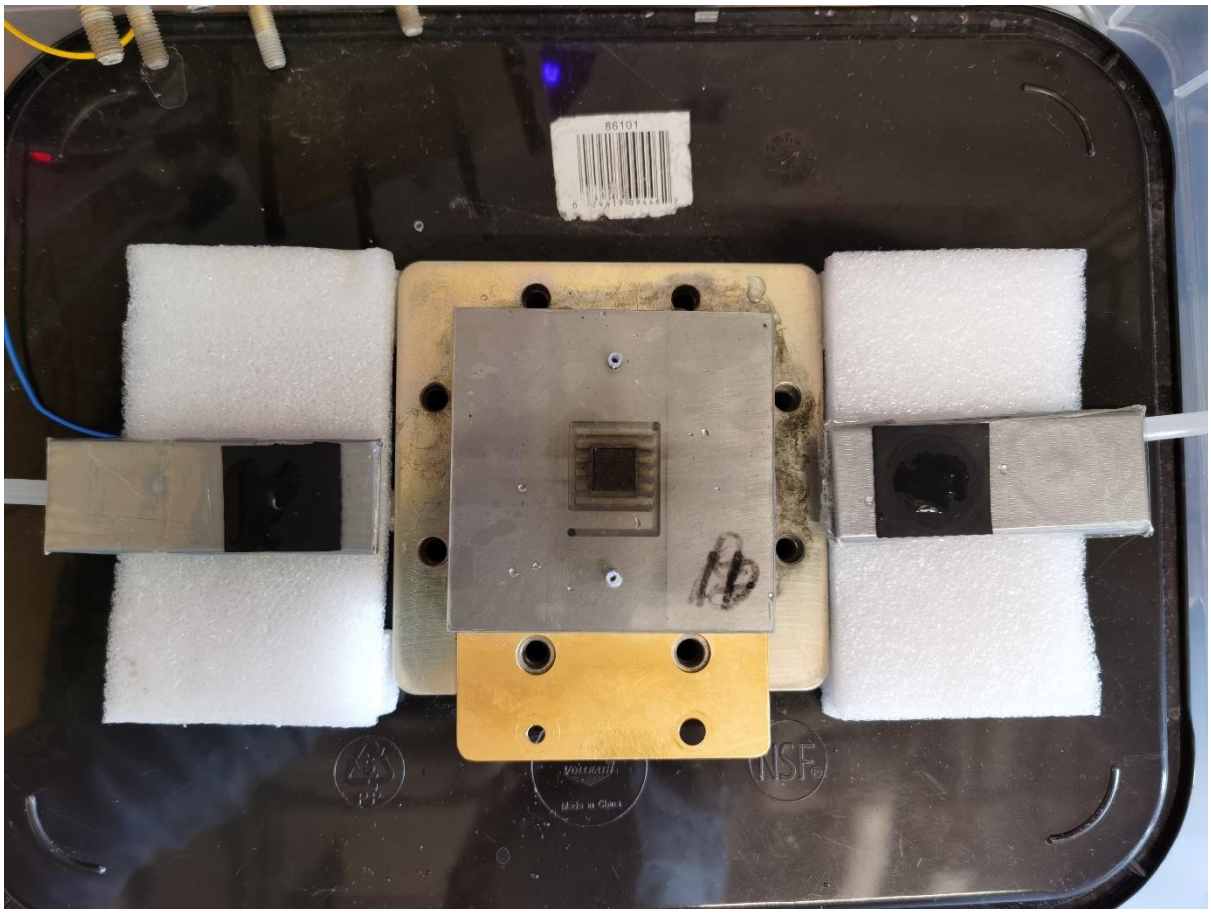

Install one anode GDL (Co_3O_4 facing up) in the active region.

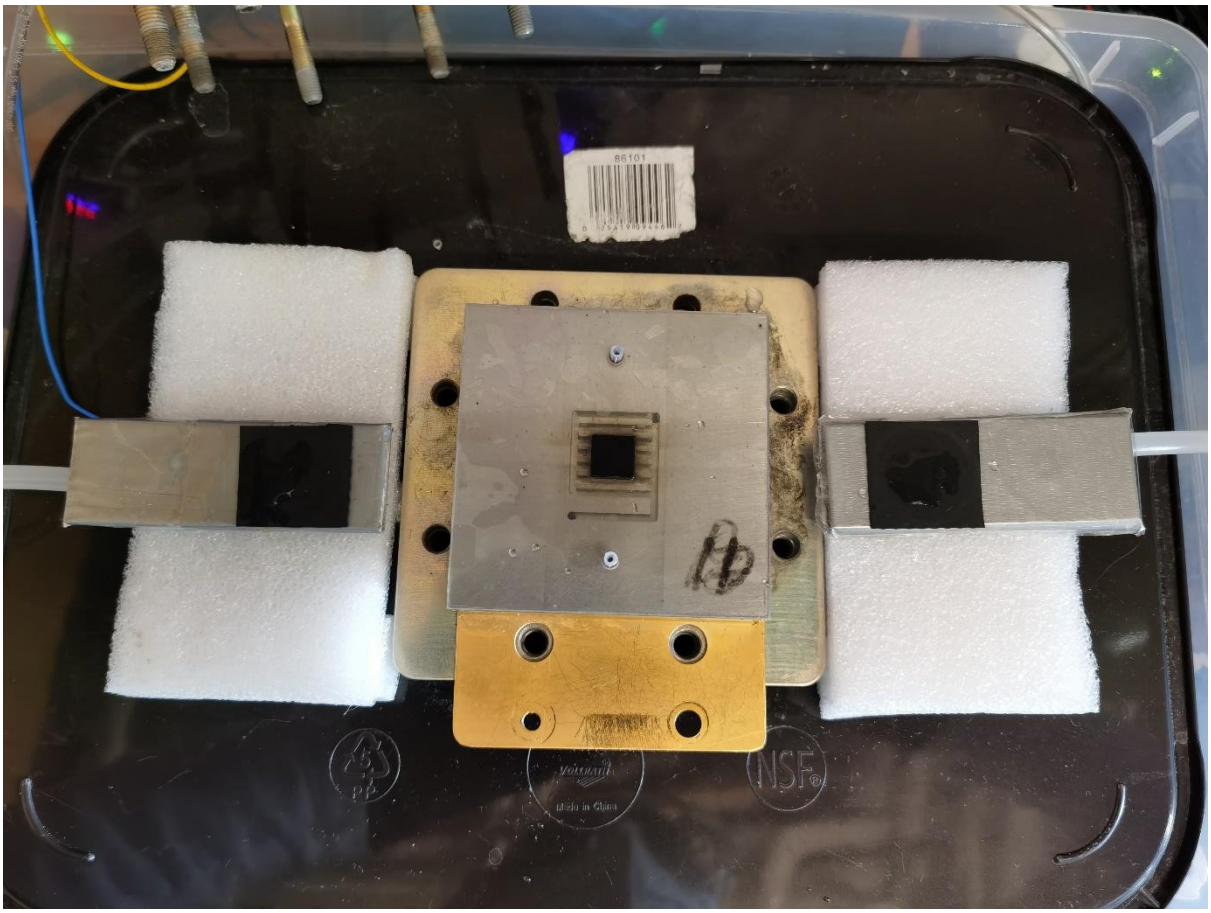

Install an extended 0.005″gasket to support the AEL sensing strip.

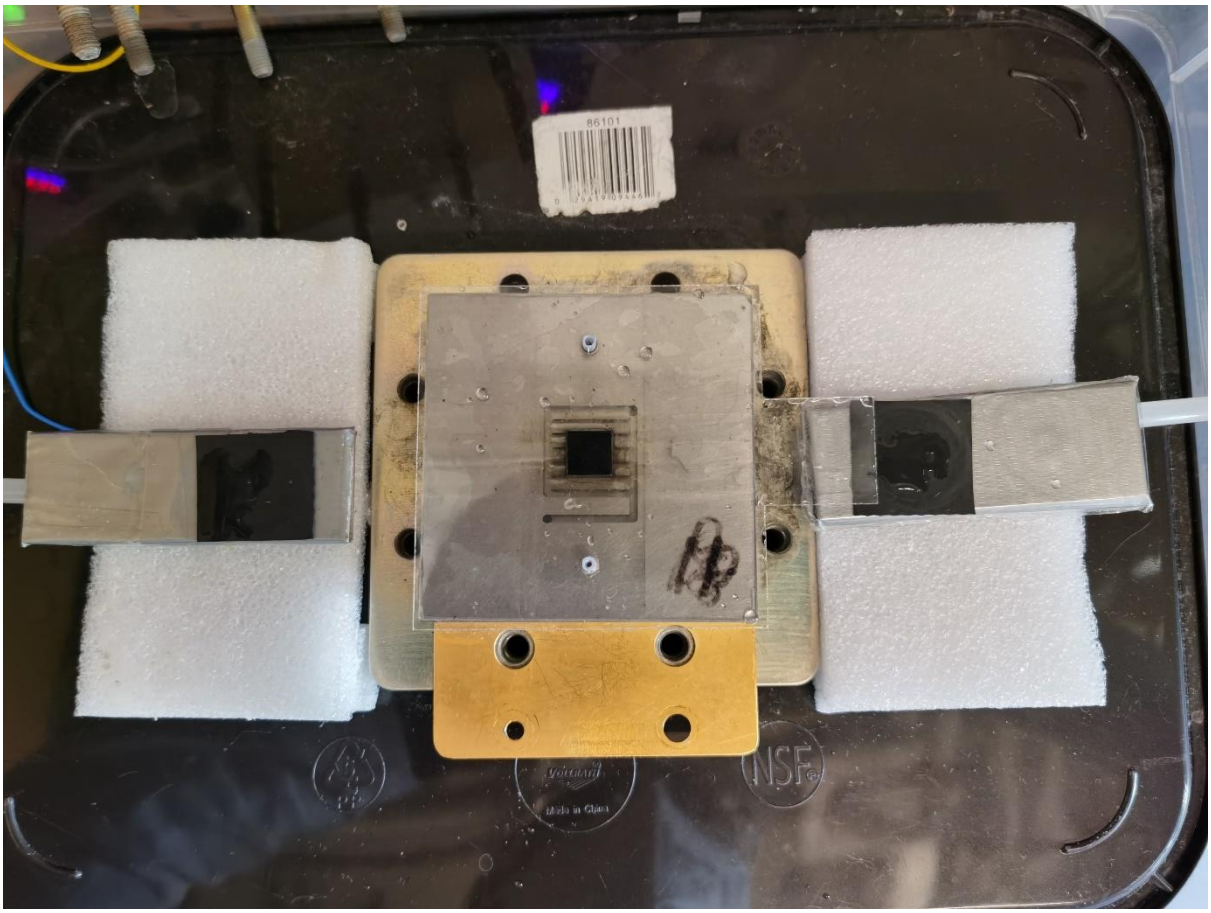

The AEL sensing strip is placed with one end aligned with the edge of the square active region of the gasket.

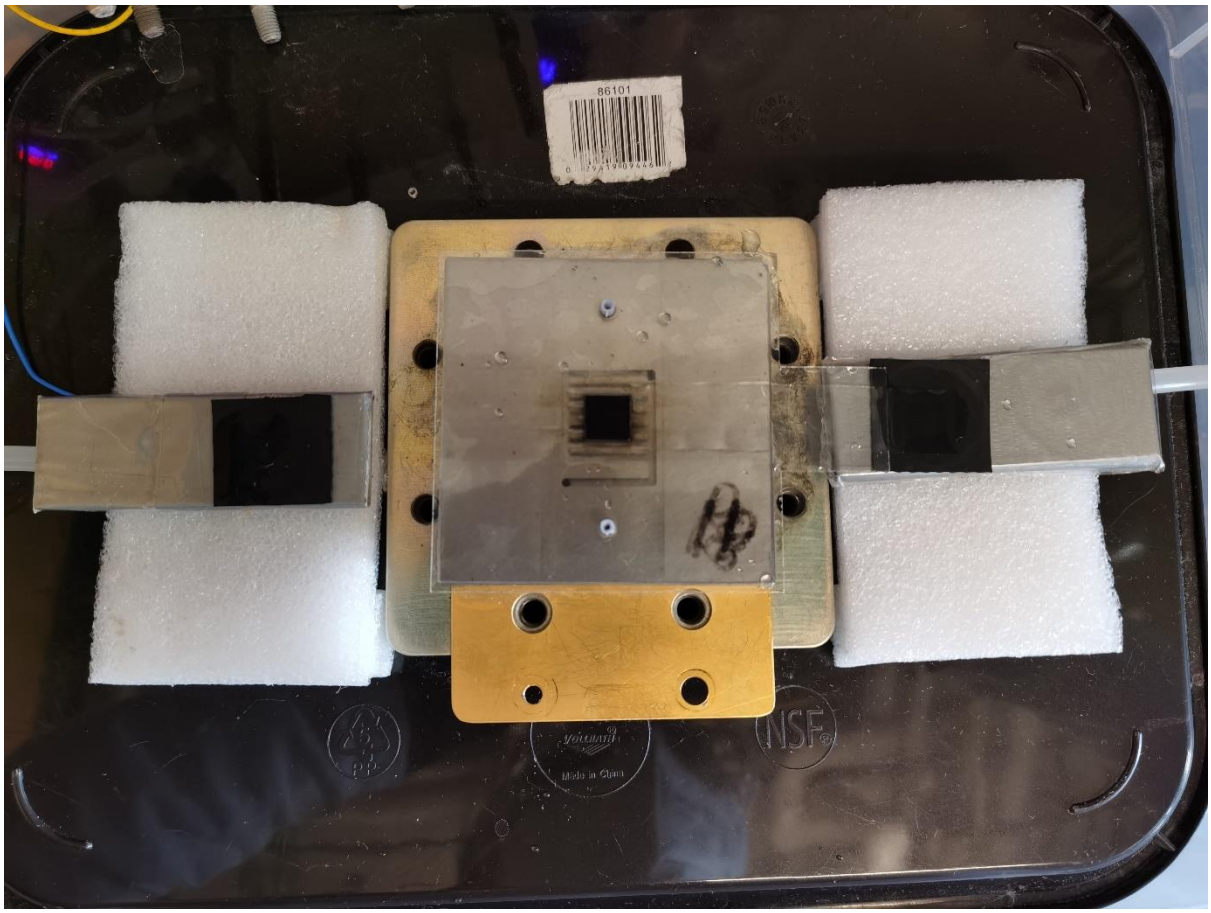

A closer view of the AEL sensing strip.

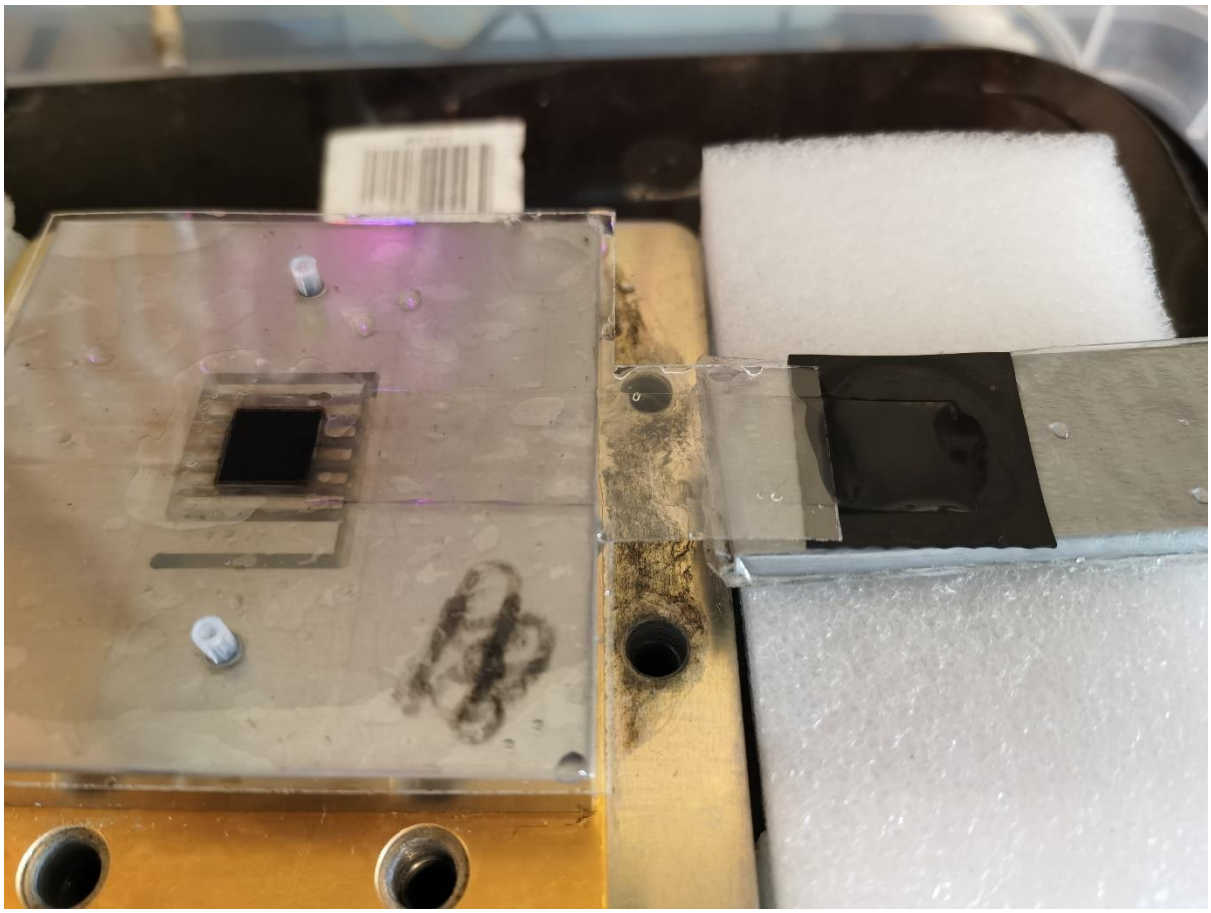

Add an extended 0.002″ gasket with an open “track” to prevent the membrane sensing strip from drying.

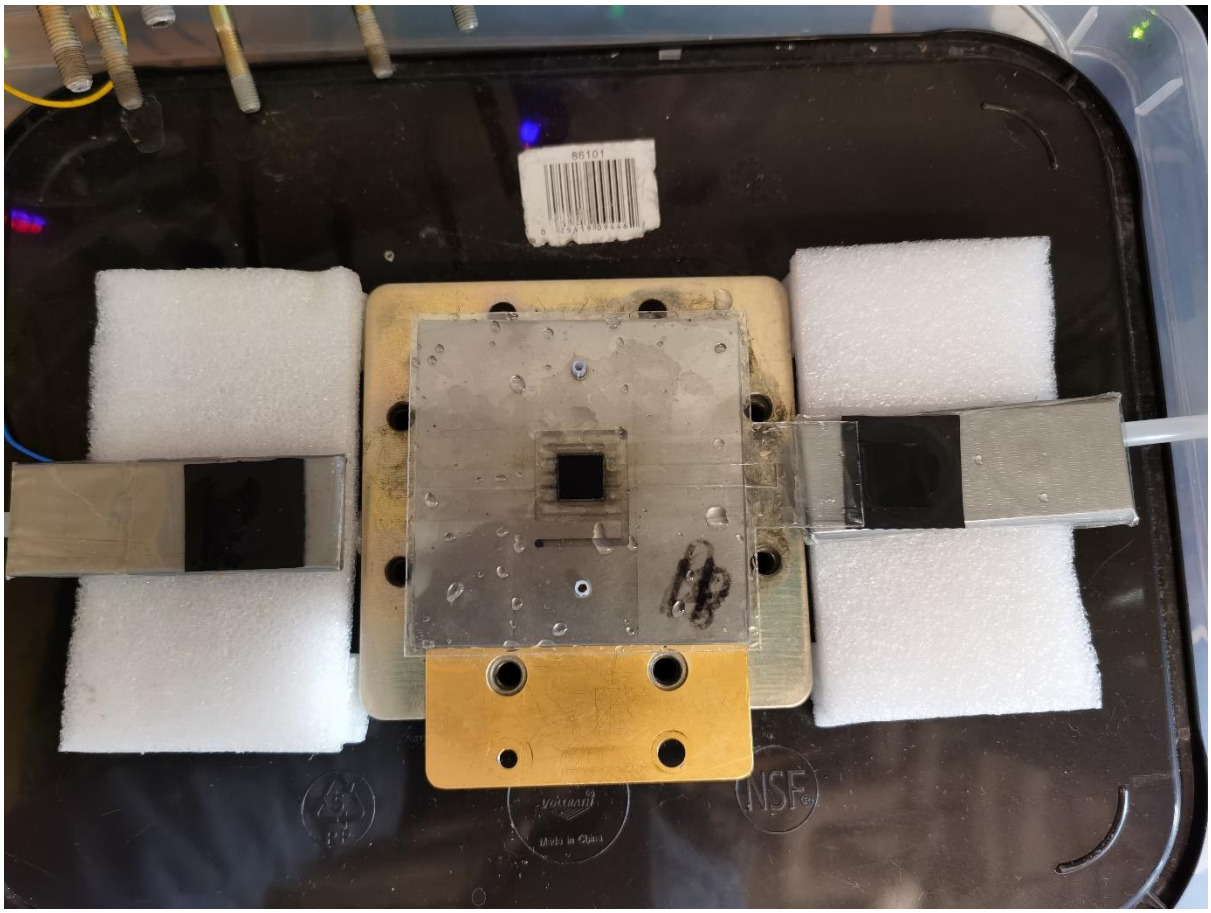

A closer view of the open “track”.

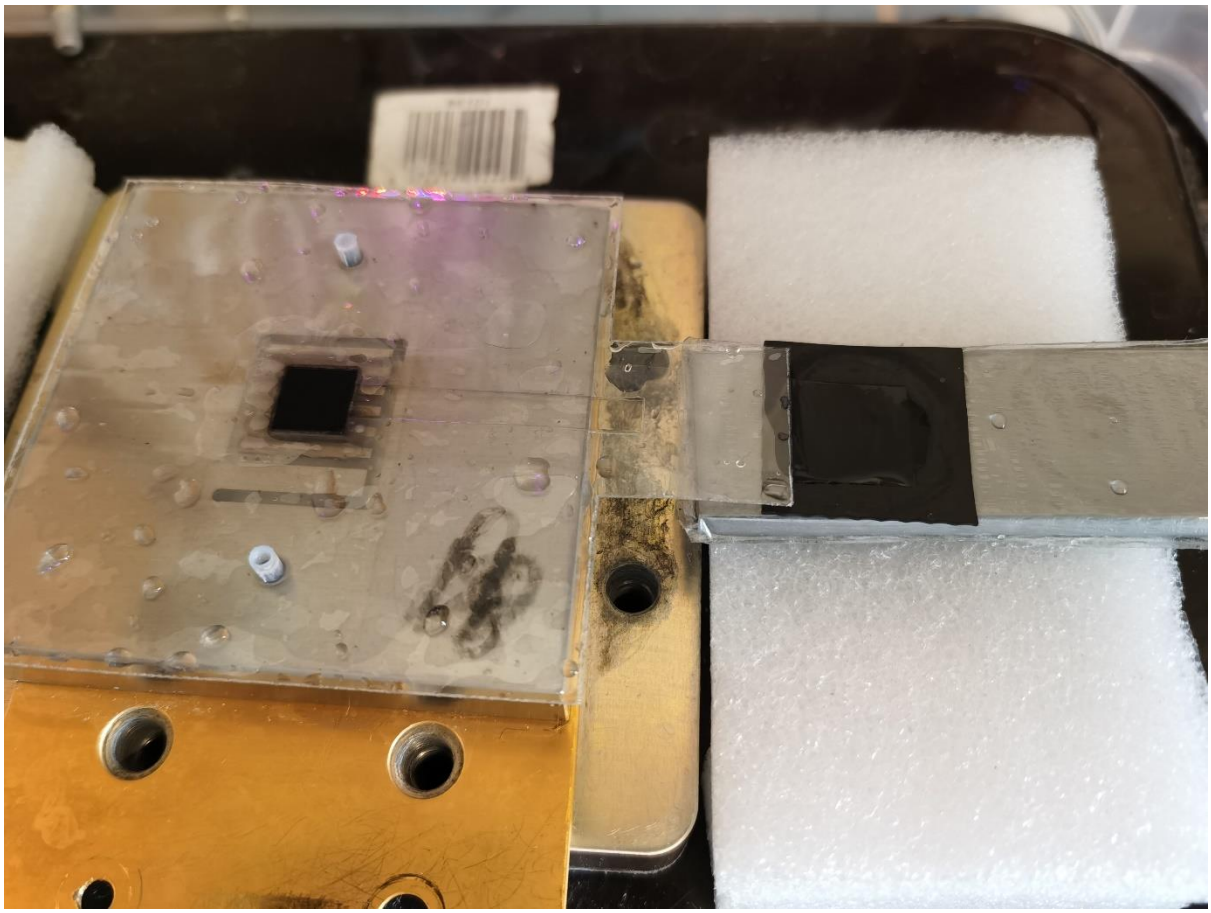

The AEL is placed on top of the anode GDL and touches the AEL sensing strip outside the active region.

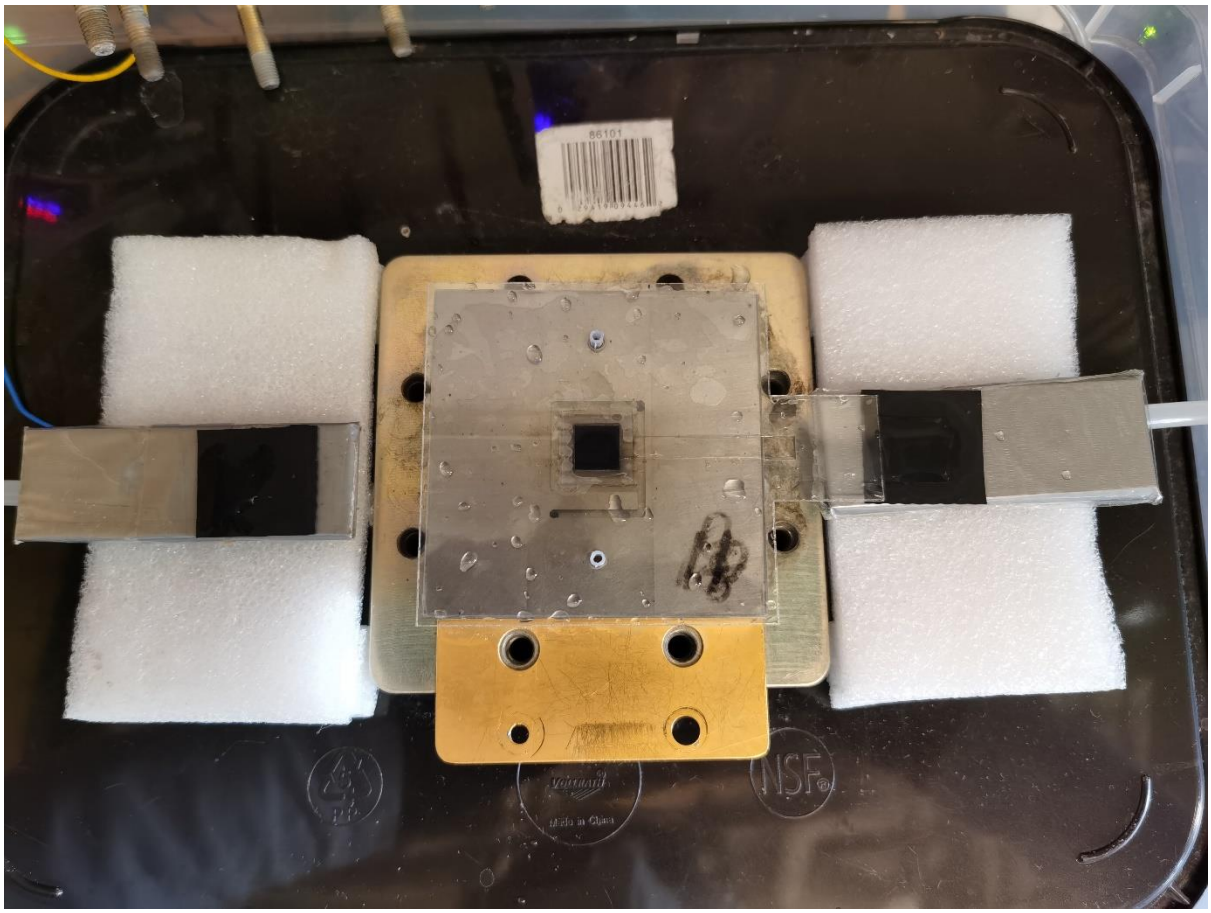

A closer view of the AEL and the AEL sensing strip. Notice the ionic contact region is outside the active region.

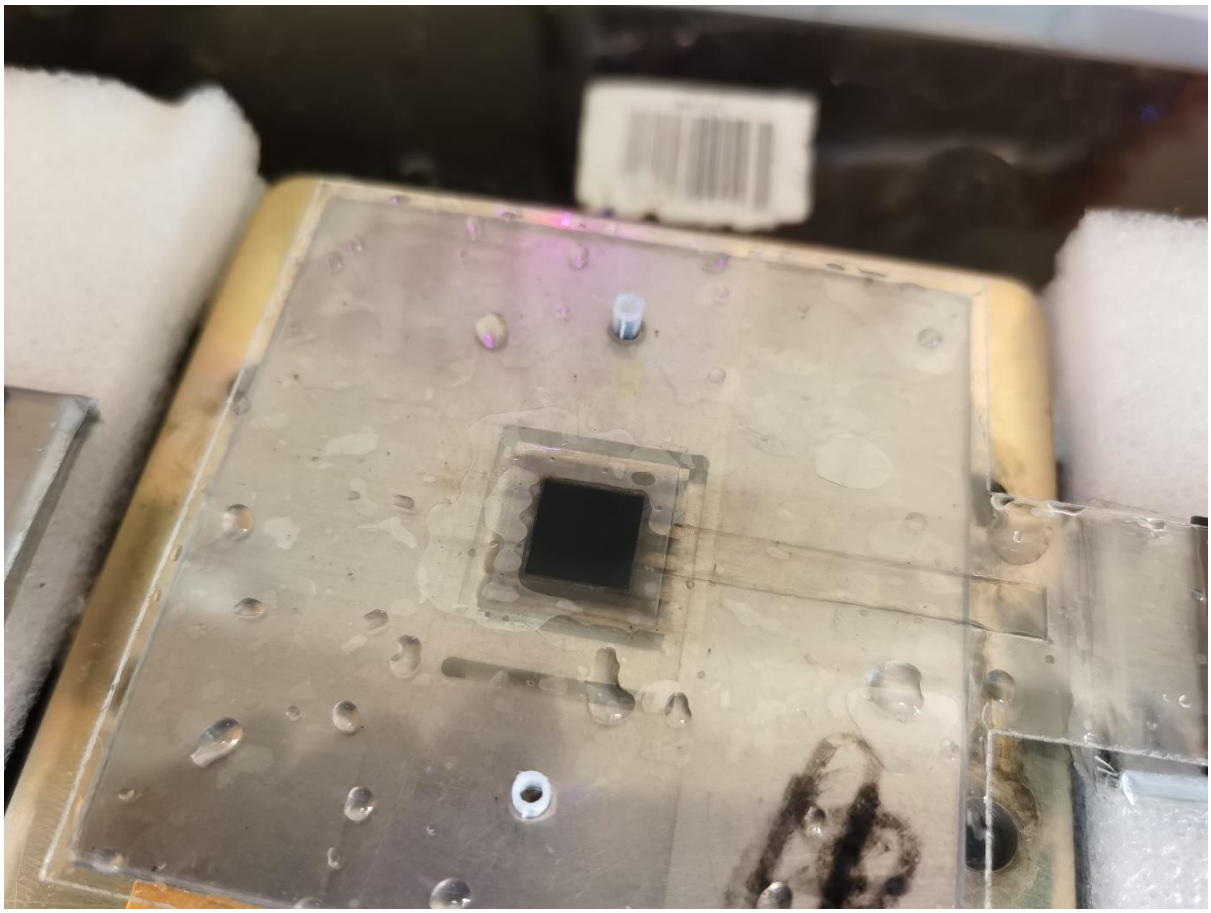

Add an extended 0.001″ gasket.

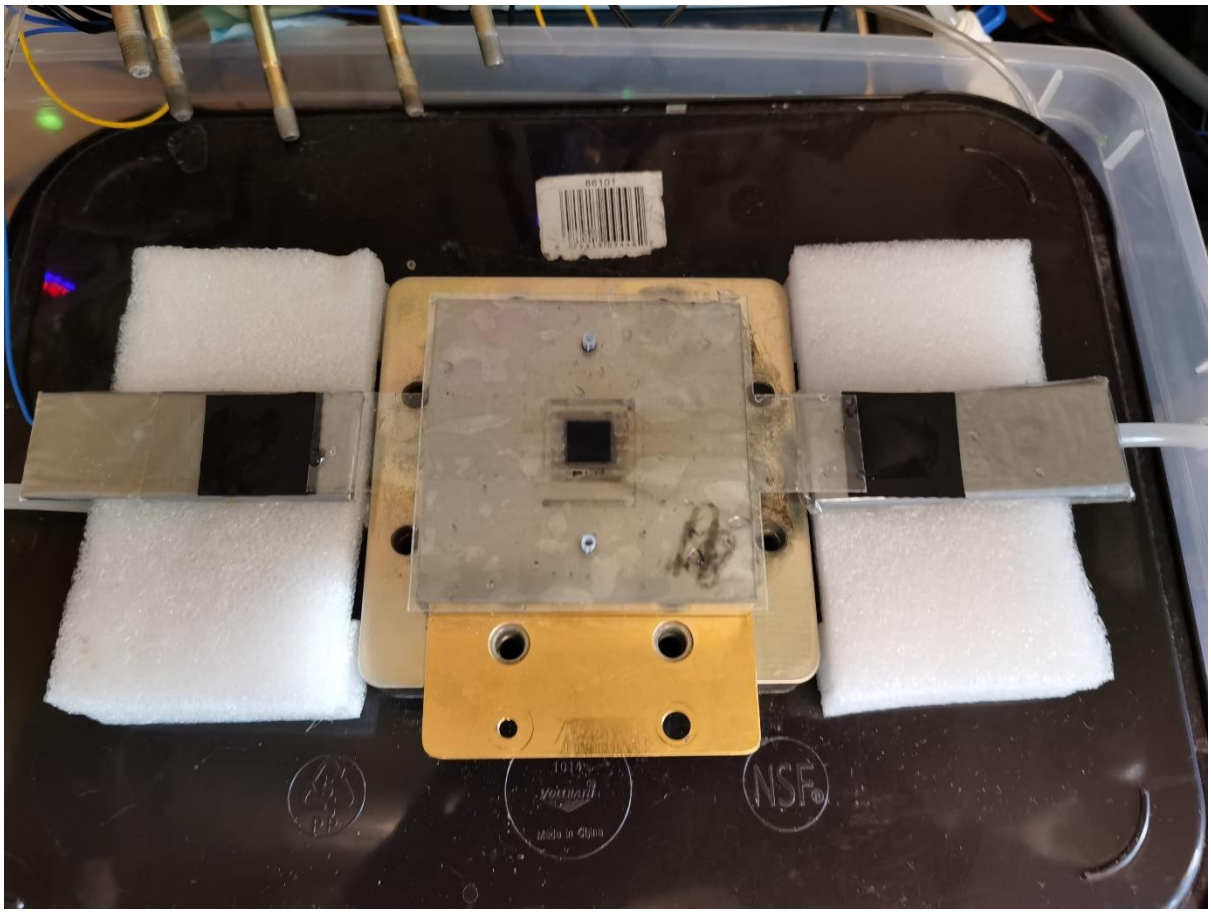

Add the CEL with WD catalyst facing down.

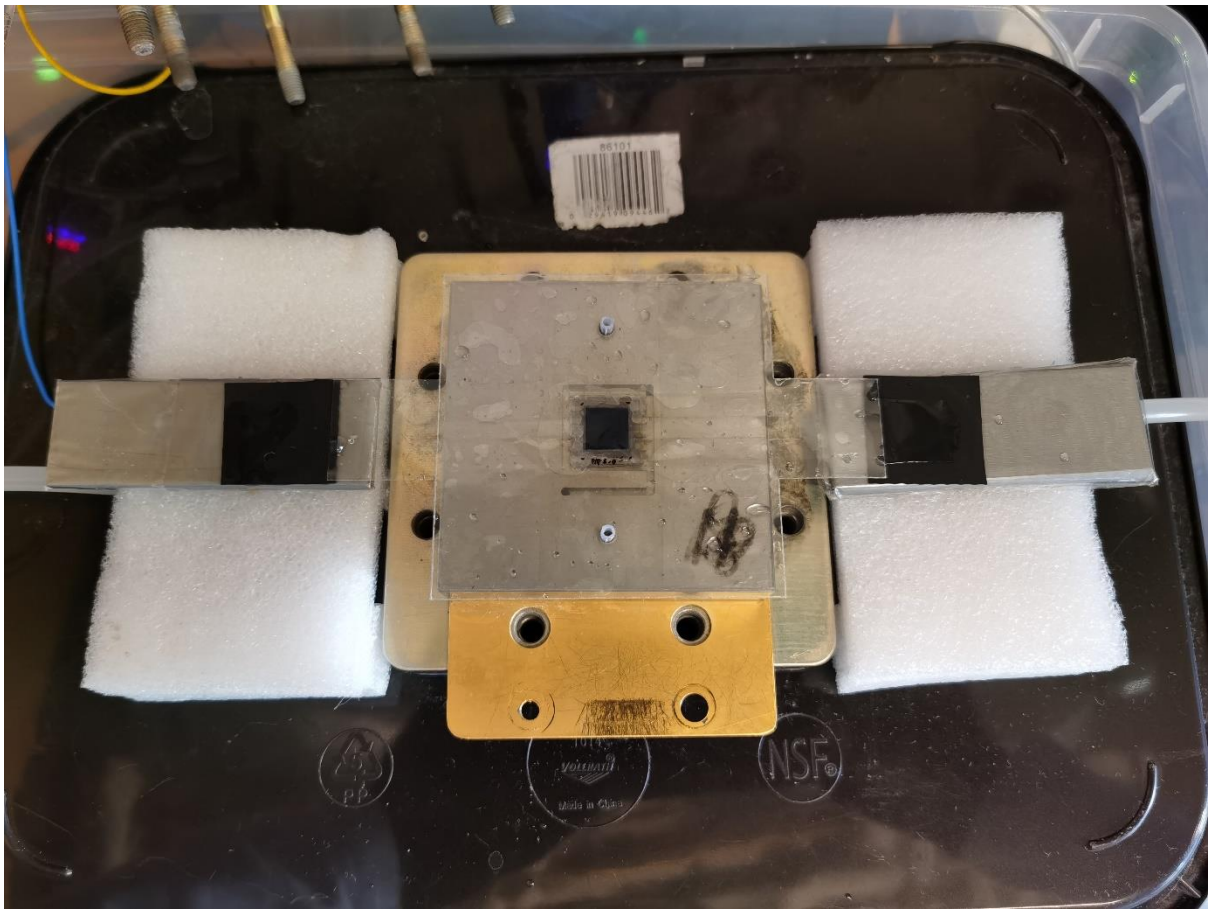

A closer view of the CEL.

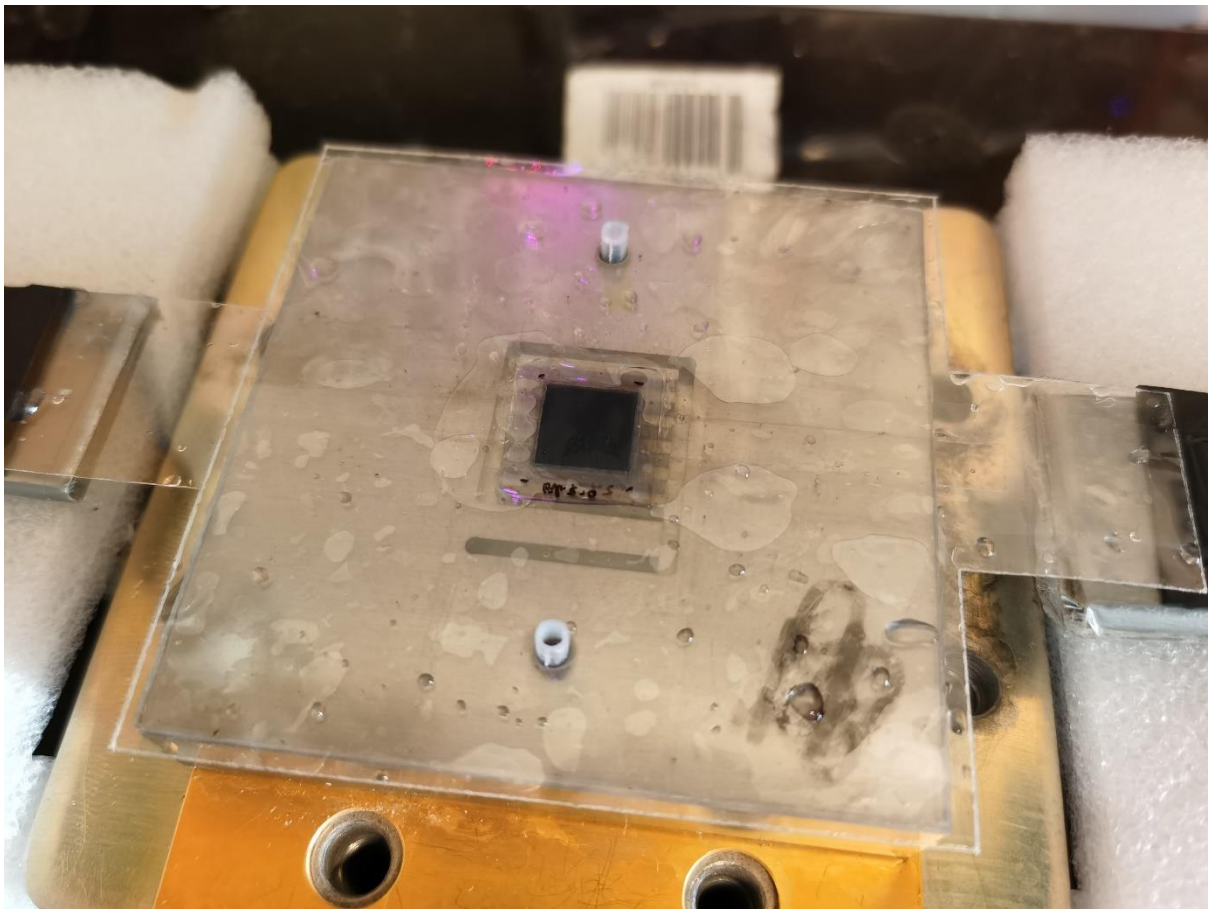

Add another extended 0.002″ gasket with an open “track” to prevent the membrane sensing strip from drying.

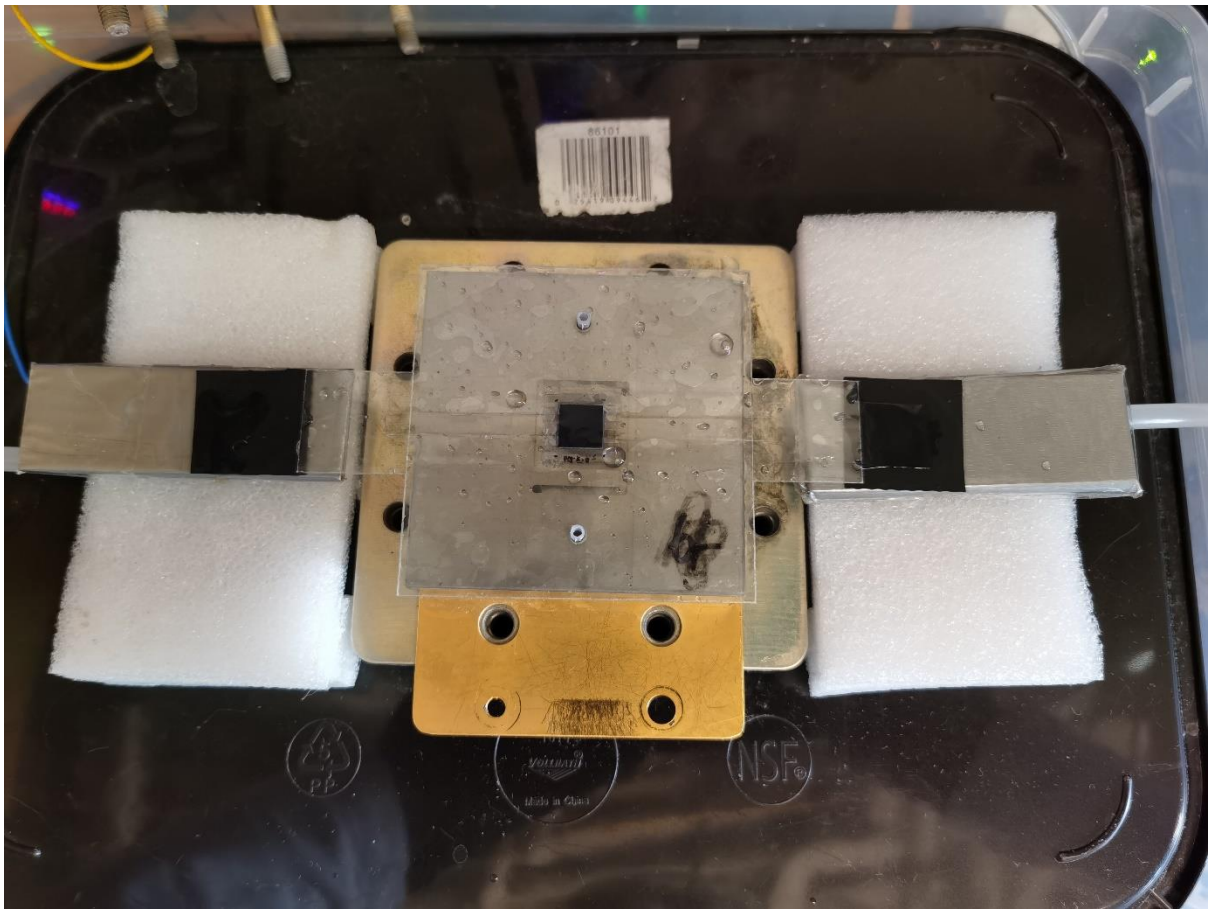

A closer view of the open “track”.

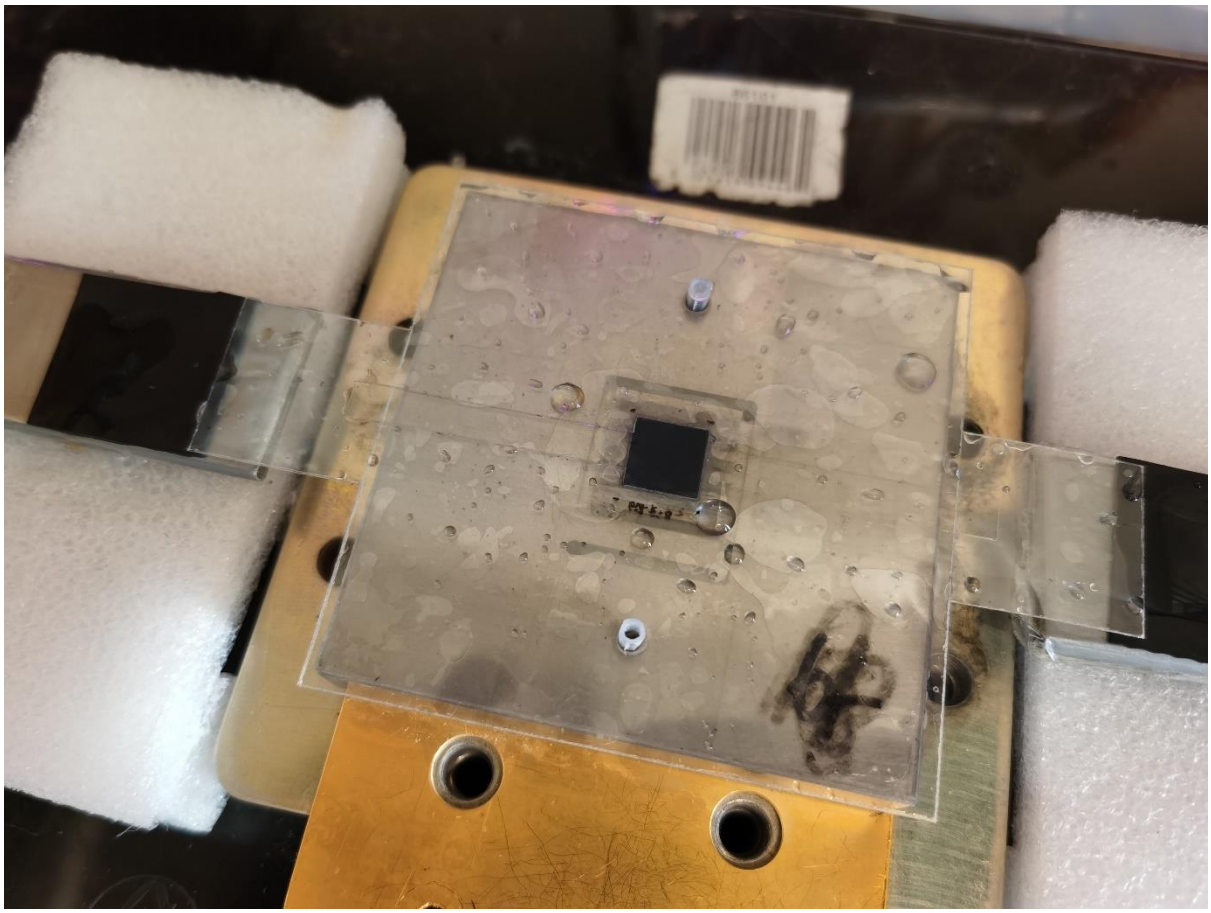

The CEL sensing strip is aligned with another edge of the active region and touches with the CEL.

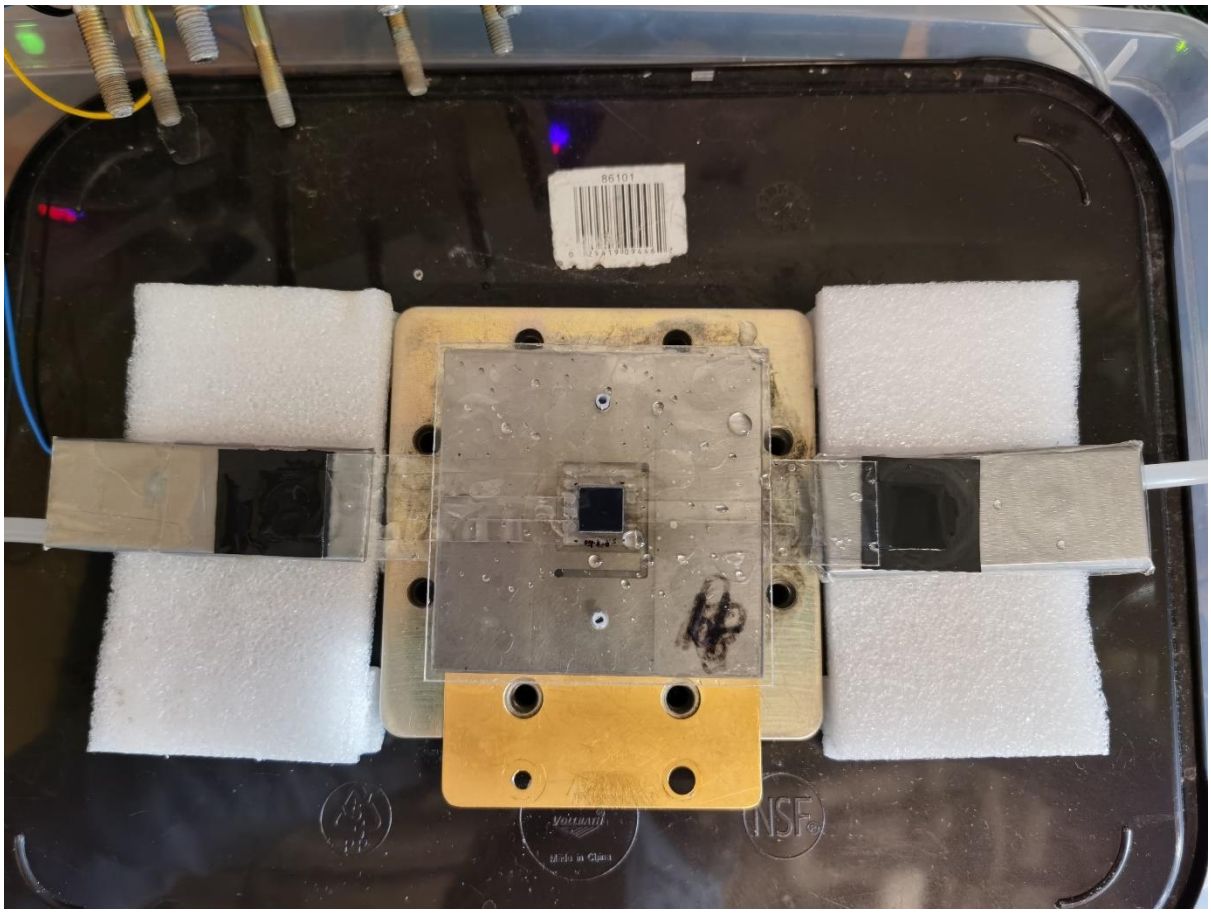

A closer view of the CEL sensing strip. Notice the ionic contact region is outside the active region.

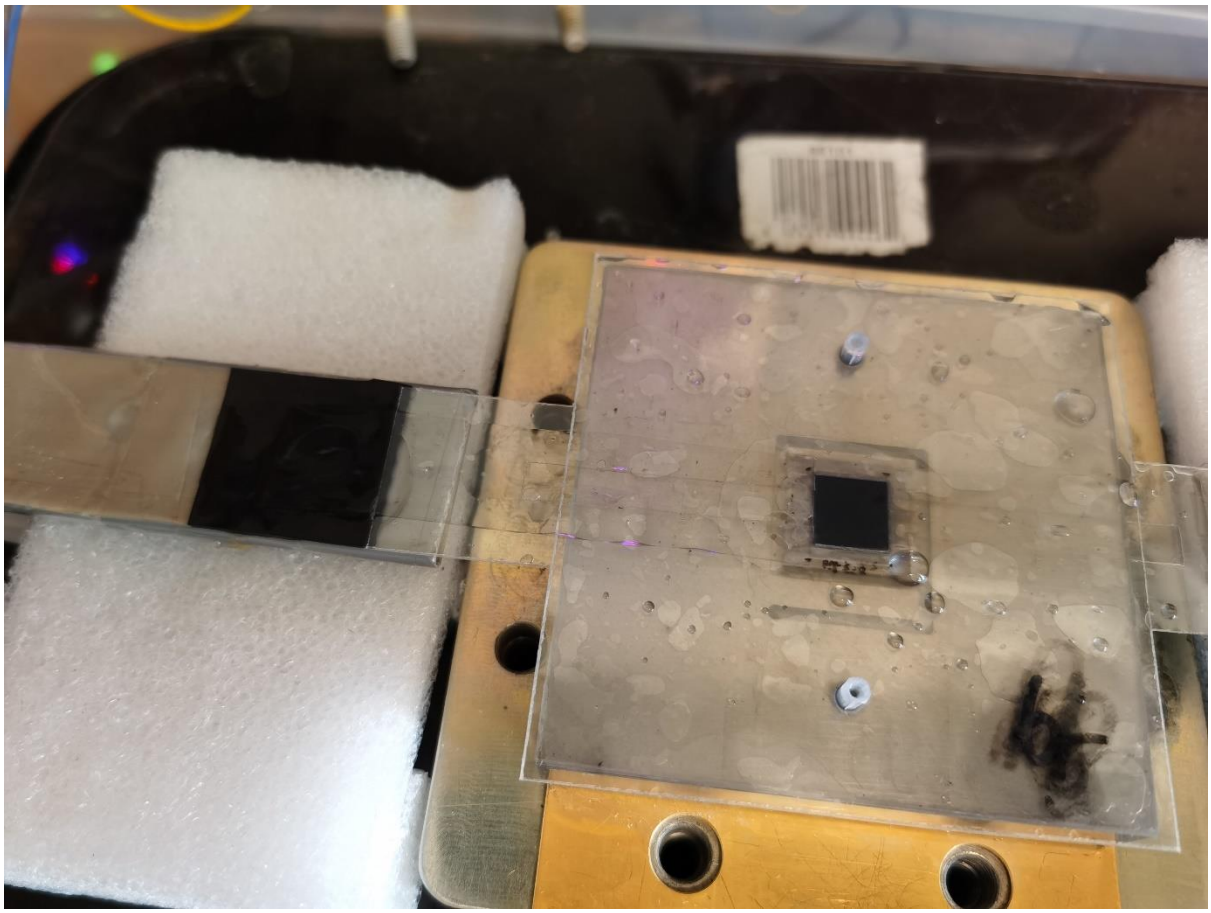

Install another extended 0.005″gasket to cover the CEL sensing strip.

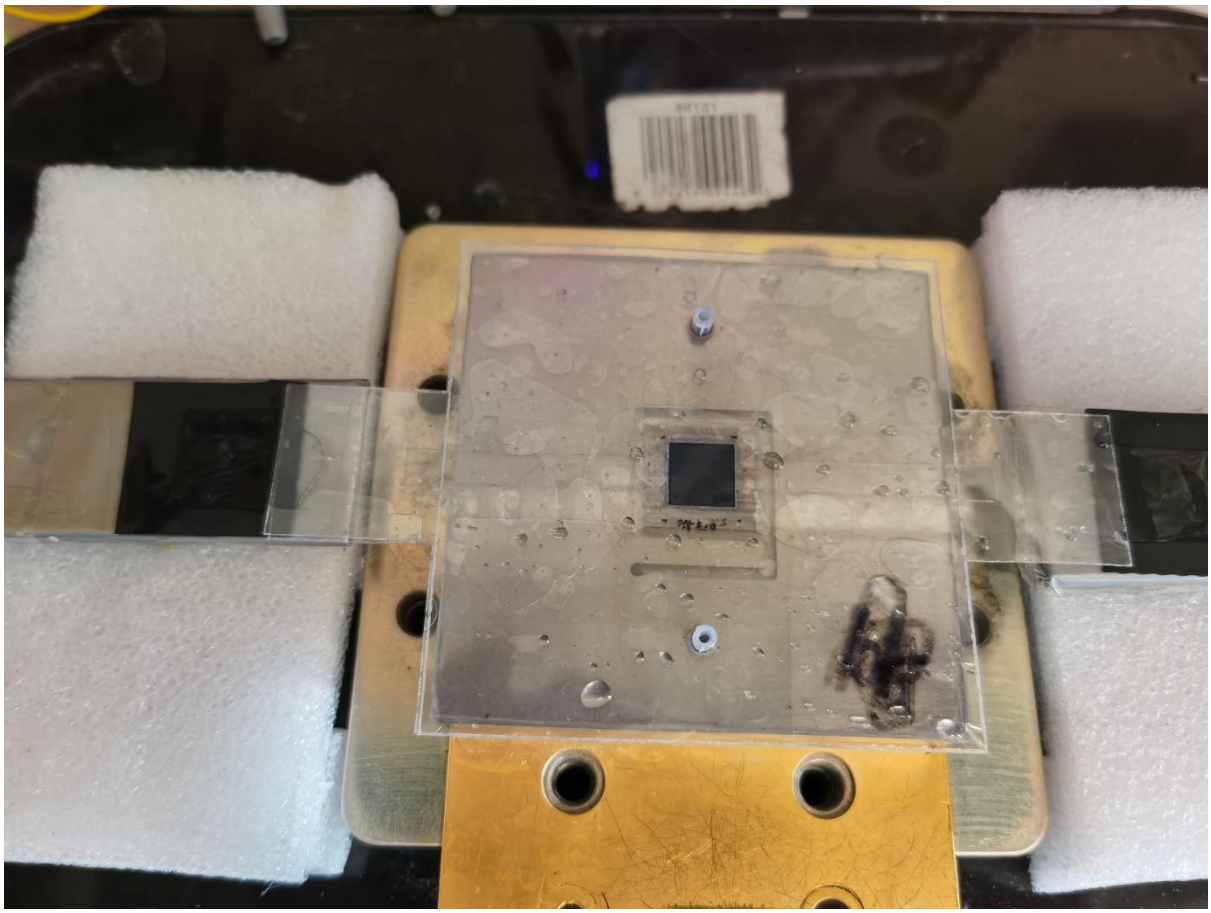

Add several gaskets with a total thickness of 0.025″.

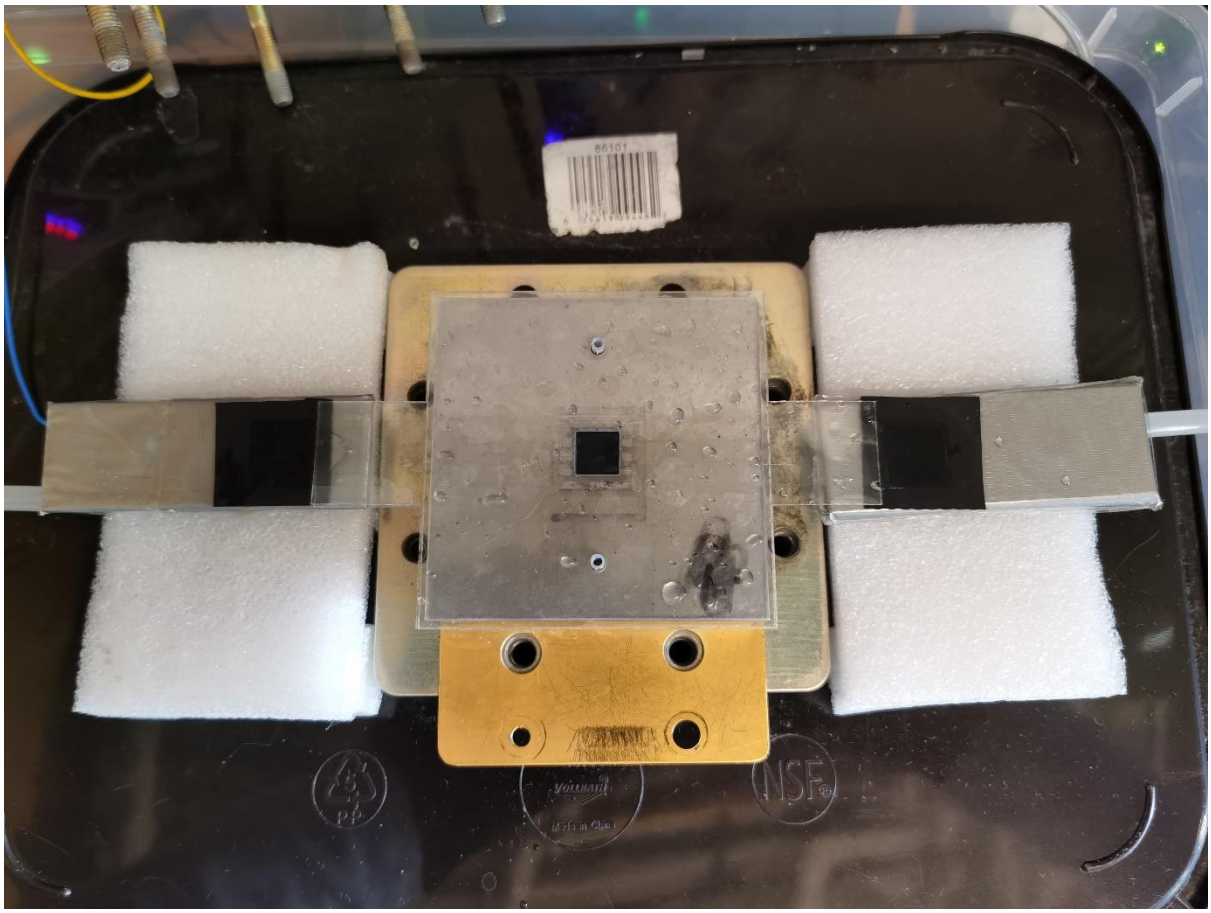

Install the cathode GDL (Pt facing down).

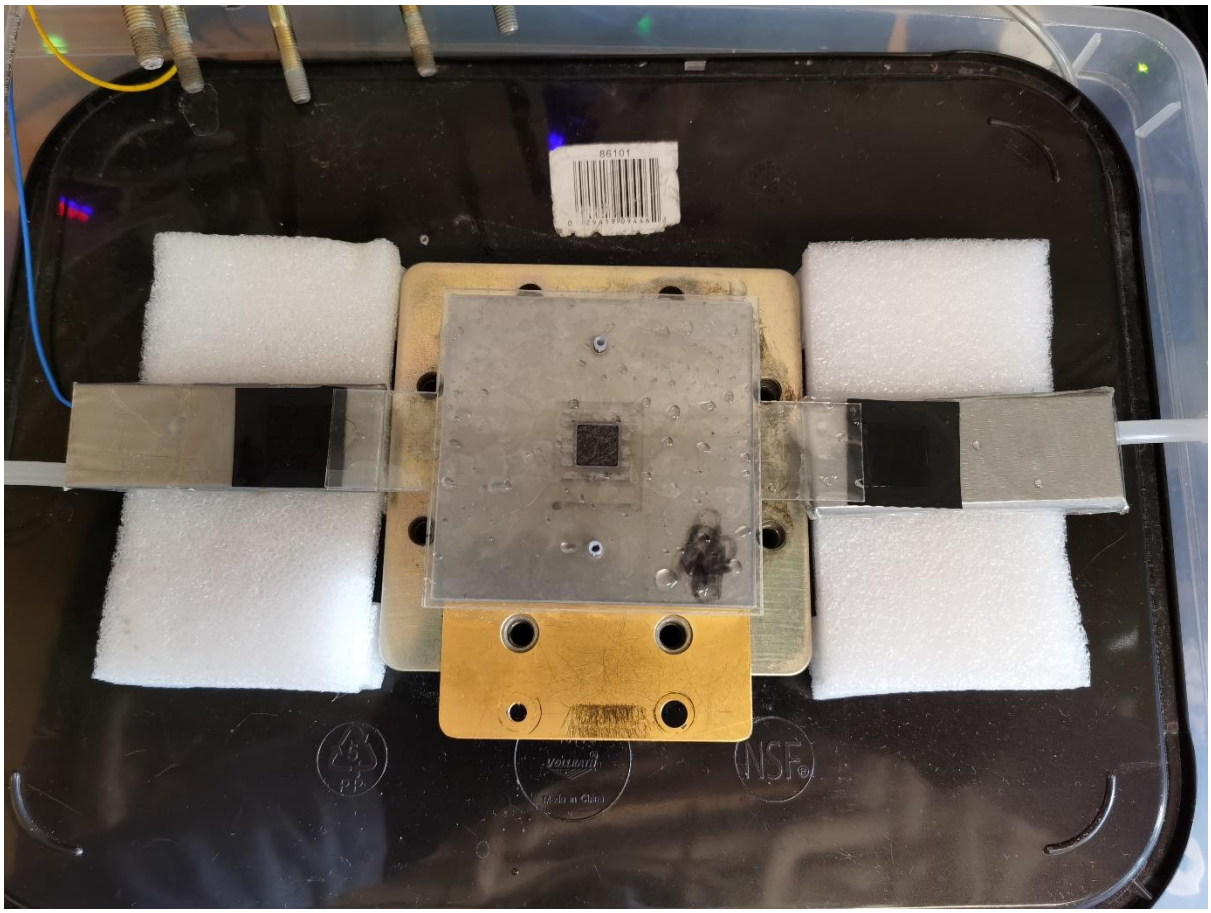

Install another Ti spacer.

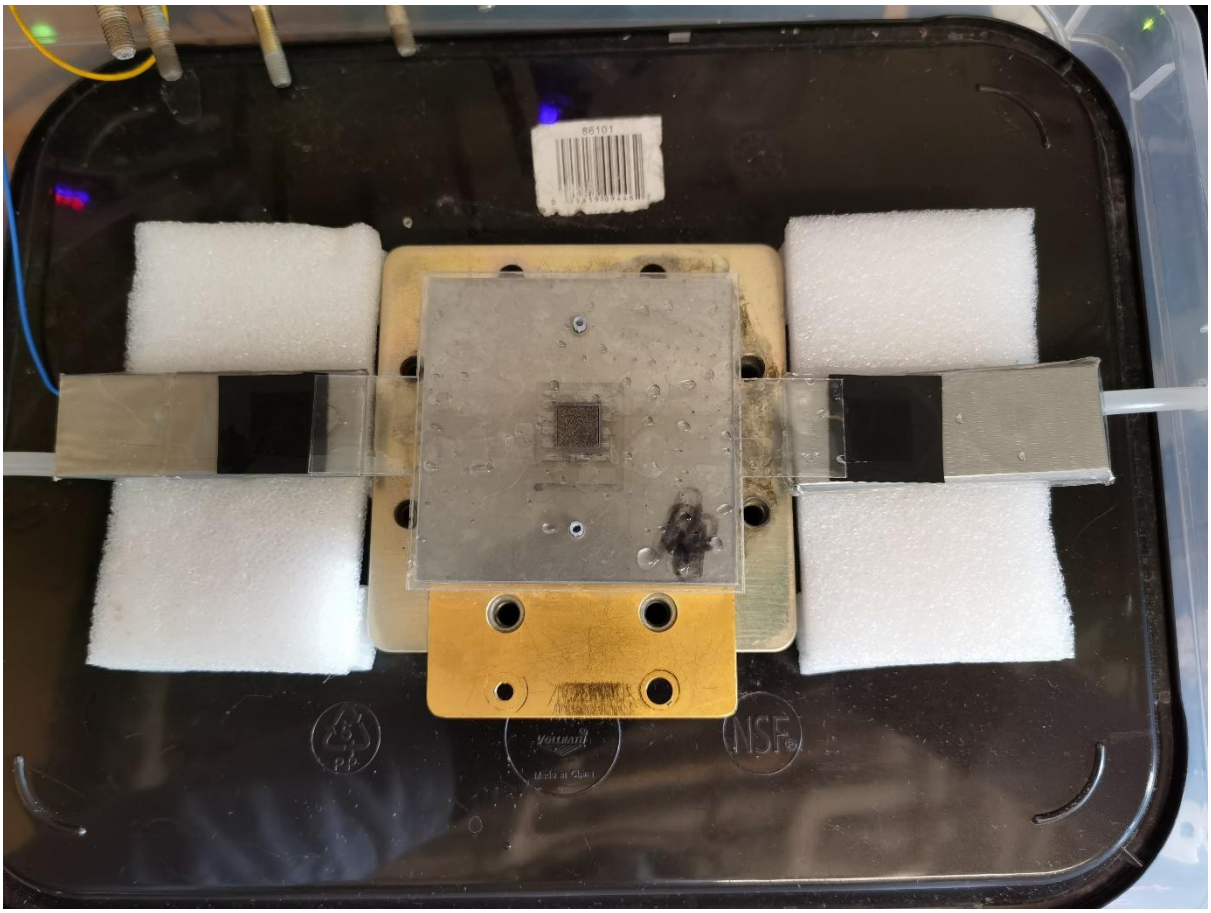

Install the cathode flow field and current collector.

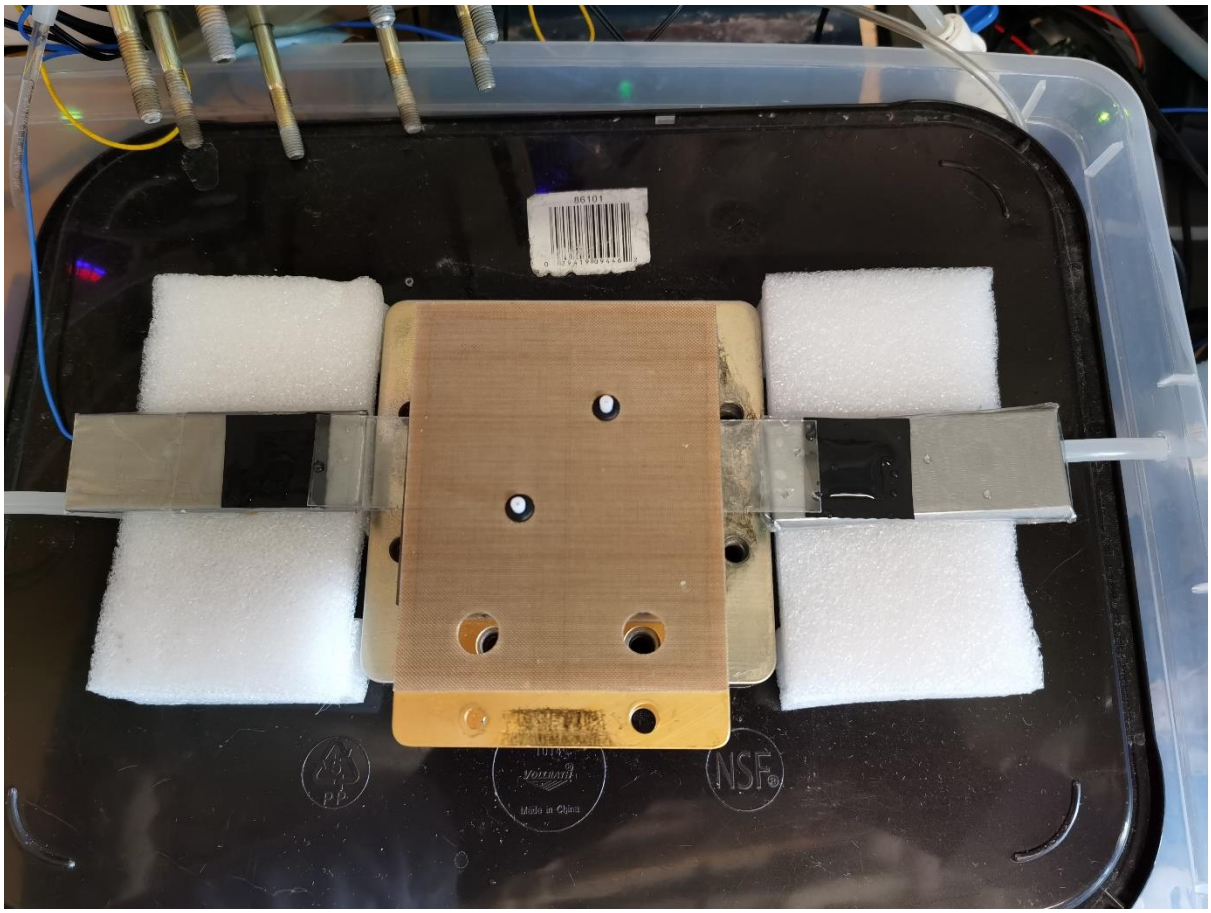

Bolt and tighten the cell by a torque wrench to 50 inch-pounds.

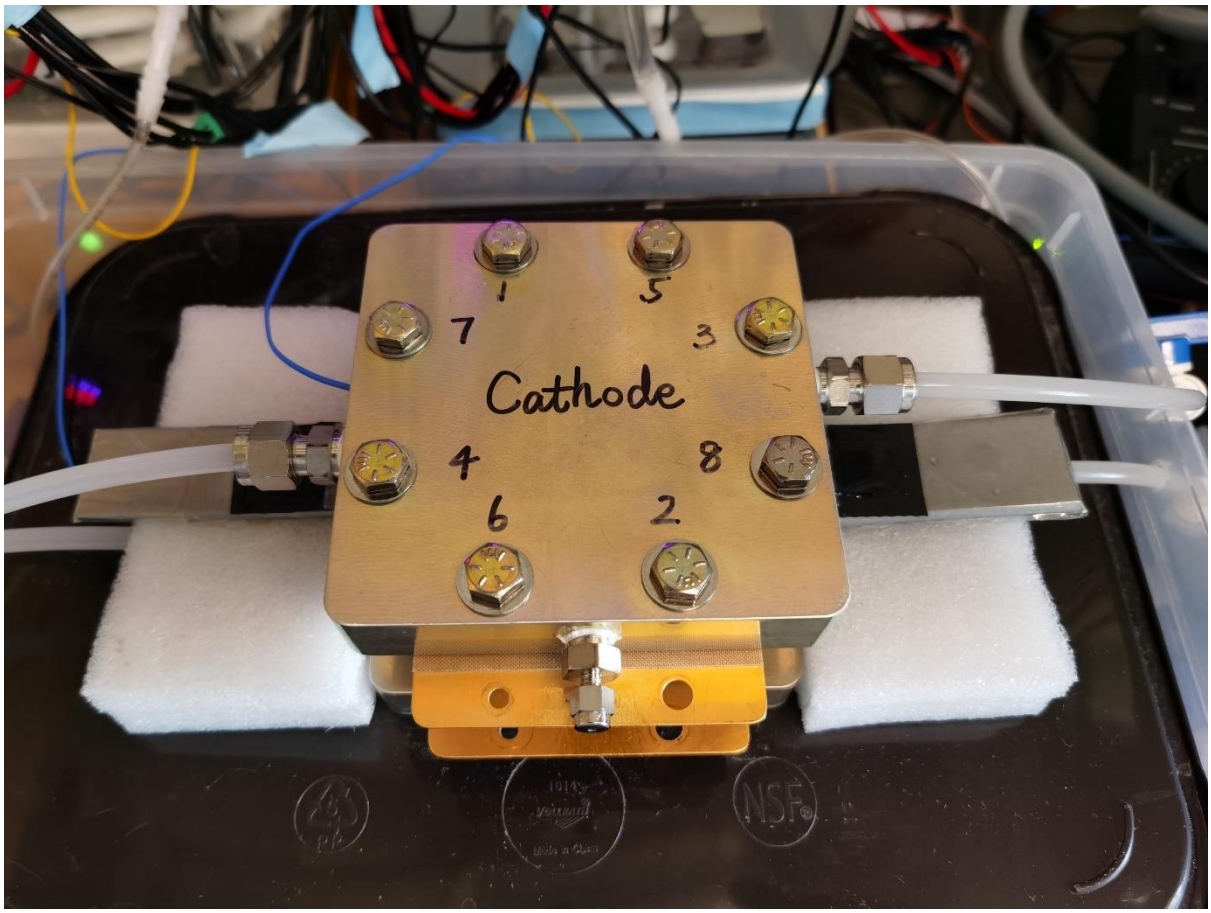

Place the O-ring on top of the exposed AEL sensing strip.

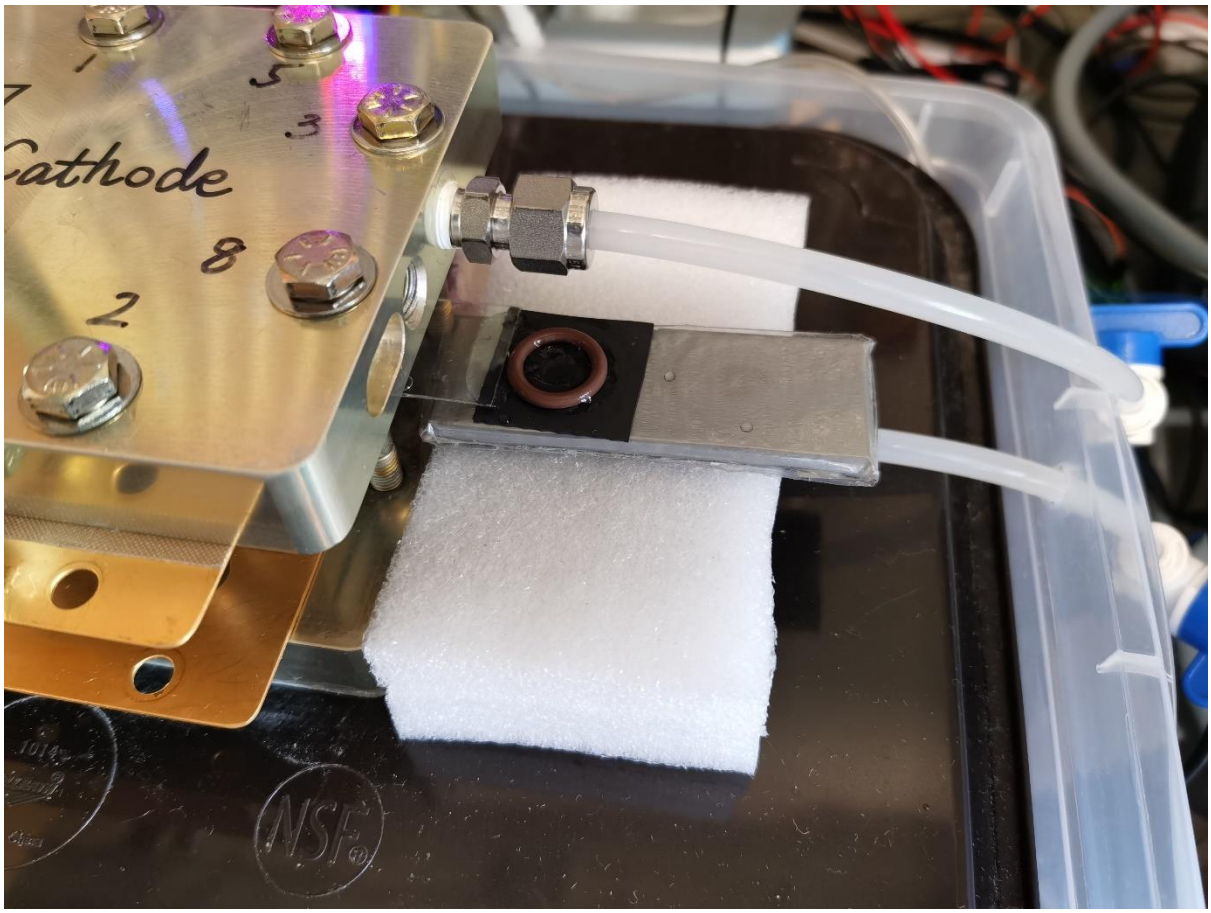

Place the O-ring joint (9 mm ID, 12 mm tube OD Chemglass Life Sciences, cut to ~4 cm in length) on top of the O-ring.

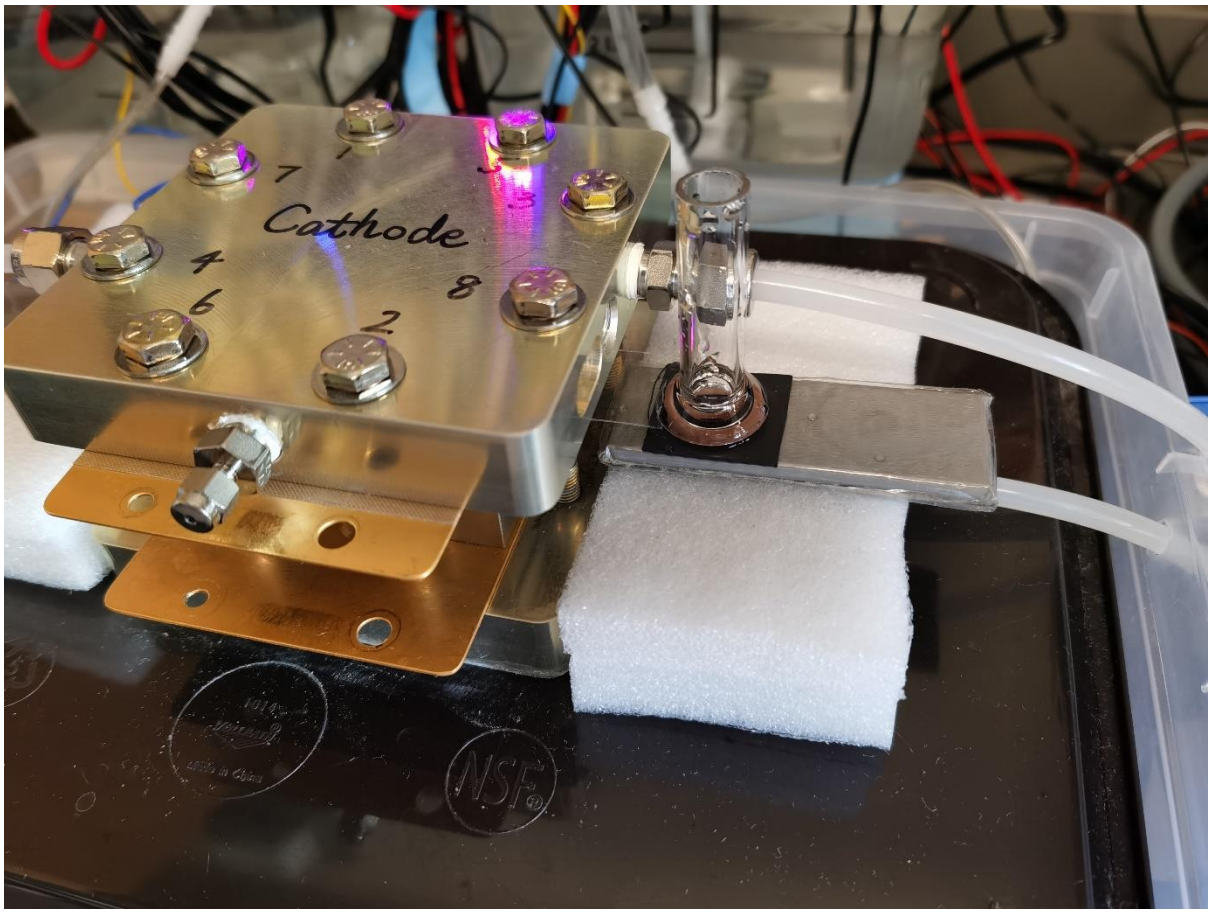

Clamp the O-ring joint.

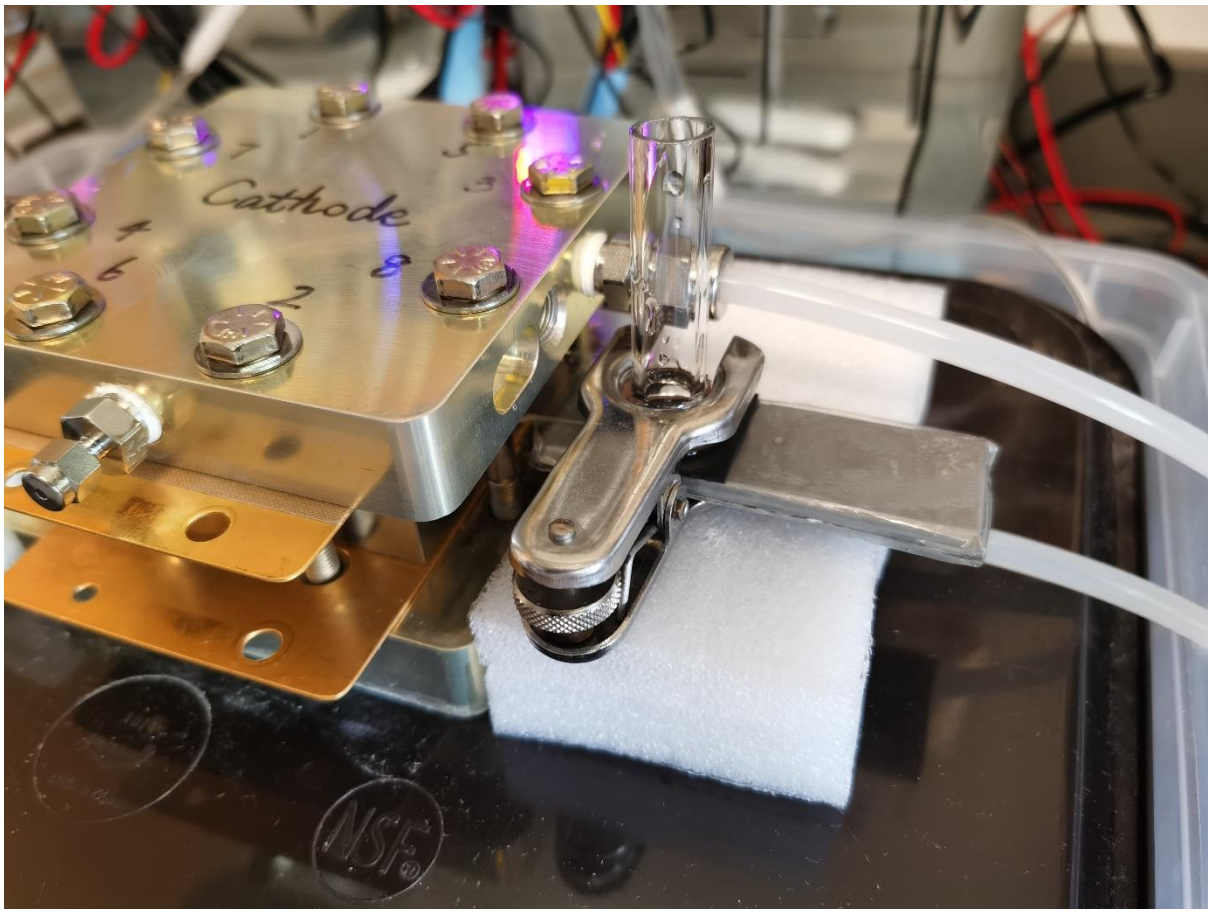

Place the O-ring on top of the exposed CEL sensing strip.

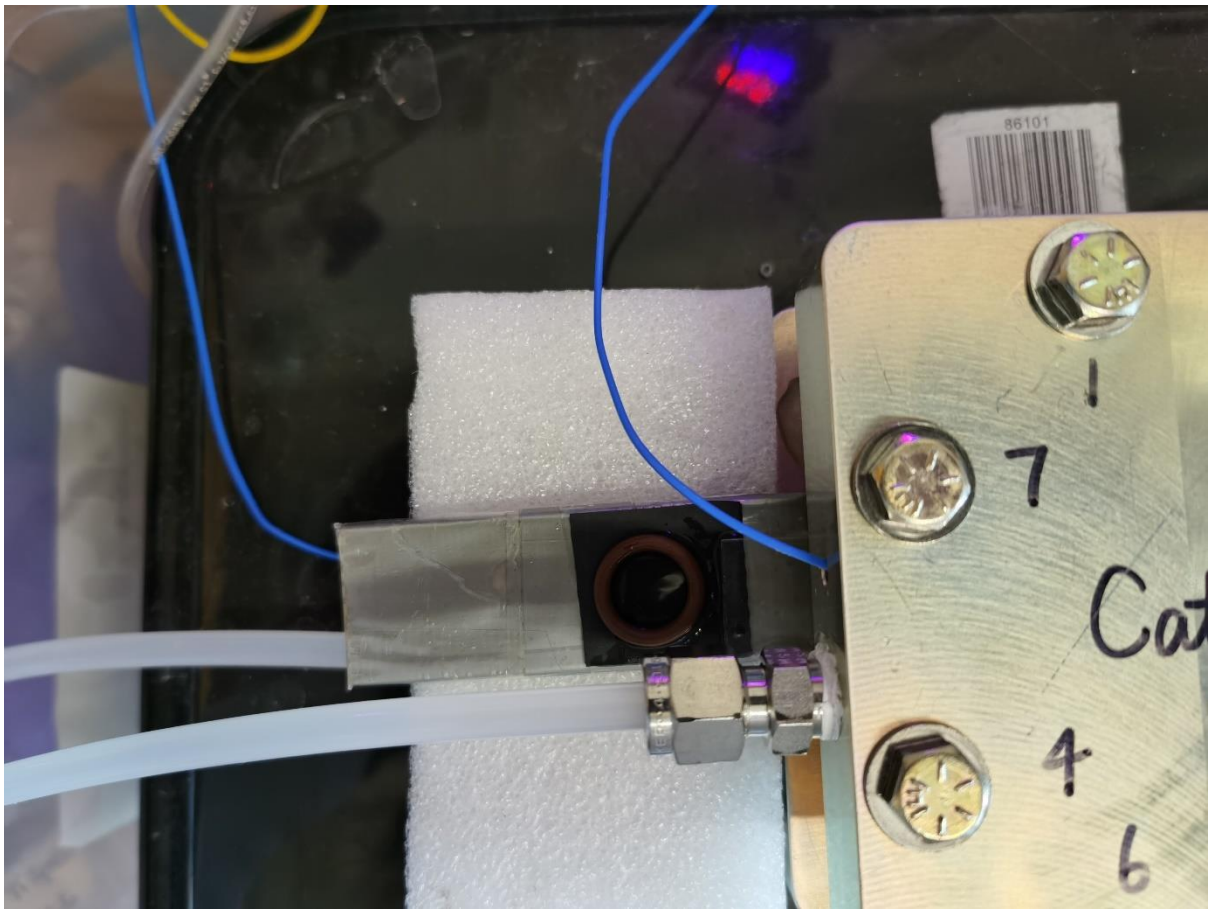

Place the O-ring joint on top of the O-ring.

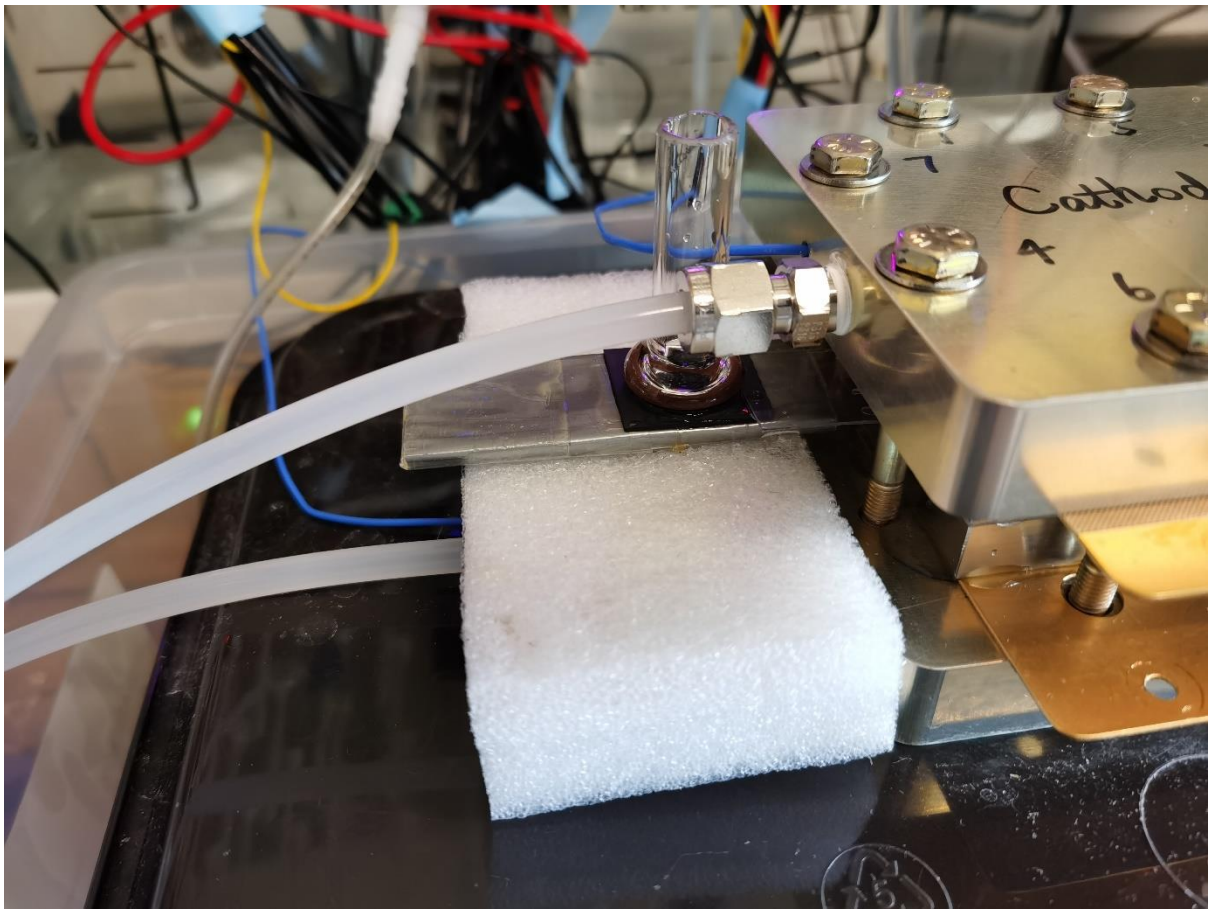

Clamp the O-ring joint.

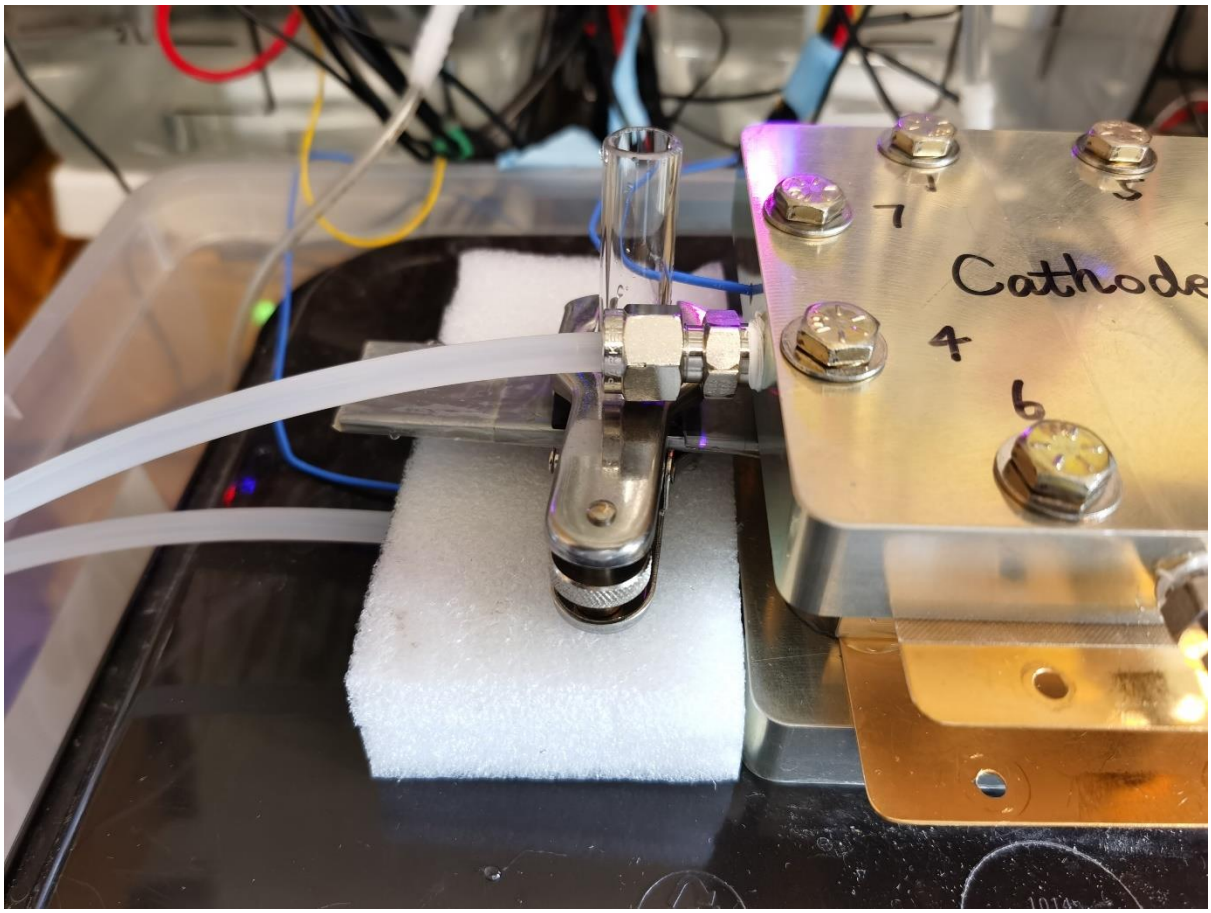

Remove the residual water in the O-ring joints.

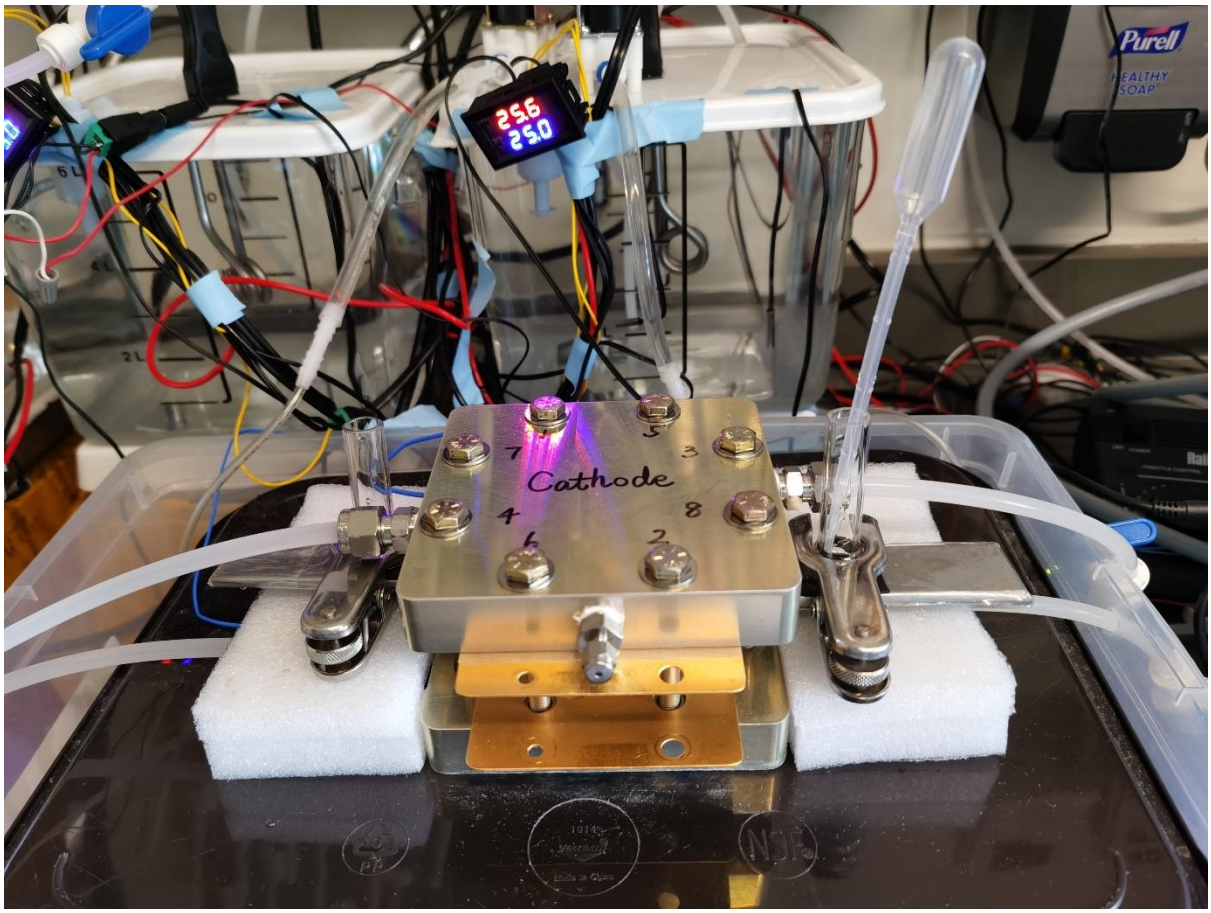

Fill the AEL side O-ring joint with 0.1 M KOH. Fill the CEL side O-ring joint with 0.1 M H_2SO_4.

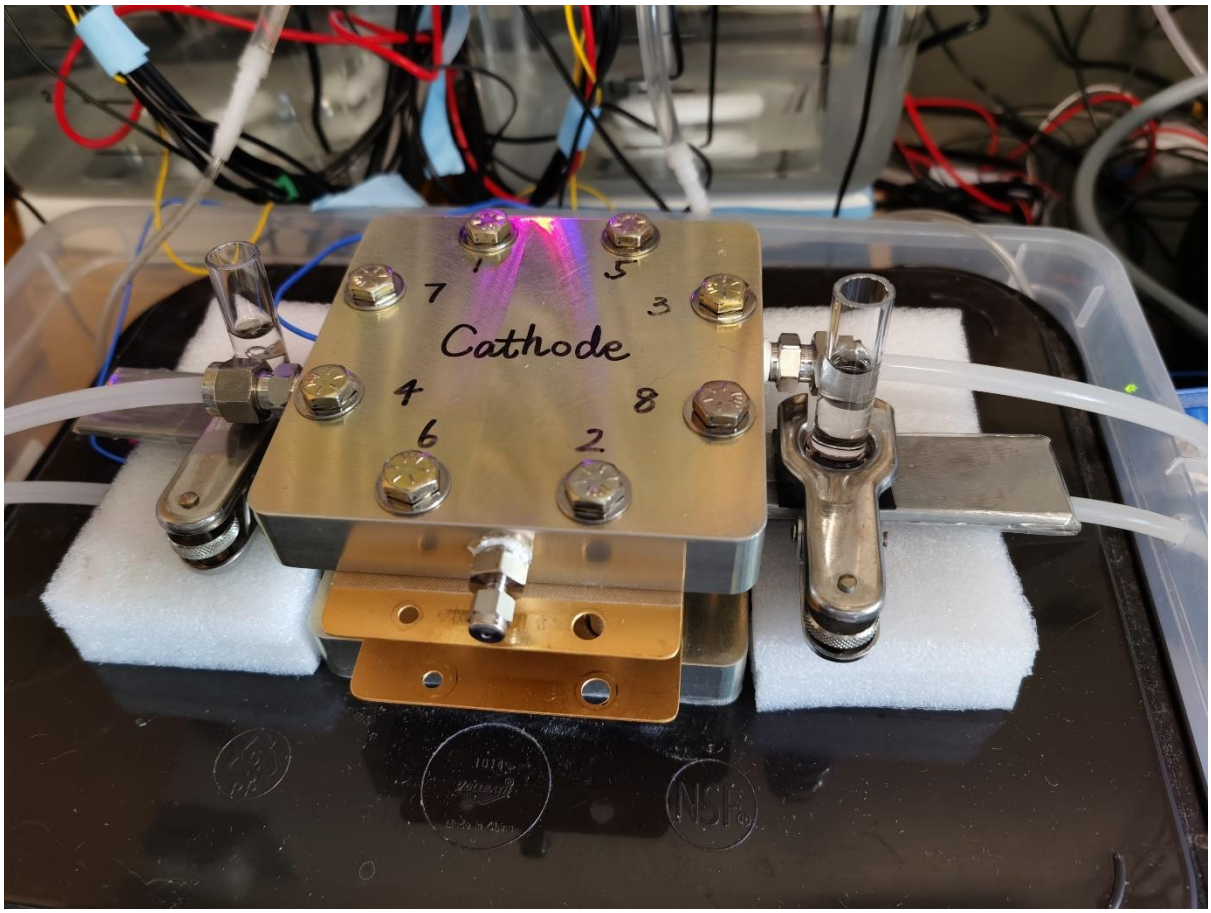

Place a Hg|HgO reference electrode (RE) inside the AEL side O-ring joint. Place a saturated calomel electrode (SCE) inside the CEL side O-ring joint.

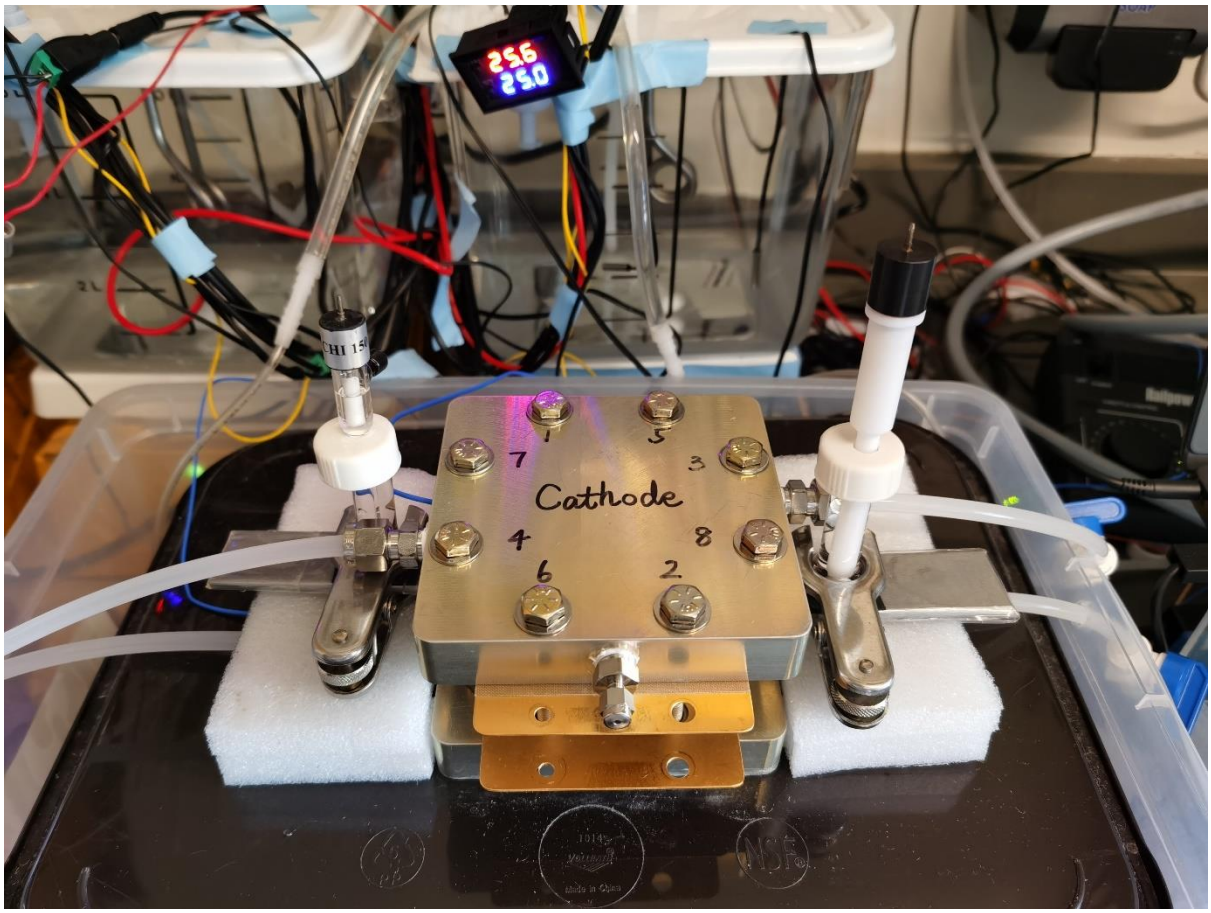

- The electrochemical tests are performed with a two-channel BioLogic VSP-300 potentiostat. For channel 1, P1 and S1 leads (P = power/current, S = voltage sense) are connected to the anode current collector, P2, S2 and S3 are connected to the cathode current collector. For channel 2, S1 is connected to the Hg|HgO RE, S2 to the cathode current collector, and S3 to the SCE RE. Channel 2 P1 and P2 are not used. Channel 1 and channel 2 are synchronized during the experiment.